SEPARATION OF RAYLEIGH WAVES IN AMBIENT NOISE USING POLARISATION-BASED METHOD

Mohsen Kazemnia Kakhki

Tese de Doutorado apresentada ao Programa de Pós-graduação em Engenharia Civil, COPPE, da Universidade Federal do Rio de Janeiro, como Parte dos requisitos necessários à obtenção do título de Doutor em Engenharia Civil.

Orientadores: Webe João Mansur

Franciane Conceição Peters

Rio de Janeiro

Junho de 2020

SEPARATION OF RAYLEIGH WAVES IN AMBIENT NOISE USING POLARISATION-BASED METHOD

Mohsen Kazemnia Kakhki

TESE SUBMETIDA AO CORPO DOCENTE DO INSTITUTO ALBERTO LUIZ COIMBRA DE PÓS-GRADUAÇÃO E PESQUISA DE ENGENHARIA DA UNIVERSIDADE FEDERAL DO RIO DE JANEIRO COMO PARTE DOS REQUISITOS NECESSÁRIOS À OBTENÇÃO DO GRAU DE DOUTOR EM CIÊNCIAS EM ENGENHARIA CIVIL.

Orientadores: Webe João Mansur

Franciane Conceição Peters

Aprovada por: Prof. Webe João Mansur

Prof. Otto Corrêa Rotunno Filho

Prof. Walnório Graça Ferreira

Prof. Jandyr de Menezes Travassos

Dr. Daniel Medeiros Moreira

RIO DE JANEIRO, RJ-BRASIL

JUNHO DE 2020

Kazemnia Kakhki, Mohsen

Separation of Rayleigh waves in ambient noise using polarisation-based method/ Mohsen Kazemnia Kakhki- Rio de Janeiro: UFRJ/COPPE, 2020.

Xi, 104 p.:il.; 29,7 cm.

Oriantadores: Webe João Mansur

Franciane Conceição Peters

Tese (doutorado)-UFRJ/COPPE/Programa de Engenharia Civil, 2020.

Referências Bibliográficas: p. 95-104.

1. Complex seismic trace. 2. Time-frequency decomposition. 3. Ambient noise. 4. Time-frequency polarisation analysis. 5. Horizontal to Vertical spectral ratio. 6. Rayleigh wave ellipticity. 7. Site response directivity in landslide-prone slopes. I. Mansur, Webe João *et al*. II. Universidade Federal do Rio de Janeiro, COPPE, Programa de Engenharia Civil. III. Título

ACKNOWLEDGMENTS

Firstly, I would like to express my sincere gratitude to Prof. Webe João Mansur, and to Prof. Franciane Conceição Peters for the continuous support of my Ph.D. study and related research, especially for their patience, motivation, and immense knowledge. Their effective guidance assisted me to facilitate the difficult way of research. They are always respectful in my mind owing to the trust they put in my work

Besides my advisor, I would like to thank the rest of my thesis committee for their insight comments and encouragement, which incentivized me to widen my research from various perspectives.

I would like to express my deepest gratitude to Prof. Vincenzo Del Gaudio, who exposed me into new subjects. My sincere thanks also go to Prof. Jandyr Travassos for his constructive comments and scientific support. I am also greatly indebted to Prof. Zaher Hossein Shomali who guided and encouraged me during my research with his constructive comments.

I would like to thank my fellow lab mates for the stimulating discussions, and the friendly atmosphere that they made for me. I would also thank Ahmad RahmatBar and Ahmad Mokhtari for their support in scientific discussions.

I gratefully acknowledge the Brazilian Research Council, CNPq, for doctorate fellowship. I would also like to acknowledge and PETROBRAS for a research grant during my last year of Ph.D.

Last but not least, I would like to thank my family: to my dear parents Habib and Raziyeh, my brothers Mahdi, Ehsan and Mehran for supporting me spiritually throughout writing this thesis and my life in general. Without the help of them, this work would not have been accomplished. My special thanks go to my adorable wife, who stood by me from the first step of my Ph.D. She played a significant role in my thesis in many aspects, not only emotionally, but also scientifically.

Resumo da Tese apresentada à COPPE/UFRJ como parte dos requisitos necessários a obtenção do grau de Doutor em Ciências (D.Sc.)

SEPARAÇÃO DE ONDAS DE RAYLEIGH EM RUÍDO AMBIENTE USANDO MÉTODO BASEADO EM POLARIZAÇÃO

Mohsen Kazemnia Kakhki

Junho/2020

Oriantadores: Webe João Mansur

Franciane Conceição Peters

Programa: Engenharia Civil

Ruído em sismologia é uma palavra geral usada para pequenas vibrações da terra com pequena amplitude conhecida como ruído ambiente ou microtremor. Microtremors compostos de uma coleção de ondas que se propagam em diferentes direções. A separação do campo de ondas sonoras em ondas corporais (P, SV, SH) e ondas superficiais (ondas Rayleigh e Love) e quantificar a proporção de cada tipo de onda seria o objetivo a ser atingido no presente trabalho. A troca de dados do domínio da frequência para o domínio do tempo ou vice-versa, considerada na metodologia utilizada, é útil na análise de dados. A análise de traços complexos, que é uma técnica de transformação, analisa dados sísmicos semelhantes ao sinal analítico. No entanto, essa técnica que se baseia na transformação convencional de Hilbert é suscetível a ruídos aleatórios e variações abruptas de frequência nos sinais sísmicos. Portanto, a transformação S adaptativa, baseada no Sparsity, acompanhada de uma função de ponderação com reconhecimento de dispersão, inspirada nas funções Geman-McClure e Laplace, é usada para solucionar esse problema. A obtenção das informações geológicas dos dados sísmicos motiva os pesquisadores a usar métodos baseados em polarização para discriminar entre diferentes fases da onda sísmica com base em suas polaridades. A combinação da definição intuitiva e direta da polaridade no domínio da frequência pelas propriedades não estacionárias dos métodos do domínio do tempo atrai a atenção para o uso de abordagens tempo-frequencia (TF) devido ao seu potencial em localizar as informações extraídas das ondas sísmicas em domínios de tempo e frequência. A análise de polarização também ajuda a detectar a ressonância direcional do local com mais confiabilidade do que os métodos conhecidos anteriores, através da separação da elipticidade das ondas Rayleigh.

Abstract of Thesis presented to COPPE/UFRJ as a partial fulfillment of the requirements for the degree of Doctor of Science (D.Sc.)

SEPARATION OF RAYLEIGH WAVES IN AMBIENT NOISE USING POLARIZATION-BASED METHOD

Mohsen Kazemnia Kakhki

June/2020

Advisors: Webe João Mansur

Franciane Conceição Peters

Department: Civil Engineering

Noise is a general word that is used in seismology for minor earth vibration with small amplitude known as ambient noise or microtremor. Microtremors are composed of waves that are propagating in different directions. Separation of the noise wavefield into body waves (P, SV, SH) and surface waves (Rayleigh and Love waves), and quantify the proportion of each type of waves would be the desired purpose. Exchanging data from frequency domain to time domain or vice versa is useful in data analysis. Complex trace analysis, which is a transform technique, analyzes seismic data similar to analytic signal. However, this technique which relies on conventional Hilbert transformation is susceptible to random noise and abrupt frequency variations in seismic signals. Therefore, the Sparsity-based, adaptive S-transform accompanied with a sparsity-aware weighting function, inspired by the Geman-McClure and Laplace functions is used to address this problem. Obtaining the geological information from the seismic data motivates the researchers to use polarisation-based methods to discriminate between different phases of the seismic wave based on their polarities. Combining the intuitive and straightforward definition of the polarity in the frequency domain by the non-stationary properties of the time domain methods attracts the attention towards using time-frequency (TF) approaches owing to their potential in localizing the extracted information of the seismic waves in both time and frequency domains. Polarisation analysis also helps in detecting the site directional resonance more reliably than the previous known methods via separating the Rayleigh wave ellipticity.

TABLE OF CONTENTS

LIST OF FIGURES ..... **ix**
LIST OF TABLES ..... **xi**
1-Introduction **1**
1-1 Motivation 1
1-2 Objectives 2
1-3 Outline of thesis 3
2-Complex seismic trace **4**
2-1 Introduction 4
2-2 Calculation of the complex trace 4
2-2-1 Basic information 4
2-3 Calculation of the quadrature trace (imaginary part) 6
2-4 High resolution time-frequency Hilbert transform using sparsity-aware weighting function 8
2-4-1 Introduction 8
2-4-2 Methodology 9
2-4-3 Experimental results 16
2-4-4 Conclusion 20
3-Wave polarisation analysis **21**
3-1 Literature review 21
3-2 Complex polarisation analysis of particle motion 22
3-2-1 Methodology of complex polarisation 22
3-3 Polarisation attributes defined by Rene (1986) 25
3-4 Polarisation of Rayleigh waves 27
3-5 Time-frequency polarisation analysis 28
3-5-1 Introduction 28
3-5-2 TF-based polarisation calculation 31
3-5-3 Results 33
3-5-4 Polarisation filtering 39
3-5-5 Conclusions 41
4-Ambient noise **43**
4-1 Ambient noise 43
4-2 The origin of microtremors 43
4-3 Application of the microtremors 45

4-4 Composition of the seismic noise wavefield 46
4-5 Contribution of Rayleigh waves in the noise wavefield 48
4-6 Relative contribution of the fundamental mode of Rayleigh waves 49
4-7 Horizontal to vertical spectral ratio 49
4-7-1 H/V technique review 50
4-7-2 The H/V Origins: Body-Wave Based Theories 50
4-7-3 The Role of the Surface Waves 53
4-7-4 Achieving amplification factor from H/V ratio 56
5-Polarisation analysis on Ambient noise 59
5-1 Basic principles 59
5-2 Analysis procedure 60
5-3 Analyses of synthetic data 62
5-4 Discussion & Conclusion 65
6-Application of polarisation analysis of ambient noise in defining site response directivity in landslide-prone slopes 69
6-1 Introduction 69
6-2 Region survey 71
6-3 Geotechnical surveys 74
6-4 ERT results 76
6-5 Ambient noise method 79
6-6 Site response directivity 84
6-7 Conclusions 89
7-Conclusions and Recommendations 92
7-1 Overview 92
7-2 Main conclusions 93
7-3 Recommendations for future research 94
References 95

LIST OF FIGURES

2- 1 Isometric diagram of an actual seismic trace. 7

2- 2 a) A multi-component signal with several Ricker wavelets, b) the corresponding amplitude spectrum, c) the SST time-frequency map of the signal computed by (d) the window-lengths reversely proportional to the amplitude spectrum shown in b (Parameter r is chosen to be 1 for this signal because it is a narrowband and not spectrally diverse). 11

2- 3 a) A non-stationary logarithmic chirp signal, b) the correspondent amplitude spectrum, c) window length variation with frequency in terms of sample numbers for conventional ST (red line) and adaptive SST (blue line). The time-frequency map of the non-stationary signal was computed by d) the conventional ST and e) adaptive sparsity, using the adaptive arbitrary windows, f) the desired matrix of adaptive windows with shifted arbitrary windows. 12

2- 4 Graphs a) $g_\beta(\omega)$ and b) $l_\beta(\omega)$ for different values of β 16

2- 5 a) Double chirp signal, b) its time-frequency panel for the WSST method using the LF and the GMF. c) Noisy double chirp signal, d) its time-frequency panel for the WSST method using the LF and e) the GMF. The white arrows show the effect of GMF where the desired signal is lost. 17

2- 6 Time-frequency panel for Double chirp signal with four methods, ST, RWHT, SST, and WSST (a-d), and the noisy form (e-h). 18

2- 7 a) Synthetic signal, and b) time-frequency panels for the RWHT, c) the SST, and d) the WSST methods. e) Synthetic noisy signal and, f) time-frequency panels for the RWHT, g) the SST, and h) the WSST methods. 19

3- 1 Polarisation ellipses for harmonic signal with phase differences of 0, π/4, π /2, 3 π /4, π, and - π/4 radians. Positive and negative phase differences correspond to retrograde and prograde motion, respectively. Positive values of the tilt and rise angles (τ and γ) indicate forward tilt of the ellipse. Reciprocal ellipticity is the ratio of the semi-minor and semi-major axis lengths (ρ = b/a). 26

3- 2 The ellipse of retrograde motion is plotted together with the polarisation attributes. p and n are the nodes (intersection of the ellipse with the horizontal plane), a and b are the ellipse major and minor semi-axes, respectively, the angle I is the inclination of the ellipse plane concerning the horizontal plane. The angle ω is that between pn and a, measured on the ellipse plane, whereas Ω is that between pn and the x axis, measured on the horizontal plane. 32

3- 3 The three-component synthetic seismogram (a) with their corresponding spectrum obtained via ST (b-c) and sparse ST (d-g). 34

3- 4 The spectrums of semi-major, semi minor, the difference of the ellipse axes, and the total power spectrum of the synthetic seismograms in Fig. 3-3 by S transform (a-d), and Sparse ST (e-h). 35

3- 5 The radial, transverse, and vertical components of the excerpted displacement record for the earthquake registered at PEMO station. 36

3- 6 The amplitude spectrum of the X, Y, and Z components achieved by ST (top plots) and Sparse ST (bottom plots). 37

3- 7 The spectra of semi-major, semi minor, the difference of the ellipse axes, and the total power spectrum of the seismogram in Fig. 3-5 by S transform (upper plots), and Sparse ST (lower plots). 38

3- 8 The spectrums of the argument of maximum $\omega\left[\hat{\tau}, \hat{f}\right]$, inclination $I\left[\hat{\tau}, \hat{f}\right]$, strike $\Omega\left[\hat{\tau}, \hat{f}\right]$, and the phase $\varphi\left[\hat{\tau}, \hat{f}\right]$ of the seismogram in Fig. 3-5 by S transform (upper plots), and sparse ST (lower plots). 38
3- 9 The total filter of Eq. (3-21) and the corresponding filtered spectrum of the 3-component signal of Fig. 3-5 achieved by S transform (top plots) and sparse S transform (bottom plots). 41

4- 1 Model of an elastic layer over a half-space. Poisson's ratios, υ, were determined from V_s as follows: υ =0.499-1.16.10^{-4} (V_s -150), for $V_s \geq$ 150m/sec. Source: Konno and Ohmachi (1998). 54
4- 2 Particle orbit of three types of fundamental-mode Rayleigh waves for the models in Fig. 4-1. Source: Konno and Ohmachi (1998). 55

5- 1 Comparison of HVIP (left figure) and Nakamura (right figure) H/V ratio 64
5- 2 Polar diagram of polarisation between azimuths 0^{O} to 360^{O} 65

6- 1 a) Topography of the stations, b) Aerial map of Nargeschal village with the locations of boreholes and trial pits, cross-sections A and B, ambient noise stations (ST1-6) and ERT profiles, (P5 is in the direction of moving mass, P1-4 are perpendicular to the sliding direction), the white-dashed ellipse delimits the landslide area, b) Topography of the stations..... 72
6- 2 Rose diagram representing the main vector of landslide movements based on the Nargeschal region landslide map (left figure) and the fracture and fault orientations (right figure) in the study area. 73
6- 3 Boreholes drilled in the study area with their corresponding lithology 74
6- 4 Geological cross-sections A and B, as located in Fig. 6-1. The blue dotted line in (b) represents the water content 76
6- 5 The ERT profiles and their quasi 3D view (the black dotted line is the sliding surface) 78
6- 6 H/V curves obtained from a geometric average of the horizontal components as a function of frequency (black solid lines) calculated for stations: (a) ST1, (b) ST2, (c) ST3, (d) ST4, (e) ST5 and (f) ST6. Dashed lines represent the standard deviation from the average and the grey areas are representative of frequency peak precision. 80
6- 7 The inversion results of the experimental H/V curve, assumed as representative of ellipticity curve of Rayleigh waves, at Station ST3. The red curve is the estimated curve best fitting the empirical H/V curve (black curve). The relevant shear wave velocity profile is reported beside the curve..... 81
6- 8 Comparison between shear wave velocity (red line) and SPT-N (green square) at stations a) ST4 b) ST5. 82
6- 9 Rayleigh wave ellipticity achieved by using the HVIP method along the directions of main peak values (specified by the legend). 83
6- 10 Azimuthal variations of HVSR values obtained for stations (a) ST1, (b) ST 2, (c) ST 3, (d) ST 4, (e) ST5 and (f) ST6. 85
6- 11 Polar diagrams of HVIP values obtained from noise recordings 87

LIST OF TABLES

3- 1 Classification of waves using polarisation attributes (Rene et al. 1986). 28

4- 1 summary of ambient noise sources according to frequency. Source: Gutenberg (1958) and Asten (1978, 1984) 44
4- 2 Ambient noise classification. Source Seo (1998) 44
4- 3 Summary of Rayleigh to Love waves ratios contained in seismic noise wave field 49

5- 1 HVIP analysis parameters selected through the preliminary tests: β = parameter controlling the filtering bandwidth; ldipp = maximum permissible inclination for planarity vector; nmin = minimum number of consecutive samples with coherent polarisation used to identify Rayleigh wave packets and rlim = rectilinearity thresholds used to distinguish Rayleigh from Love waves; fcmax= frequency of hvfcmax; hvfcmax= maximum of the H/V averages calculated from the analysis of the data among all comparison frequencies for comparison azimuths; nRfmax= number of samples of Rayleigh type for comparisons azimuth at the fcmax frequency; pRfmax= percentage of samples classified as Rayleigh for comparison azimuths on the total of those classified at the frequency fcmax; nRmed= average number of samples of Rayleigh type for the azimuths of comparison between all the comparison frequencies. 63

6- 1 Geotechnical properties of the slip surfaces 75
6- 2 The details of the profiles and inversion parameters 77
6- 3 Ambient noise stations with their corresponding amplification and directional resonance 89

Chapter 1

Introduction

1-1 Motivation

During all times of history, earthquakes have impacted the evolution of human beings by destroying towns, rising sea level, and creating slope failures. Among the factors responsible for slope destabilization, earthquakes play an important role in activating a large number of simultaneous mass movements. During the earthquakes, some seismic waves are released which have an impact on the structure of the medium where they are traveling. For example, seismic waves can reflect several times inside sedimentary basins, which not only results in amplifying the seismic motion but also extending them to longer durations.

Indeed, many cities are built on sedimentary basins which increase the seismic risk for these cities compared to the nearby locations. Therefore, even a moderate earthquake may cause serious damages to these cities. Site effect is the term used to characterize the impacts of modification of the seismic motion at a given site, which needs to be considered in seismic hazard risk assessment. Site effects can be studied using earthquake recordings, methods of imaging substratum (like borehole measurements or reflection and refraction methods).

The high expense of the above-mentioned methods besides their difficulty in deploying in populated areas drifts the attention to the surface waves methods specially in urban areas. Surface waves are dispersive, which means their velocity is a function of frequency and is directly linked to the soil structure. Moreover, Rayleigh waves have elliptical particle motion with the ellipticity that is also a function of frequency and linked to the soil structure. Therefore, surface waves analysis is useful to define the structure of sedimentary layers. Accurate measurement of the Rayleigh wave ellipticity helps to define the properties of subsoil structure and shear wave velocity profile.

The active surface waves methods are not always possible in urban areas and are limited to the superficial layers. Therefore, ambient noise, composed of both body and surface waves, becomes a more interesting alternative. One common approach that benefits the inversion of the ellipticity curve of ambient noise data to derive the subsoil properties is the known H/V method (Nakamura 1989). This method compares the ground motion recordings of the horizontal component with that of the vertical component at a site to obtain the resonance frequency which needs a thorough extraction of Rayleigh waves for an

accurate analysis. However, these methods are not able to define the actual wavefield composition. The key point to identify different wave types is through their polarisation mode.

A particle motion plot (hodogram) for a P wave is a line with the direction parallel to the direction of P wave propagation. The other wave with rectilinear particle motion is the shear wave with a difference that the line is perpendicular to the wave propagation direction. Ground roll is the other wave type that travels along or near the surface of ground, formed by the coupling of p waves and shear waves (SV) that propagates along a free surface (Sheriff 2002). The hodogram of the ground roll shows an elliptically polarised wave with retrograde particle motion, which its major axis is in the vertical direction. Using the three-component data would allow the estimation of wave polarisation and conclusively the precise detection of the wave types.

Taking advantage of the polarisation features for different waves, one can devise a filter to diminish one type of seismic wave and to enhance another type of seismic wave. Seismic recordings are often contaminated by noise which makes the recognition of minor seismic events difficult. Signal and noise can be separated by using polarisation filtering owing to the difference that exists in their polarisation features. Polarisation filters can improve the quality of 3-component seismic recordings by enhancing the signal-to-noise ratio (SNR) using the polarisation properties. A polarisation filter can be designed to enhance rectilinearly polarised waves (body waves) or surface waves while attenuates the other type.

Polarisation filters are applied in time or frequency domain depending on the wave content and the type of the event. In real seismograms, events with different frequency and different polarisation features may occur simultaneously and also, any particular frequency band may at two different times be dominated by events that do not have the same polarisation characteristics. Therefore, methods that consider polarisation variations and features of 3-component signals in the time-frequency domain are in priority. To target this aim, a robust time-frequency decomposition which renders high-resolution maps is in high demand.

1-2 Objectives

In this thesis, there are three principal goals as follows:

1- Develop a time-frequency decomposition which is robust against noise and has high resolution.
2- Devise a time-frequency polarisation filter to target the Rayleigh waves.
3- Study the site response via horizontal to vertical spectra of ambient noise using the polarisation filtering.

Two types of datasets were used in this thesis: synthetic data used in chapter 2 was generated in Matlab and the synthetic data used in chapter 3 was created from synthetic seismic code (Herrmann 2013). I provided the real data by carrying out the ambient noise acquisition in the Northern part of Iran. All the codes of this thesis were written in Matlab. The H/V spectral ratios were estimated (by Geopsy software), the Dinver and OpenHVSR software tools (Wathelet et al. 2004; Bignardi et al. 2016) were utilized for the inversion of H/V curves to obtain the shear wave velocity profile of the soil in the region.

1-3 Outline of thesis

This thesis contains six chapters that will be described as follows:

Chapter 1 is an introduction of the theme of the thesis, its motivation, objective, and the thesis overview.

Chapter 2 starts with the explanation of complex trace analysis and the way of its estimation. Then outlines a new time-frequency decomposition with some numerical examples to show the superiority of the proposed method to other state-of-the-art. In the introduced decomposition, the adaptive, sparse S transform (SST) is improved by a weighting function to provide stable and high-resolution instantaneous spectral attributes.

Chapter 3 gives definition of polarisation analysis. Then, the polarisation attributes are defined using some well-known methods. Finally, the proposed time-frequency polarisation method with its application on earthquake data are presented. The polarisation attributes are derived directly from the time-frequency spectra. The Rayleigh wave packets are filtered in an example using the proposed time-frequency polarisation filter.

Chapter 4 describes the ambient noise and its composition, then presents the horizontal to vertical spectral ratio method with the challenging ideas exist in this technique.

Chapter 5 explains the principles of polarisation analysis on ambient noise. Then the method is tested using synthetic data.

Chapter 6 shows the application of the polarisation analysis of ambient noise to study the possibility of defining directional site amplification that could influence land sliding on an unstable slop. The results obtained via the proposed method are verified via other geophysical and geotechnical techniques.

Chapter 7 contains the conclusion of this study with the achieved results.

Chapter 2

Complex seismic trace

2-1 Introduction

In signal analysis, transforming the data in different forms is common; therefore, to extract important information from seismic data, one needs to apply different techniques. Exchanging data from frequency domain to time domain or vice-versa is useful in data analysis. One way of transform is Fourier transform, which gives us the chance to survey the average properties of a significantly large portion of the trace, although examination of local variations is not possible. Complex trace analysis, which is a transform technique, analyzes seismic data similar to analytic signal. This kind of analysis can keep local significance and also is applicable in interpretation. Applying complex trace analysis helps obtain the amplitude and phase attributes. From the phase information, instantaneous frequency measurement basis and an attribute that is on its own can be obtained. The other attribute is amplitude which is named reflection strength. Other attributes can be obtained via combining the phase and amplitude information such as apparent polarity and weighted average frequency. Electrical engineering and signal analysis literatures also take advantage of complex trace analysis (Gabor 1946; Oppenheim, A.V. and Schafer 1975).

2-2 Calculation of the complex trace

2-2-1 Basic information

In complex trace analysis, f (t) plays the role of the real part and $f^{*}(t)$ is the imaginary part of an analytical signal. The imaginary part can be determined from f (t) by a linear convolution operation, which has the same amplitude spectrum as real trace but is 90 degrees out of phase with the real part. One of the perks of using complex trace, F (t), is defining instantaneous phase, frequency, and amplitude. The other advantage is its ability to detect the relative arrival times of a regular signal representing different traces more accurately. f (t) can be expressed in the following form $f(t) = A(t) \cos \Theta(t)$, where A(t) is time-

dependent amplitude and Θ (t) is the time-dependent phase. Therefore, the imaginary part defines as $f^{*}(t) = A(t) \sin \Theta(t)$. Finally, the complex F (t) is

$$F(t) = f(t) + jf^{*}(t) = A(t)\, e^{j\Theta(t)}. \quad (2\text{-}1)$$

A(t), reflection strength, and Θ(t), instantaneous phase, can be obtained if the f(t) and $f^{*}(t)$ are known (Bracewell 2000):

$$A(t)=[f^2(t)+ f^{*2}(t)]^{1/2} =|F(t)|, \quad (2\text{-}2)$$

and

$$\theta(t)= \tan^{-1}[f^{*}(t)/f(t)]. \quad (2\text{-}3)$$

The functional dependence on time of these attributes is the reason for calling them "instantaneous". Time-dependent frequency can be achieved by the time derivative of time-dependent phase. In other words, instantaneous frequency is the time derivative of instantaneous phase.

$$d\theta(t)/dt= \omega(t). \quad (2\text{-}4)$$

Representing it into the convolution form would be as

$$\omega(t)=\int_{-\infty}^{\infty} d(\tau)\theta(t-\tau)d\tau, \quad (2\text{-}5)$$

where $d(\tau)$ is differentiation filter (Rabiner and Gold 1975, p. 164). In view of equations (2.3) and (2.4) one has:

$$\omega(t) = d/dt\ \{\tan^{-1}[f^{*}(t)/f(t)]\ \}, \quad (2\text{-}6)$$

which leads to

$$\omega(t) = \frac{f(t)\frac{df^{*}(t)}{dt} - f^{*}(t)\frac{df(t)}{dt}}{f^{2}(t) + f^{*2}(t)}. \quad (2\text{-}7)$$

2-3 Calculation of the quadrature trace (imaginary part)

The way of calculating the f*(t) and F(t) is similar. At first, they are defined by Fourier integral afterward in terms of convolution in time domain with Hilbert transform. Assuming f (t) be real and defined in the range $-\infty < t < \infty$, the Fourier integral formula for it is

$$f(t) = \int_{-\infty}^{\infty} B(\omega) e^{j\omega t} d\omega, \tag{2-8}$$

And

$$f(t) = \int_{0}^{\infty} c(\omega) \cos[\omega t + \phi(\omega)] d\omega,$$

where $c(\omega) = 2|B(\omega)|$, and $\phi(\omega) = \arg B(\omega)$, $\omega > 0$ then

$$f^*(t) = \int_{0}^{\infty} c(\omega) \sin[\omega t + \phi(\omega)] d\omega, \tag{2-9}$$

and

$$F(t) = \int_{0}^{\infty} c(\omega) e^{j[\omega t + \phi(\omega)]} d\omega$$

while the phase $\Phi(\omega)$ is unchanged. The complex trace amplitude $c(\omega)$ is double when $\omega > 0$ and eliminates if $\omega < 0$. Rabiner and Gold (1975) present a similar formula for f*(t) by the Hilbert transform

$$f^*(\tau) = \frac{1}{\pi} P.V. \int_{-\infty}^{\infty} \frac{f(t)}{\tau - t} dt, \tag{2-10}$$

where PV $\int_{-\infty}^{\infty}$ means the Cauchy principal value

$$PV \int_{-\infty}^{\infty} = \lim_{\varepsilon \to 0} [\int_{-\infty}^{t-\varepsilon} + \int_{t+\varepsilon}^{+\infty}]. \tag{2-11}$$

The quadrature trace can be formed by applying Hilbert transform to the real trace by the convolution operation

$$f^*(t) = P.V.\int_{-\infty}^{\infty} = \lim_{\varepsilon \to 0}[\int_{-\infty}^{t-\varepsilon} + \int_{t+\varepsilon}^{+\infty}\ ]\frac{1}{\pi}\sum_{n=-\infty}^{\infty} f(t-n\Delta t)\frac{1-e^{j\pi n}}{n}$$

n≠0, (2-12)

$$f^*(t) = \frac{2}{\pi}\sum_{n=-\infty}^{\infty} f(\mathrm{t}-n\Delta\,\mathrm{t})\frac{\sin^2(\frac{\pi n}{2})}{n}$$

and from quadrature trace to real trace by applying the inverse convolution. The complex trace F (t) can be imagined as the trace in complex space of a vector which is frequently altering its length and rotating, graphically represented by a spiral shaped curve as illustrated in Fig. 2-1.

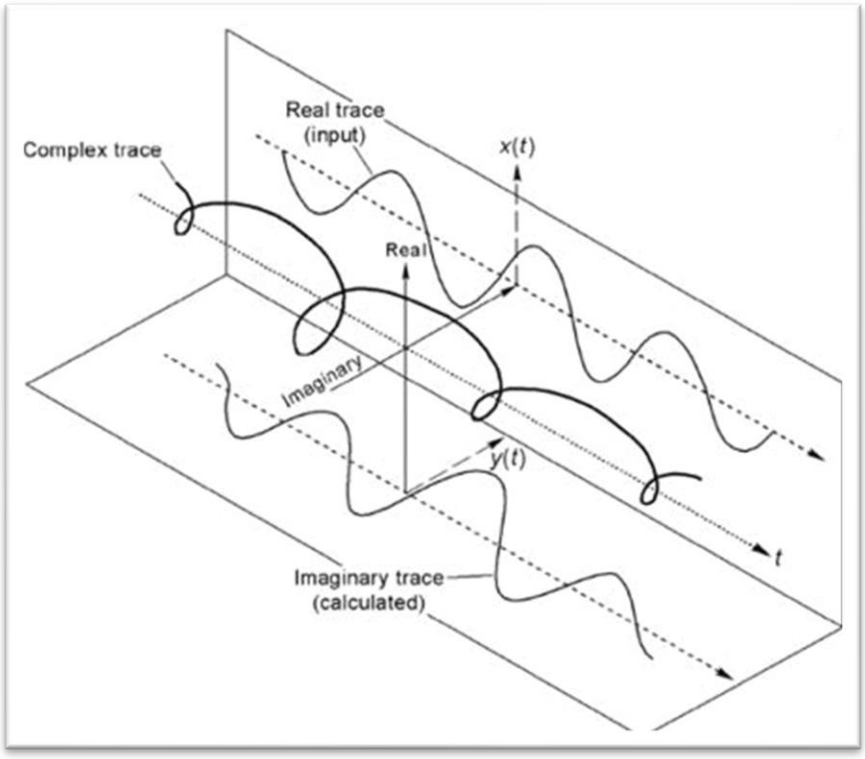

Fig. 2- 1 Isometric diagram of an actual seismic trace.

A(t) and θ(t) can be regarded as time-varying modulus and argument, respectively. The trace projection of the rotating vector on the real and imaginary planes present the real and quadrature (imaginary) traces, respectively. The angle of the vector with the horizontal plane is θ(t) while A(t) shows its length. The

reflection strength, A(t), is called the envelope of the seismic trace. Assuming A (t) like beads on a string rotating about the time axis, the arrival of new energy is shown by each bead. Every-time the rotating vector is locking onto new energy, an acutely leap is seen in the instantaneous frequency curve while during each bead of energy a significant change cannot be seen (Taner et al. 1979).

2-4 High resolution time-frequency Hilbert transform using sparsity-aware weighting function

2-4-1 Introduction

Despite the efficiency of conventional seismic methods in the interpretation of geological features, these methods do not necessarily ascertain all of the subtle geological features. One way of addressing this problem is the use of instantaneous complex attributes (Ville 1948), that are derived from complex traces and can potentially detect stratigraphic and geological properties (Taner et al. 1979). The physical parameters of the subsurface (such as absorption, velocities, and reflection coefficients) can be inferred from the amplitude of the seismic data, while the phase is usually useful for recognising the geometry of other features, such as a reflector dip and azimuth (Wang *et al*. 2019) and discontinuities related to structural anomalies, such as faults and channels (Yuan *et al*. 2019). Moreover, the dominant-frequency attribute can be used to delineate the features of hydrocarbon-bearing reservoirs (Ali *et al*. 2019). The susceptibility of these attributes to noise, however, has limited their applications in seismic interpretation.

Noise effects are a ubiquitous problem in seismic data analysis and can often impede the signal reconstruction. Various techniques have been proposed to address this problem (Li *et al*. 2015; Zhang et al. 2015; Xue *et al*. 2019). A generalised version of the Hilbert transform (GHT) has been presented to address this obstacle (Luo *et al*. 2003). Also, the time-frequency representation (TFR) of the instantaneous spectral attributes was proposed to detect thin-beds and channels (Liu and Marfurt 2007). Moreover, a zero-phase adaptive filter has been added to the windowed Hilbert transform (WHT), in order to make the instantaneous complex attributes more robust against noise (Lu and Zhang 2013). Recently, a fast, sparse S-transform was introduced to avoid losing the original data during filtering (Sattari 2017). The method, however, is still sensitive to random noise. Therefore, in this thesis, the adaptive, sparse S transform (SST) is improved by a weighting function to provide stable and high-resolution instantaneous spectral attributes, which considers the abrupt changes in the frequency content of the signal and is robust against noise. The main

procedure in this method is the use of sparsity-based window-parameter optimisation to increase the signal resolution. Furthermore, it applies a weighting function to the time-frequency domain, to diminish the noise in the computation of the analytic signal.

2-4-2 Methodology

In this section, we compute the analytic signal in the time-frequency domain. The analytic signal is then enhanced by utilising the SST. The sparsity-aware weighting function is then introduced to improve the resolution of the analytic signal generated by the SST.

2-4-2-1 Analytic signal using adaptive sparse ST

The similarity in the adaptive fast SST introduced by Sattari (2017) and the conventional ST proposed by Stockwell et al. (1996) is in retaining the absolute phase information (Boashash 2015) and the computational complexity, since both need to transfer the signal to the frequency domain first. The notable difference in the adaptive SST algorithm is the use of the optimised windows height and length, where the windows are adaptively varying to translate the spectrally varying signal. The best criterion to sparsify the time-frequency (TF) map is based on the strength or weakness of the spectrum amplitudes. However, the problem in frequency-dependent, conventional ST is that the translation of the frequency components cannot be obtained adaptively for the amplitudes. Sattari (2017) first applied this strategy by exploiting the matrix formula of ST described by

$$\mathbf{TFR}_{ST}^{[l]}[l,k] = IFT\left\{\mathbf{A}_{\mathbf{s}[l]}[l,m] \odot \hat{X}[l,m]\right\}, \tag{2-13}$$

in which $\boldsymbol{A}_{\boldsymbol{s}[l]}[l,m] \in \mathbb{R}^{N\times N}$ is the desired adaptive windows matrix. The columns of this matrix are constructed by the shifted random windows in the shape of $\boldsymbol{a}^{\boldsymbol{s}[l]}[m+l\text{-}1]$ and the rows, via the standard Gaussians in the shape of $g^{\boldsymbol{s}[m]}[m+l\text{-}1]$, where g is the window function as we move alongside the frequency axis, employing $m=0,\ldots,N\text{-}1$. Moreover, $1\leq k\leq N$ and $1\leq l\leq N$ are the time and frequency indices, respectively, and $\boldsymbol{s}[l]$ denotes the standard deviation of the window function that plays the role of frequency dependent support of g. $\widehat{\boldsymbol{X}}[l,m] \in \mathrm{C}^{N\times N}$ represents the frequency domain of the input signal $\boldsymbol{x}[l]$ with N elements repeated m times. Furthermore, operators $\odot$ and IFT represent the Hadamard product of the two matrices and the inverse Fourier transformation, respectively. Sattari (2017) used the important information included in the amplitude spectrum of the input signal to separate the high and low amplitude frequency components, conforming to their known positions. Ultimately, the amplitude spectrum is used to produce sparsity through the computing $a(\boldsymbol{s}[l], m)$ as an optimised function of l for each m. This complicated two-

dimensional problem is employed by switching the optimisation direction from frequency to frequency shift (Sattari 2017).

Due to the inter-relation of *l* and *m* under the matrix formula, we can utilise the linear program proposed by Sattari (2017) to modify the optimisation direction through a simple transpose in the ST algorithm. This modification results in optimised, standard voice Gaussians along the frequency shift (rows of $\boldsymbol{A}_{\mathbf{s}[l]}[l,m\,]$), where smooth and differentiable random windows are automatically attained along frequency (columns of $\boldsymbol{A}_{\mathbf{s}[l]}[l,m\,]$). The voice Gaussians window-length $\mathbf{s}[l]$ is supposed to be a curve, reversely proportional to the smoothed amplitude spectrum $\left|\widehat{\boldsymbol{X}}_{\varsigma u}[l]\right|$ with a scale between zero and one (Eq. 2-14).

$$\mathbf{s}[l\,] = \frac{N}{2} * \frac{1}{\left\{r * \left|\hat{\mathbf{x}}_{\varsigma\,\mathrm{u}}[l\,]\right|\right\} + 1} \tag{2-14}$$

The optimisation sensitivity to random noise can be efficiently repressed by the smoothing method (Sattari 2017). The range of the curve varies from 1 to $r + 1$ using $\{r * \left|x'_{\varsigma u}[l]\right|\} + 1$, thus, the reciprocal term is in the range $1/(r + 1)$ and 1. Note that the free parameter r plays an important role in ascertaining the range, the lower boundary, and the windows size. If we increase r, we get a smaller lower boundary and broader range. This implies narrower windows with larger heights in the frequency domain to localise spiky components. The symmetry of $\boldsymbol{x}[l]$ helps us to be able to select the greatest possible window-length as N / 2, fixed for zero amplitude frequency components, while the parameter *r* sets the smallest *s*. The range of $\boldsymbol{s}[l]$ is controlled by the parameter *r*, which is readily adjustable, owing to its linear behaviour. For example, according to their bandwidth and spectral diversity, we can select r as being equal to 1 or 2 for band-limited signals, 3 or 4 for seismic signals, and 5 to 10 for wide-band signals.

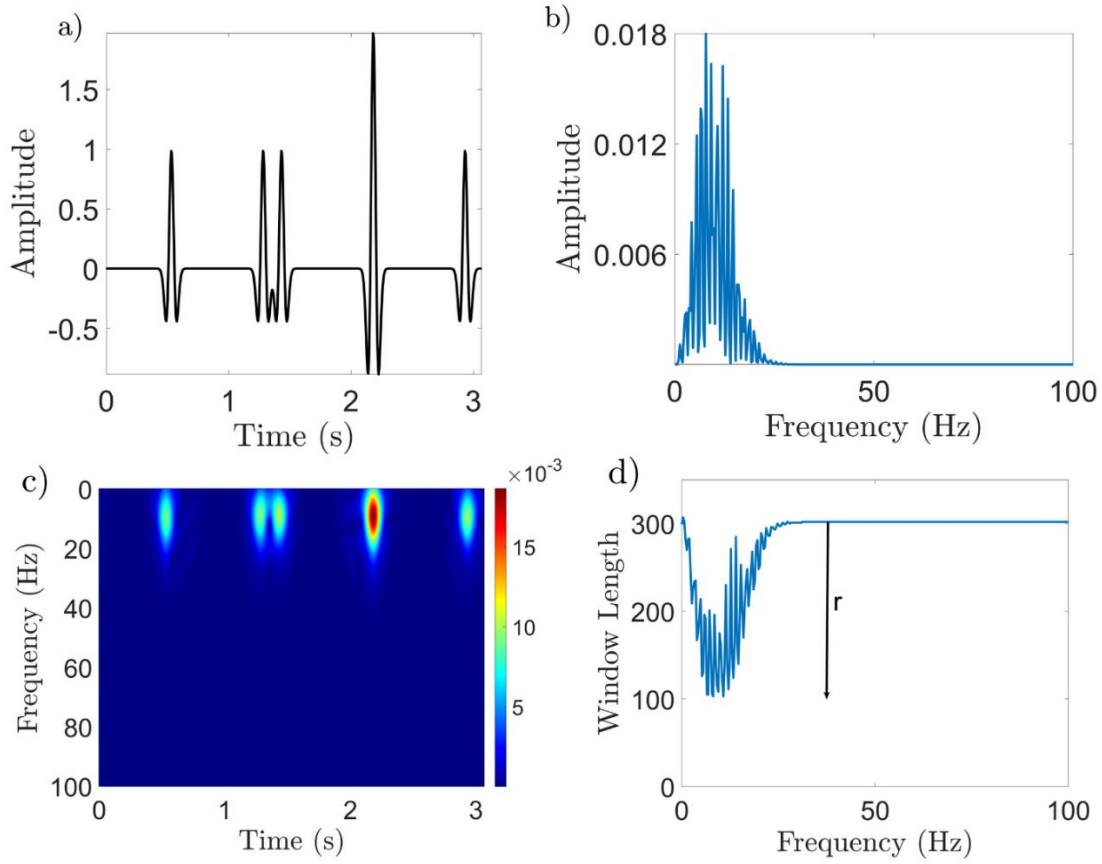

Fig. 2- 2 a) A multi-component signal with several Ricker wavelets, b) the corresponding amplitude spectrum, c) the SST time-frequency map of the signal computed by (d) the window-lengths reversely proportional to the amplitude spectrum shown in b (Parameter r *is chosen to be 1 for this signal because it is a narrowband and not spectrally diverse).*

It is worth mentioning that, neither energy concentration maximisation methods (ECM) nor generalised versions of the ST are user-friendly and efficient in terms of free-parameters (Radad et al. 2015b). In Fig. 2-2, we present how parameter *r* sets the range of window lengths using the amplitude spectrum in Eq. (2-14) for this purpose. The wavelets central frequencies, with the high amplitude components in 10 Hz, are presented in Fig. 2-2c. These components were translated with narrow windows, which inevitably have great heights to clearly resolve the interfered wavelets in the TF domain, owing to the localisation of their central frequency. Parameter *r* is taken as 1 for this signal since it is a narrow band and has low spectral diversity.

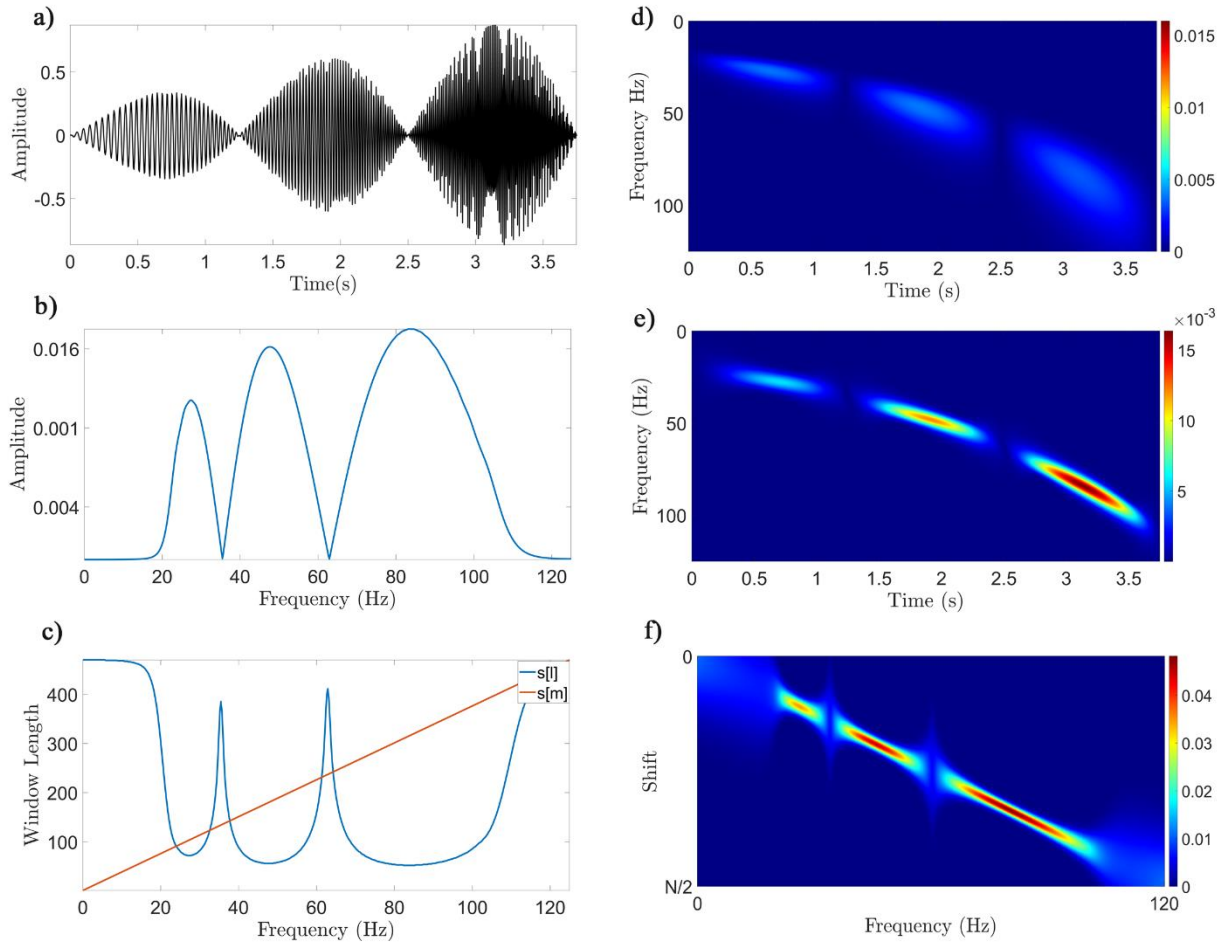

Fig. 2- 3 a) A non-stationary logarithmic chirp signal, b) the correspondent amplitude spectrum, c) window length variation with frequency in terms of sample numbers for conventional ST (red line) and adaptive SST (blue line). The time-frequency map of the non-stationary signal was computed by d) the conventional ST and e) adaptive sparsity, using the adaptive arbitrary windows, f) the desired matrix of adaptive windows with shifted arbitrary windows.

The performance of the adaptive SST and conventional ST is compared in Fig. 2-3 by using 1330 samples in a logarithmic chirp signal with 3 ms sampling intervals and amplitude variations, in both the time and frequency domains. Fig. 2-3c compares the adaptive window-length variation of the SST with the non-adaptive frequency-dependent window-lengths of the conventional ST. Using more zeroes and fewer, but larger amplitudes when calculating the TF maps by the SST, makes the spectral coefficients sparser and results in higher resolution and adaptivity (Figs. 2-3d and 2-3e). The comparison of the TF maps of the input signal (Fig. 2-3a) shows that conventional ST has led to erroneous amplitudes in the TF domain (Fig. 2-3d), low resolution and low adaptivity.

ECM methods were also used for improving the adaptivity of Fourier-based spectral decomposition (Jones and Parks 1990; Sattari et al. 2013; Radad et al. 2015b). Sattari (2017) discussed the performance of these methods and the SST method in detail. The computational expense of obtaining TF maps for ECM

methods is pN^2logN, which is p times heavier than that of conventional ST and adaptive SST (p is the number of TF maps need to be calculated by different window lengths in terms of sample number to optimise windows in ECM methods). Additionally, these methods are less adaptive, susceptible to noise, have lower resolution, and require more parameters for various signals.

The arbitrary windows of SST follow the criteria of the partition of unity (Lamoureux et al. 2003), which means that the superposition of them to the columns of $\boldsymbol{A}_{\boldsymbol{s}[l]}[l,m\,]$ onto the frequency axis, add up to 1. This characteristic makes the adaptive SST invertible similar to conventional ST by a simple projection of the SST map onto the frequency (Eq. 2-15).

$$\mathbf{x}[k\,] = \sum_{l=1}^{N} \mathbf{TFR}_{ST}^{[l\,]}[\,l\,,k\,] \tag{2-15}$$

Taking advantage of the information provided by the amplitude spectrum resulted in the development of an SST algorithm that is capable of creating a TF map which automatically adapts to all the temporal, spectral and amplitude variations (Figs. 2-2 and 2-3). The superior performance and computational complexity from using just one, well-behaved, free parameter suggests that the adaptive SST is an ideal alternative to conventional ST.

In this work, the analytic signal is calculated based on the decomposed signal from the SST (Sattari 2017), in order to benefit from higher resolution, in comparison to the conventional ST method. The TFR of WHT is defined by:

$$\mathbf{Z}(\omega,\tau) = \mathbf{X}(\omega,\tau)\left[1 + iH\,(\omega)\right] = \begin{cases} 2\mathbf{X}(\omega,\tau) & \omega > 0 \\ \mathbf{X}(\omega,\tau) & \omega = 0 \\ 0 & \omega < 0 \end{cases}, \tag{2-16}$$

where $\boldsymbol{\tau}$ is translation, $\mathbf{X}(\boldsymbol{\omega},\boldsymbol{\tau})$ is the TFR of the input signal obtained by the SST method, and $\mathbf{H}(\boldsymbol{\omega})$ is the Fourier spectrum of the sign function (Lu and Zhang 2013). In the next section, we apply a sparsity-aware weighting function to the TFR of WHT in Eq. (2-16), to address the suppression of the random noise that was not detected by the SST.

2-4-2-2 Sparsity-aware weighting function

The sparsest weight vector can be attained by utilising the ℓ_0-norm, however, problems involving this norm are intractable due to some serious difficulties, including (i) the outcome of the ℓ_0-norm is strongly sensitive to noise, (ii) in practice, sparse systems are compressible systems, and (iii) the ℓ_0-norm leads to an NP-hard problem (Natarajan 1995). NP-hard problems are the complexity class *of* decision problems

that are primarily harder than problems which can be solved by a non-deterministic Turing machine in polynomial time. If a decision version of a combinatorial optimisation problem is demonstrated to be a member of the class of NP-complete problems, then the optimisation version is NP-hard. In other words, NP-hard problems are those problems with efficient algorithms for verifying the correctness of a given answer but we do not know any efficient way of finding the answer to the problem.

Therefore, we can introduce the continuous weighting function $f_\beta(\omega)$ for a component ω so that

$$\lim_{\beta\to\infty} f_\beta(\omega) = \begin{cases} 1 & if\ |\omega| \neq 0 \\ 0 & if\ |\omega| = 0 \end{cases}, \tag{2-17}$$

where $\beta \in \mathbb{R}_+$ controls the sharpness of the weighting function and its sensibility to ω. Eq. (2-17) states that as β tends to infinity, $f(\beta)$ tends to the ℓ_0-norm. Furthermore, the function $f(\beta)$ must be continuous with a minimum and maximum equal to zero and one, respectively, and it ought to satisfy the following conditions:

$$\lim_{\omega\to 0} f_\beta(\omega) = 0 \quad \text{for} \qquad \beta \in \mathbb{R}_{+,} \tag{2-18}$$

$$\lim_{\omega\to \pm\infty} f_\beta(\omega) = 1 \ \text{for} \qquad \beta \in \mathbb{R}_+. \tag{2-19}$$

Many candidates for $f(\beta)$ satisfying conditions (2-17) to (2-19) can be adopted. However, in this work, we chose two candidates for $f(\beta)$, inspired by the Geman-McClure function (GMF) (Yazdanpanah and Diniz 2017) and the Laplace function (LF) (Lima et al. 2014), as follows:

$$g_\beta(\omega) \triangleq 1 - \frac{1}{1+\beta|\omega|}, \tag{2-20}$$

$$l_\beta(\omega) \triangleq 1 - e^{-\beta|\omega|}. \tag{2-21}$$

Note that both $g_\beta(\omega)$ and $l_\beta(\omega)$ satisfy Eqs. (2-17) to (2-19). Figs. 2-4a and 2-4b depict $g_\beta(\omega)$ and $l_\beta(\omega)$ for different values of β, respectively. As can be seen, when ω is close to zero, high values of β lead to a sharp decrease in $g_\beta(\omega)$ and $l_\beta(\omega)$; whereas, for large ω, these functions are approximately equal to 1. The drawback of the SST method in the suppression of random noise is addressed by applying the proposed weighting functions (2-20) and (2-21) to the TFR obtained in Eq. (2-13). The linear behaviour

of parameter β helps easy adjustment. For example, the range of β for band-limited signals can be 1 or 2 and, for seismic signals 3 or 4, depending on their bandwidth.

By selecting the appropriate β and applying the filter, the TFR of WHT turns into the weighting sparse s- transform (WSST). The WSST aims to achieve less noisy results by enhancing higher amplitude frequency components and diminishing the lower ones. An increase in the value of β results in the amplification of frequencies with the maximum amplitude. The value of β depends on the signal to noise ratio (SNR), the higher the SNR, the lower β. Although the SST is supposed to render less noisy results, it fails to suppress the noise when the SNR is low. On the other hand, the proposed adaptive filter by Lu and Zhang (2013) cannot distinguish the discrepancy between the desired signal and undesired noise if applied directly to the TFR. The weight factor proposed by Lu and Zhang (2013) reduces the noise at the cost of losing the signal and conclusively losing the subsurface information. Therefore, applying a weighting function to the obtained TFR in SST not only produces high-resolution TFR (as SST) but also suppresses the noise. Meanwhile, the superiority of the applied filter (compared to the RWHT) arises by maintaining the original signal while suppressing the remaining random noise. In this method, we first set the optimised window according to the spectrum amplitude and then choose the appropriate weighting function parameter, based on the SNR. These two parameters were chosen for seismic data analysis, through a process of trial-and-error.

Remark1: Note that the function $f(\beta)$ is non-convex, however, in our approach it does not cause any problems in exploiting sparsity since we do not require the gradient of $f(\beta)$ in the optimisation problem. Indeed, this function only applies to the TFR matrix to generate the appropriate weights for the components. Moreover, the weights obtained by this function are more effective than the weights inspired by the ℓ_1-norm. In other words, the ratios of the weights to their corresponding components in the TFR matrix always have absolute values equal to one. However, by utilising the function $f(\beta)$, the absolute values of these ratios for small components are less than one and, for large components, are close to one. Therefore, in the proposed strategy, small components tend to zero with a higher intensity, compared to methods using the ℓ_1-norm.

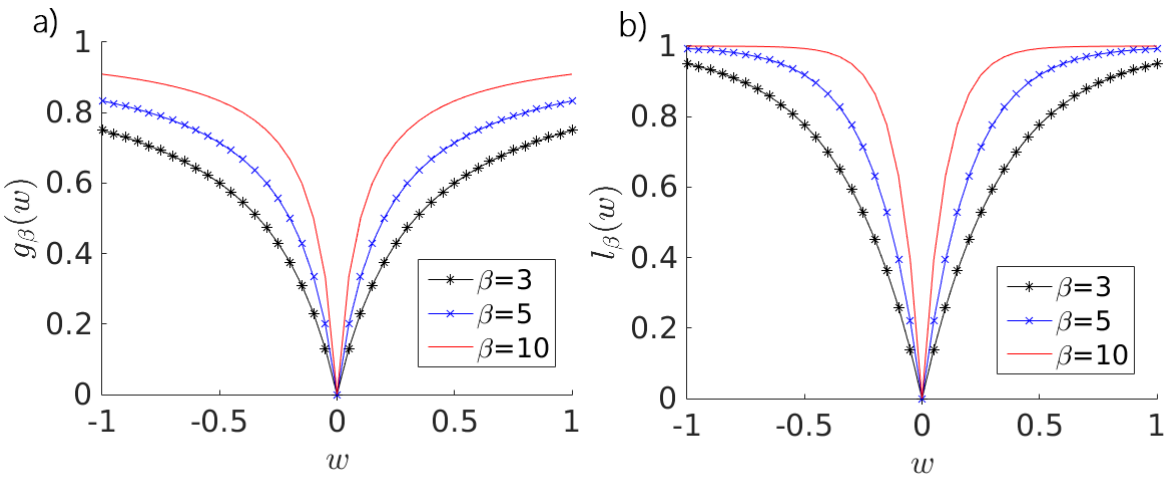

Fig. 2- 4 Graphs a) $g_\beta(\omega)$ *and b)* $l_\beta(\omega)$ *for different values of* β .

2-4-3 Experimental results

In this section, the proposed method utilises the weighted SST (WSST), the SST, and the RWHT in synthetic data sets. First, the numerical results for the synthetic data are presented in Subsection A. The noise is zero-mean, white Gaussian noise.

The first example is a double-linear chirp signal with a sampling interval of 2 ms and maximum time of 2 s. The efficiency of the two proposed weighting functions (the LF and the GMF) were tested. As can be seen in Fig. 2-5, the LF retains the energy of the desired signal better than the GMF, not only for the noise-free case but also for the noisy case, when the white Gaussian noise (with 1 dB SNR) is added to the original signal. The arrows in Fig. 2-5 indicate the regions where the desired signal faded due to the attenuation of the noise.

In this example, different values of β are tested, since this parameter needs to be selected with care. We observed that the lowest value of β (equal to 1) suppresses all of the noise but damages the original signal as well, due to its sharp decrease. On the other hand, the highest value of β (which is 10 in this example) is unable to present a clear TF map for the noisy signal. Finally, β of around 5 gives the most reasonable trade-off between maintaining the desired signal and attenuating the noise. From now on, we depict the results of WSST utilising the LF as both functions attenuate the random noise to a similar extent but the LF maintains the desired signal better than GMF.

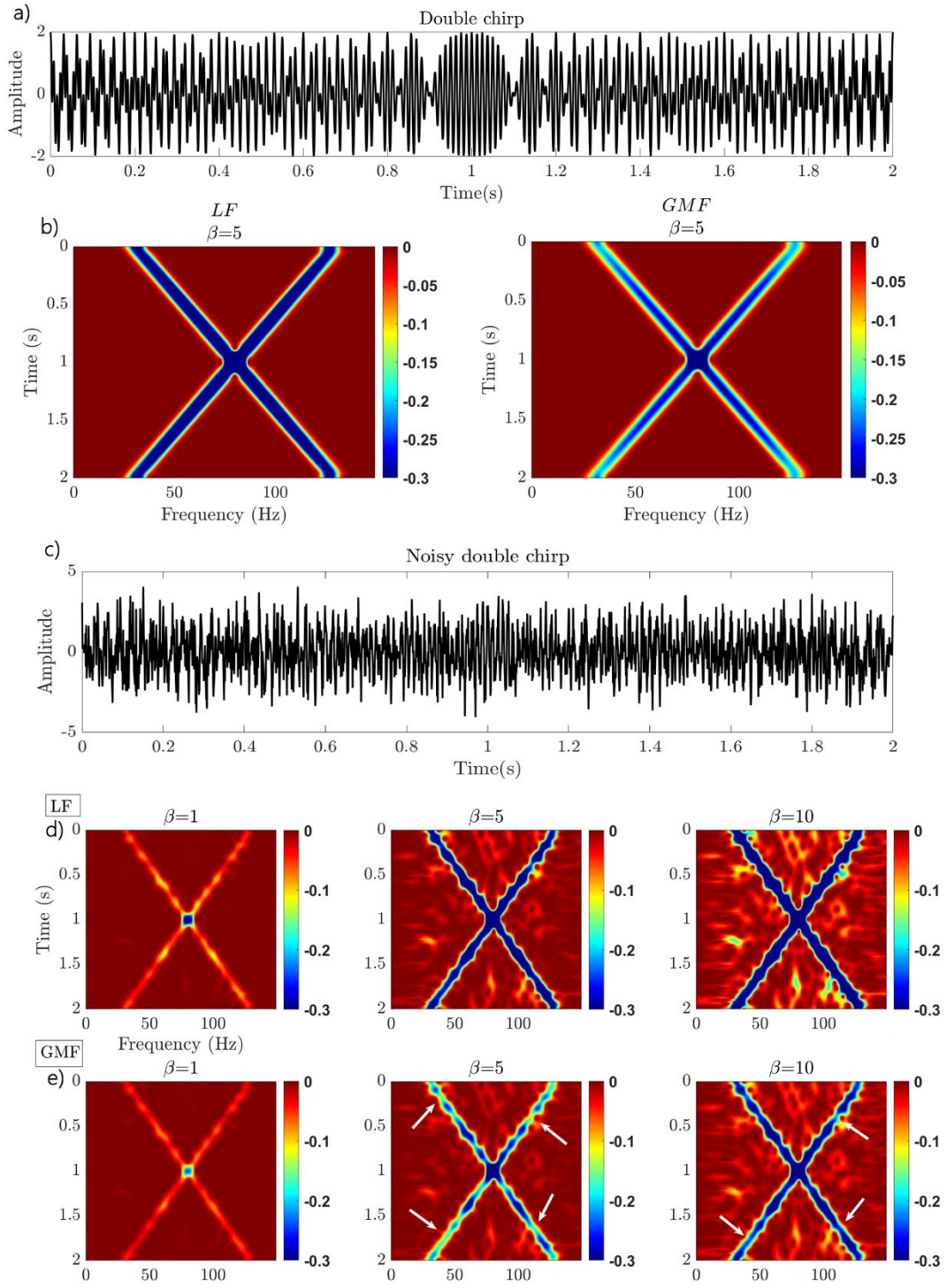

Fig. 2- 5 a) Double chirp signal, b) its time-frequency panel for the WSST method using the LF and the GMF. c) Noisy double chirp signal, d) its time-frequency panel for the WSST method using the LF and e) the GMF. The white arrows show the effect of GMF where the desired signal is lost.

In Fig. 2-6, by adopting the same signal as Fig. 2-5, the performance of the WSST, ST, SST and the RWHT in retrieving the TF map is illustrated. In this example, the parameters chosen are β = 2.5 for the WSST, r = 30 for the SST and the WSST, and N = 1.5 for the RWHT.

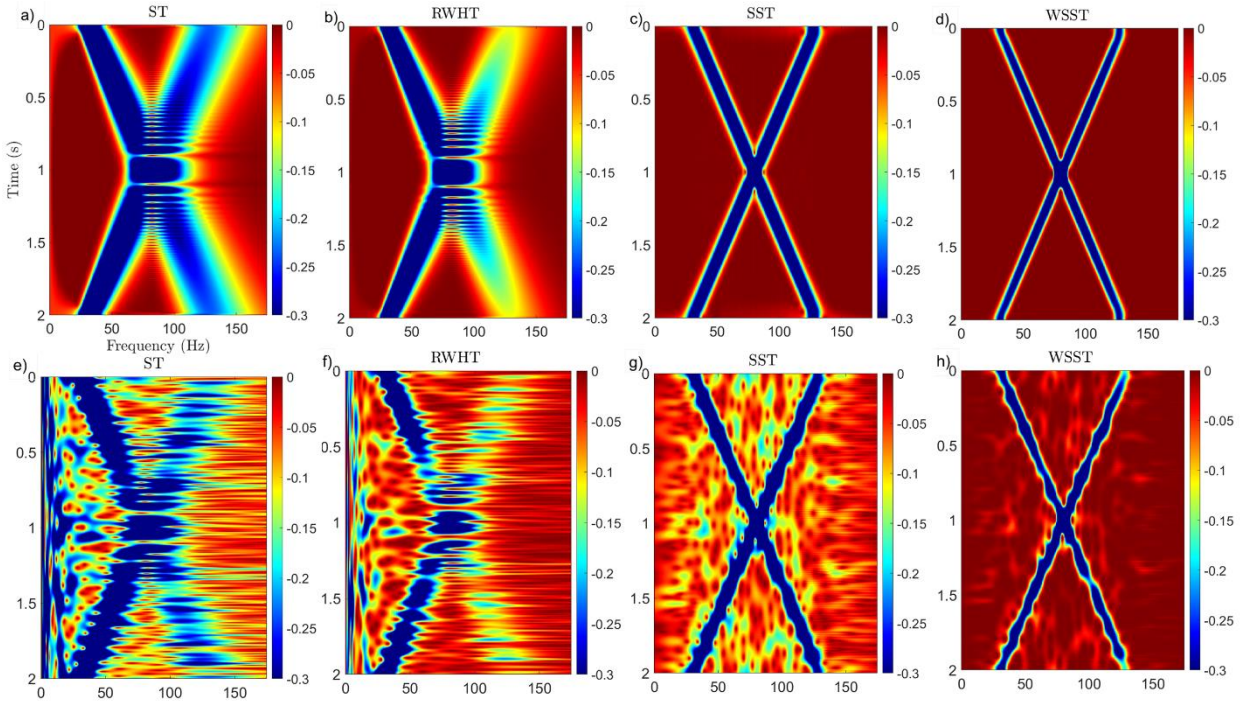

Fig. 2- 6 Time-frequency panel for Double chirp signal with four methods, ST, RWHT, SST, and WSST (a-d), and the noisy form (e-h).

As can be seen, in the case of both clean and noisy data, the WSST has the highest resolution, while the ST and RWHT are unable to reconstruct the signal, particularly in the noisy situation. For RWHT, the right-hand side of the panel has lost its information in both cases. In the noisy case, the SST method retrieves the signal but is still unable to remove the noise completely, while the WSST not only retains the signal but also suppresses the additive noise.

To demonstrate the superiority of the WSST over the SST and the RWHT in decomposing narrowband signals, we have compared the TFR of 5 non-stationary signals in Fig. 2-7. The signal was taken from Andrade, Porsani and Ursin (2018) and it comprises two harmonic components of 15 Hz, $\boldsymbol{x}_1(t)$, and 35 Hz, $\boldsymbol{x}_2(t)$, a frequency-modulated harmonic of about 65Hz, $\boldsymbol{x}_3(t)$, a sliding harmonic from 35 to 158 Hz, $\boldsymbol{x}_4(t)$, and a Morlet wavelet with a central frequency of 113 Hz, $\boldsymbol{x}_5(t)$. The signals were generated by a sampling interval of 0.003 s, and given by

$$\begin{cases} \boldsymbol{x}_1(t) = 0.8\cos(30\pi t) & 0 \le t \le 6s \\ \boldsymbol{x}_2(t) = 0.6\cos(70\pi t) & 0 \le t \le 6s \\ \boldsymbol{x}_3(t) = 0.7\cos(130\pi t + 5\sin(2\pi t)) & 4s \le t \le 8s \\ \boldsymbol{x}_4(t) = \sin\left(\dfrac{8\pi 100^{t/8}}{log(100)}\right) & 6s < t \le 10s \\ \boldsymbol{x}_5(t) = 3e^{-1250(t-2)^2}\cos\big(710(t-2)\big) & 0 \le t \le 10s \end{cases}.$$

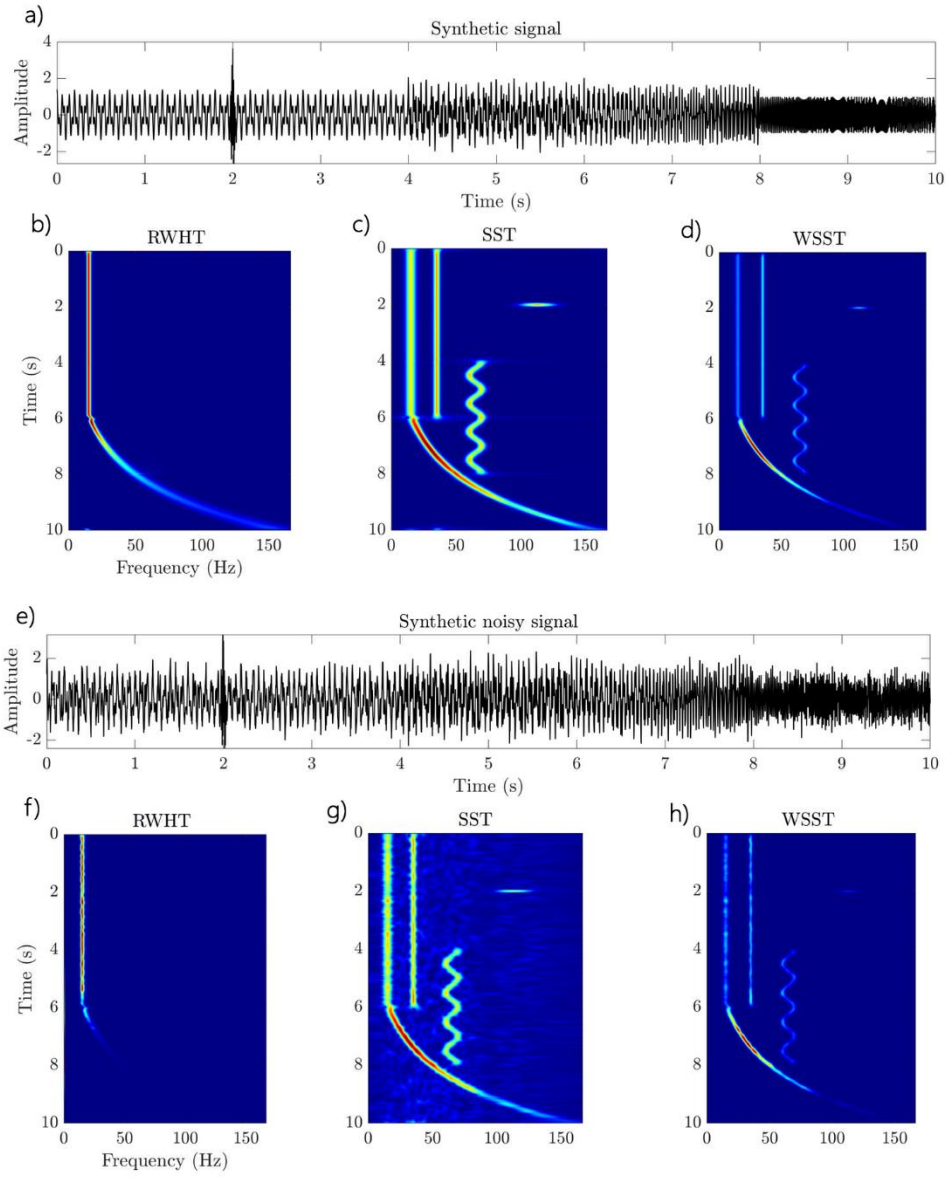

Fig. 2- 7 a) Synthetic signal, and b) time-frequency panels for the RWHT, c) the SST, and d) the WSST methods. e) Synthetic noisy signal and, f) time-frequency panels for the RWHT, g) the SST, and h) the WSST methods.

In this example, the values of the input parameters are the same. We set the value of β to be 2 owing to the narrowband feature of the signal. The filtering effect of the RWHT method can be observed in the

TF panel as the energy of the signals are attenuated and results in the loss of the desired signal $\boldsymbol{x}_2(t)$, $\boldsymbol{x}_3(t)$, and $\boldsymbol{x}_5(t)$. The SST method blurs the TF panel and is unable to accurately localise the signal in both the time and frequency domain. For example, the signal $\boldsymbol{x}_5(t)$, which has the central frequency of 113 Hz, is localised between 100 and 130 Hz. Moreover, the other signals are not clearly resolved in the TF domain due to the spectral leakage, especially in the low frequency components at a time of 10 s and in other frequency components at 4, 6 and 8 s. As can be seen in Fig. 2-7, the WSST method proves its capability in obtaining a high-resolution TF spectrum without losing the energy of the signal. As for the noisy case, the SST is unable to render a clear TF map, while the WSST completely removes the random noise added to the desired signal. This is the result of employing the sparsity properties of SST and the filtering effect of the proposed weighting function.

2-4-4 Conclusion

In this chapter, a stable and high-resolution time-frequency decomposition is proposed within the framework of a sparsity-based optimisation and weighting function. Indeed, by using the Geman-McClure and Laplace functions, the weighting function has been incorporated into the existing SST approach, to introduce the WSST method. The fundamental role of the weighting function is to enhance the frequency components with the larger amplitudes proposed by the SST technique and to attenuate the components with low amplitudes but without eliminating the desired signal. In the proposed method, the need for regularising the abrupt changes are satisfied with the optimised windows and the remaining random noise is suppressed via the devised weighting function. The results have shown the superiority of the proposed method in obtaining robust and high-resolution time-frequency maps compared to the previously introduced methods (ST, SST, and RWHT).

The computation complexity of the proposed method is slightly higher than the SST, however, its computational efficiency is much better than the RWHT method, since RWHT requires the inverse Fourier transform. It is worth mentioning that these weighting functions can be joined to other techniques, such as approaches utilising short-time Fourier transform. Finally, the numerical results demonstrate that the proposed WSST method outperforms the other state-of-the-art strategies in removing noise.

Chapter 3

Wave polarisation analysis

3-1 Literature review

The acquisition of multicomponent seismic data is highly common in most studies of earthquakes and in some borehole and surface seismic exploration studies. Gabor (1946) studied the minimum bandwidth for the transmission of radio and television signals in studying the complex analytical signal. Whalen (1971) named the complex analytic signal the pre-envelope and the Farnbach (1975) called it complex envelope. Stratton (1941) studied the characterization of harmonic electromagnetic (EM) waves with elliptic polarisation. The polarisation of narrowband EM radiation was investigated by Wolf (1959) using a coherency matrix and Gabor's concept of the analytic signal. To determine the coherency matrix and parameters of elliptic polarisation of light, Wolf (1959), Parrent and Roman (1960) explained physical experiments using an intensity meter, a polarizer, and a compensator which produces a phase shift. In EM prospecting, elliptic polarisation of monochromatic fields was defined in Dey and Ward (1970) and Smith and Ward (1974).

Shimshoni and Smith (1964) describe the polarisation of multicomponent seismic signals by decomposing vertical and radial horizontal components of motion into Fourier components. As concerns of analyses similar to Shimshoni and Smith (1964), comparatively short sliding data windows are necessary since the seismic signals are nonstationary. In the case of having large data set, this method is computationally expensive. In polarisation investigations of earthquake and nuclear explosion seismograms, time-averaged cross products of vertical and horizontal components of motion were devised by Shimshoni and Smith (1964). Sutton and Pomeroy (1963) applied cross products of seismic components by considering analog analysis of seismic data. To digitize earthquake seismic data, Farnbach (1975) used complex signal analysis to calculate envelope and instantaneous phase to improve the definition of arrival times of various phases. Goebel (1984) placed vertical component in the real part and horizontal component in the imaginary part of a complex seismic trace. Since one component is 90 degrees out of phase with the

other, the Fourier transform of that trace is modified before inversion to attenuate elliptically polarized waves. As Aki and Richards (1980) mentioned, all types of waves (P, S, Rayleigh and Love) have distinct polarisation, which can be useful in identifying the phases on 3-component seismograms.

The first problem arises when several energies arrive at the same time, which makes the polarisation recovery hard even on either arrival. Another one is related to the conversion of P and S waves at the free surface for P-SV energy, which results in phase discrepancy between different components of motion for incident SV waves (Nuttli 1961) and Rayleigh surface waves (Aki and Richards 1980). Vidale (1986) proposed a low degree of polarisation method for the multiple arrivals, which applies analytic signal to control elliptical polarisation.

In the laterally homogeneous earth, vertical and radial components indicate the Rayleigh waves while the transverse shows the Love waves. To separate body waves (except SH body waves) from Rayleigh waves, a two-dimensional polarisation analysis of the vertical and radial components is adequate, since body and Rayleigh waves have linear and elliptical polarisations, respectively. As long as laterally heterogeneous earth, the two-dimensional polarisation cannot isolate P-SV and SH onto vertical and radial and transverse components, therefore a three-dimensional one can be a proper alternative in recognition of the arrivals.

3-2 Complex polarisation analysis of particle motion

A simple definition of polarisation analysis is the rotation of motion into vertical, radial, and transverse components and studying them visually (Vidale 1986). By this analysis, it is possible to detect the polarisation orientation approximately and possibly to define whether the components are in phase for a special arrival. The application of polarisation filters introduced by Montalbetti and Kanasewich (1970) is to automatically intensify the highly polarized portion of the signal. Samson and Olson (1980) mentioned some theoretical points in their papers. Moreover, Smart and Sproules (1981) designed a polarisation filter to define the back-azimuth.

3-2-1 Methodology of complex polarisation

In 3-component seismogram data, three-time series which are related to each component is available. For the radial component, $u_r(t)$, the positive direction is outward; the transversal component, $v_r(t)$,

has a positive orientation in the clockwise direction; and the vertical component, $w_r(t)$, presents its positive value in an upward direction.

$$\begin{aligned} u(t) &= u_r(t) + iH(u_r(t)) \\ v(t) &= v_r(t) + iH(v_r(t)) \\ w(t) &= w_r(t) + iH(w_r(t)) \end{aligned} \tag{3-1}$$

The Hilbert transform is defined by H and i is the square root of -1, $\sqrt{-1}$. The covariance matrix can be calculated by analytical signal.

$$c(t) = \begin{pmatrix} uu* & uv* & uw* \\ vu* & vv* & vw* \\ wu* & wv* & ww* \end{pmatrix} \tag{3-2}$$

Complex conjugation is represented by asterisks. Malvern (1969, p.92) analytically calculated the three eigenvalues λ_i and eigenvectors (x_0, y_0, z_0) of the covariance matrix.

$$\begin{bmatrix} x_i \\ y_i \\ z_i \end{bmatrix} \left[c - \lambda_i I \right] = 0 \quad \text{i=1, 2, 3} \tag{3-3}$$

The covariance matrix has real positive eigenvalues and complex eigenvectors since the matrix is Hermitian. The greatest amount of polarisation is presented by the largest eigenvalue λ_0 related to the eigenvector (x_0, y_0, z_0). In the first step, the length of the eigenvector is normalized to be 1. Then by rotating the eigenvector related to the largest eigenvalue by 0 to 180 degree in the complex plane, the rotation that results in the largest real component can be achieved. This rotation can be defined by seeking over $\alpha = 0^O$ to 180^O for maximizing the length of the real component of the eigenvector, X.

$$X = \sqrt{(\mathrm{Re}(x_0 cis\,\alpha))^2 + (\mathrm{Re}(y_0 cis\,\alpha))^2 + (\mathrm{Re}(z_0 cis\,\alpha))^2} \tag{3-4}$$

In the above equation $cis\alpha$ is $\cos\alpha + i \sin\alpha$ and Re(x) is the real part of x. The vector (x_0, y_0, z_0) is then rotated by the angle α, and the elliptical component of polarisation can be computed by

$$P_E = \frac{\sqrt{1 - X^2}}{X} \tag{3-5}$$

$\sqrt{1-X^2}$ represents the length of the complex part of the eigenvector, since the eigenvector is normalized. Therefore, P_E is the ratio of the imaginary part to the real part of the eigenvector. In the case the value of P_E shows zero, it is linearly polarized motion, and if it is 1, it refers to the motion which is circularly polarized. Comparison of the real and imaginary parts signs of the rotated vector can be practical in rectifying the ambiguity for the propagation direction of fundamental Rayleigh waves, which have retrograde polarisation (Vidale 1986). Different types of polarisation, linear, prograde, or retrograde, can be seen if a random combination of Rayleigh modes is involved. The strike and the dip of the direction of maximum polarisation are defined in Eqs. (3-6) and (3-7), respectively.

$$\phi = \tan^{-1}\left(\frac{\mathrm{Re}(y_0)}{\mathrm{Re}(x_0)}\right) \tag{3-6}$$

$$\delta = \tan^{-1}\left(\frac{\mathrm{Re}(z_0)}{\sqrt{\mathrm{Re}(x_0)^2 + \mathrm{Re}(y_0)^2}}\right) \tag{3-7}$$

The ambiguity in the polarisation vector arises when the vector (x, y, z) has similar polarisation as (-x, -y, -z). The dip and strike in Eqs. (3-6) and (3-7) are in the range of -90^O to 90^O; in that case a vector pointed horizontally to the direction back to epicenter is defined by 0^O strike and dip. The strikes in the ranges -180^O to 90^O and 90^O to 180^O have ambiguity so are not represented. The same applies for the other two eigenvalues λ_1 and λ_2. The eigenvalue λ_2 is relevant to the eigenvector which is directed to the intermediate polarisation while λ_3 is related to the eigenvector with the direction of least amount of polarisation. As eigenvectors associating with λ_0, λ_1, λ_2 are orthogonal, polarisation components would be gained orthogonal. The strength of polarisation in the signal is defined as

$$P_S = 1 - \frac{\lambda_1 + \lambda_2}{\lambda_0} \tag{3-8}$$

If just one component shows polarisation, the P_S is approximately 1, which means that the signal is completely polarized, on the other hand, if P_S is around 0 it means that all three components have the same amount of polarisation. The degree of planar polarisation in the signal can be presented as

$$P_P = 1 - \frac{\lambda_1}{\lambda_2} \tag{3-9}$$

In the case that the intermediate component has much higher value in comparison with the smallest component, P_P shows 1, while if it has the value 0, the two components are nearly the same.

3-3 Polarisation attributes defined by Rene (1986)

The relationship between elliptic polarisation and phase difference for harmonic signal, the semi-major and semi-minor axis lengths, tilt angle τ, and "rise angle" Υ of the polarisation ellipse are depicted in Fig. 3-1. Particle motion up and away from the source is shown on positive axes. Retrograde and prograde polarisation can be defined by the sign of phase difference Φ. While the positive values associated with retrograde, negative is representative of prograde motion. Linear polarisation with forward and backward tilt are shown by 0 and π radians, respectively. There is no dependency on instantaneous phase difference and instantaneous amplitudes of the component particle motions. The expressions for computing the square of semi-major and semi-minor axis lengths were presented by Steen (2000).

$$a^2(t) = \{S_0(t) + [S_1^2(t) + S_2^2(t)]^{1/2}\}/2, \quad (3\text{-}10)$$

and

$$b^2(t) = \{S_0(t) - [S_1^2(t) + S_2^2(t)]^{1/2}\}/2, \quad (3\text{-}11)$$

where S_0, S_1 and S_2 are three of Stoke's parameters and define as follow:

$$S_0(t) = A_v^2(t) + A_h^2(t), \quad (3\text{-}12)$$

$$S_1(t) = A_v^2(t) - A_h^2(t), \quad (3\text{-}13)$$

and

$$S_2(t) = 2A_v(t)A_h(t)\cos[\Phi(t)]. \quad (3\text{-}14)$$

a(t) and *b(t)* are the instantaneous major and minor components of the seismic trace, respectively. The instantaneous reciprocal ellipticity is defined as

$$\rho(t) = b(t)/a(t). \quad (3\text{-}15)$$

The reason for using Reciprocal ellipticity is that ellipticity becomes infinite if the polarisation is linear. In the case of linear polarisation ρ=0 while for the circular polarisation the value is approximately 1. Using signed ellipticity in polarisation studies of monochromatic EM fields was devised by Smith and Ward (1974). Based on their suggestion, Rene et al. (1986) defined an instantaneous signed reciprocal ellipticity as

$$\sigma(t) = \text{sign}\,[\Phi(t)]\rho(t). \qquad (3\text{-}16)$$

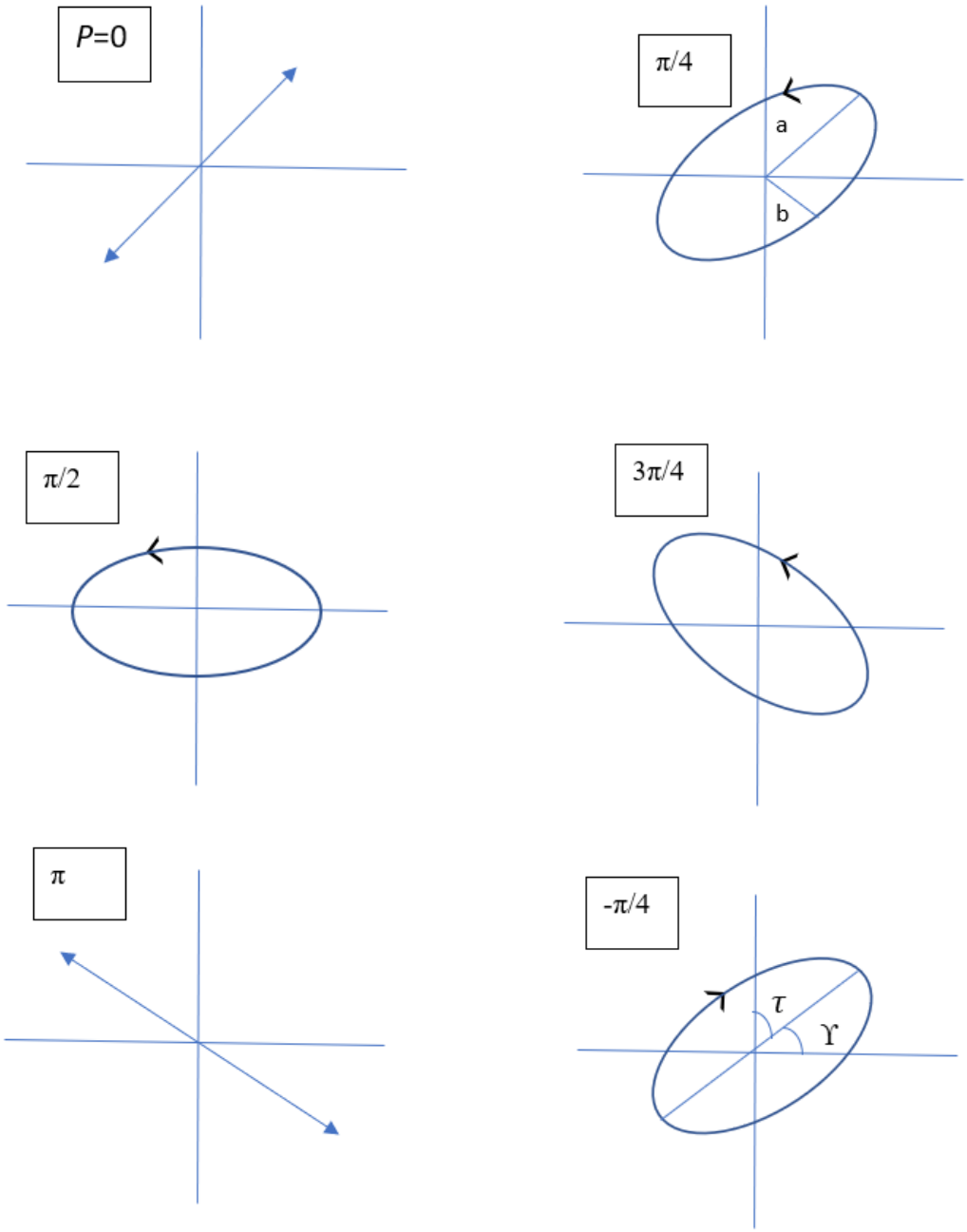

Fig. 3- 1 Polarisation ellipses for harmonic signal with phase differences of 0, π/4, π /2, 3 π /4, π, and - π/4 radians. Positive and negative phase differences correspond to retrograde and prograde motion, respectively. Positive values of the tilt and rise angles (τ and γ) indicate forward tilt of the ellipse. Reciprocal ellipticity is the ratio of the semi-minor and semi-major axis lengths (ρ = b/a).

The negative sign is associated with prograde motion and the positive sign is relevant to retrograde one.

Rene et al. (1986) also defined instantaneous tilt angle which measures tilt of the major axis of polarisation from the vertical as

$$\tau\,(t) = \{\arctan[S_2(t)/S_1(t)]\}/2. \tag{3-17}$$

Instantaneous rise angle $\Upsilon\ (t)$ which measures the angle between the major axis of polarisation and the horizontal is also defined by Rene et al. (1986):

$$\gamma(t) = \begin{cases} \pi/2 - \tau(t); 0 \le \tau(t) \le \pi/2 \\ -\pi/2 - \tau(t); -\pi/2 \le \tau(t) \le 0 \end{cases}. \tag{3-18}$$

Both instantaneous rise angle and tilt angle are in the range of $-\frac{\pi}{2}$ to $\frac{\pi}{2}$ radians. In the above attributes, vertical and radial horizontal components were involved. However, in the case of measuring the deviation of the major axis of polarisation from the horizontal radial direction, radial and tangential horizontal components might be used to compute an attribute which is called instantaneous "skew angle" $\Psi(t)$. One of the advantages of using this attribute is in the interpretation of reflections and diffractions which have propagated out of the vertical plane of the section in CDP reflection methods.

3-4 Polarisation of Rayleigh waves

In the case of an isotropic and homogeneous half-space, Rayleigh waves are non-dispersive and exhibit elliptic retrograde motion in the classical case of propagation along a surface while in the layered medium show multiple modes and also are dispersive. Oliver, J. and Ewing (1957) defined the first mode, M_1, as the primary mode, and higher modes as shear modes. As Kanai (1955) stated even-numbered modes are sometimes called Sezawa, or M_2 type waves. Based on Mooney and Bolt (1966), regardless of mode, particle motion can be either retrograde or prograde, and particular properties of the layered medium can cause the change with frequency. Particle motion of Rayleigh waves can also change due to lateral inhomogeneity. Group velocity can be less than phase velocity at any given frequency provided that *P* and S-wave velocities increase monotonically with depth. According to Mooney and Bolt (1966), the shear modes phase velocities are intermediate between the Rayleigh wave velocity associated with the shallowest layer, and the S-wave velocity of the deepest layer penetrated.

Table 3-1 represents wave classification according to attributes using vertical and radial horizontal components of motion (Rene et al. 1986). The interpreter has an important role in defining the limits ρ_l, ρ_c, τ_v and τ_h defining linear, circular, vertical, and horizontal polarisation, respectively, based on his objective, the SNR sought, and whether instantaneous or average attributes are used.

Table 3- 1 Classification of waves using polarisation attributes. Source: Rene et al. (1986).

Wave type	**Range of attributes**
L=linearly polorised	$0 \leq \rho(t) \leq \rho_1$
***E* = elliptically polarised**	$\rho_1 < \rho(t) < \rho_c$
C = circularly polarised	$\rho_c \leq \rho(t) \leq 1$
***R* = retrograde motion**	$\Psi(t) > 0$
***P* = prograde motion**	$\Psi(t) < 0$
***V* = vertically polarised**	$\lvert\tau(t)\rvert \leq \tau_v$
***F* = forward tilt**	$\tau_v < \tau(t) < \tau_h$
***B* = backward tilt**	$-\tau_h < \tau(t) < -\tau_v$
H = horizontally polarised	$\lvert\tau(t)\rvert \geq \tau_h$

3-5 Time-frequency polarisation analysis

3-5-1 Introduction

Studying the seismic response of Earth to gain geological information often necessitates seismic wave type identification and propagation analysis, which may be done in different domains. Selection of processing method depends on the data sets in terms of the SNR, the measurement geometry and the domain where signal and noise can be better separated. The seismic wavefield is composed of polarized waves in the three-dimensional space; therefore the polarisation filters are one of the processing tools that can discriminate between signal and noise according to their distinct polarisations (Du et al. 2000). Polarisation analysis enhances our knowledge of both source process and the substratum via defining both the type (linear, elliptical or circular) and orientation of polarisation. This analysis requires the calculation of attributes in 3D space which is susceptible to noise. Polarisation methods are capable of simplifying the complexities in high-frequency signals such as conversions of modes and anisotropy. Furthermore, the depth, strike and dip of interfaces can be obtained via determination of the time discrepancy between the

direct and the converted waves using polarisation filtering (Christoffersson et al. 1988; Roberts et al. 1989; Bataille and Chiu 1991).

Polarisation approaches are basically applied in time or frequency domain depending on the wave content and the type of the event. For instance, the time domain methods are more practical in the case of adjacent arrival of waves in time, such as waves conversions at crustal discontinuities. Utilizing correlation technique in time-domain, polarisation filtering designed by Montalbetti and Kanasewich (1970) results in defining the direction of particle motion and rectilinearity measurement of the three-component earthquake data. Even though their non-linear polarisation filter improved the shear and compressional phases, the fact that the waveforms have different polarisations for different frequencies is overlooked. On the other hand, coda waves can be better distinguished in frequency domain. Since the phase and polarisation are not constant in frequency for different wave types, Samson (1977) assessed the polarisation of particle as a function of frequency. Later, Samson and Olson (1980) designed a polarisation filter in frequency domain which improves the waveform while the signal is a pure state of arbitrary shape. Notwithstanding, their proposed filter does not perform well when there is strong random noise.

In real-world seismograms, events with varying frequencies and polarisation characteristics may coincide; vice-versa events with similar frequencies and different polarisation content may transpire in a different time. As a result, methods that consider polarisation variations and features of 3-component signals in the time-frequency domain were proposed. Several authors have attempted to analyze the polarisation of signals in the time-frequency domain by considering the scale of the analyzing window, but the windowing optimization is still intriguing (Jurkevics 1988; Lilly and Park 1995; Morozov 1996; Stockwell et al. 1996; Anant and Dowla 1997; Diallo et al. 2005; Schimmel and Gallart 2005; Claassen 2006; Schimmel et al. 2011). On the other hand, even by selecting the most relevant domain, choosing the appropriate method to estimate the polarisation attributes is still controversial in polarisation analysis. Therefore, some researchers take advantage of the analytic signal to derive the polarisation features (Vidale 1986; Morozov 1996; Schimmel and Gallart 2003; Del Gaudio 2017). The mere hint in most of these methods is applying the Eigen analysis of the data covariance matrix performed in either time or frequency domains. Instantaneous polarisation attributes which deal with linear and elliptical motion without using Eigen analysis are determined in Schimmel and Gallart (2003) which are capable of identifying the polarized signals in separated times. However, the polarized signals with different frequency content concealed in noise cannot be detected efficiently. Therefore, Schimmel and Gallart (2004) devised a frequency-dependent polarisation filter to improve their time-dependent filter by using Eigen analysis. To tackle the mentioned obstacles in time and frequency domains, Pinnegar (2006) defined the elements of the polarisation ellipse in the time-frequency domain by applying the S transform instead of the Short Time

Fourier Transform (STFT) and the Discrete Fourier Transform (DFT) to obtain better results. However, the windowing problem in these Fourier based spectral decomposition methods has always been an important issue for different applications, so several optimized versions of these transforms were introduced in the literature among which the sparsity based approaches were shown to be more successful (Gholami 2013; Sattari et al. 2013; Radad et al. 2015a; Sattari 2016).

Indeed, sparsity is a crucial feature of many signals and systems in real-world applications. Therefore, numerous works and approaches have been proposed to exploit this ubiquitous feature in order to improve the performance or the computational efficiency of conventional approaches which are not capable of exploiting sparsity. The most notable one is the $\ell 1$-norm owing to its simplicity and low computational cost (Loris et al. 2007; Goldstein and Osher 2009; Shalev-Shwartz and Tewari 2009). Another potential strategy to exploit sparsity can be obtained by utilizing the $\ell 0$-norm; however, the $\ell 0$-norm has discontinuity, and its derivative is not available for gradient methods. Hence, various approximations for the $\ell 0$-norm have been introduced to address this problem (Donoho 2006; Lima et al. 2014; Tibshirani 2018). Moreover, by mixing two norms, more potential approaches can be obtained to exploit sparsity and avoid over sparse systems (Gholami 2013; Sattari 2016). Aside from the conventional linear algebraic approaches to create sparsity, researchers often come up with innovative methods to sparsify their results, and the sparsity-based window-parameters optimization introduced to the ST by Sattari (2016) is a novel contribution of this kind which is discussed and used in this paper.

The primary aim of this section is the identification of waves with different polarisation properties more precisely via a robust time-frequency representation. This part is devoted to enhance the resolution of polarisation attributes by applying adaptive sparse S-transform (ST), whose usage becomes fundamental to enhance the quality of observations compared to the STFT and the standard ST with suboptimal resolution due to the Heisenberg uncertainty. The proposed approach differs from other existing techniques, which essentially implement the STFT or the ST to evaluate polarisation in that it uses the SST as a fast and adaptive alternative which helps to calculate the polarisation attributes directly from the sparse TF maps without using Eigen analysis or analytic signal. After that, the obtained high-resolution spectra of elliptical elements were applied in designing time-frequency filters to study the part of the signal with relevant polarisation feature. The ability of the proposed method to accurately recognize the unwanted waves in the TF polarisation map and that of the ST method is presented by comparing the results of the filtered seismic signal in removing surface waves. The results are tested by applying the method on synthetic and real seismograms. We will develop the high-resolution polarisation filtering method by combining the concepts and formulas of TF-based polarisation method, and the sparsity-based adaptive S-transform method.

3-5-2 TF-based polarisation calculation

The polarisation describes the three-dimensional particle ground motion at the receiver position. Based on the source properties and the Earth structure, the particles displacement effected by seismic waves represents individual polarisation shape. The polarisation can be estimated analyzing multicomponent data recorded in three orthogonal directions (generally vertical up, north-south and east-west; the two last ones are convertible to the Radial and Transverse components for computational purposes). Indeed, the main objective of the polarisation analysis is the determination of the polarisation state, characterized type of polarisation (linear, elliptical or circular) and orientation of the polarisation in 3D space. The polarisation analysis is useful as a tool to identify the wave types. For instance, P-wave particle motion is linear and in the direction of the wave propagation, while Rayleigh waves generate elliptical particle motion (Labonne et al. 2016).

Polarisation has an intuitive and straightforward description for a monochromatic wave propagating in 3D space. Assume the three components seismic data, $\left[x(t), y(t), z(t)\right]$, recorded at discrete time samples, $t=n\delta t$, with n ϵ {1, 2,… , N}, δt and N are the sample interval and the number of samples, respectively. Applying the Fourier transform to all three components of the data, we obtain $\left[X(f), Y(f), Z(f)\right]$, whose real and imaginary parts are $X_R(f)$, $X_I(f)$, $Y_R(f)$, $Y_I(f)$, $Z_R(f)$, and $Z_I(f)$, respectively. The Fourier representation of the signal describes a monochromatic signal in a 3D space, whose interpretation has a primary and intuitive role in the description of the polarity. The trajectory of these monochromatic signals for a full period of the wave, T=1/f, delineates polarized elliptical motions in 3D space, comprehensively describing the concept of polarity for different types of the seismic wave (Labonne et al. 2016).

The characterization parameters of the ellipse for each frequency component of the signal can be obtained using the real and imaginary parts of the polarized elliptical motions in 3D space owing to the superposition of x, y, and z components of a monochromatic wave (Pinnegar 2006). The ellipse parameters are schematically depicted in Fig. 3-2 and defined as follows:

- The Semi-major and semi-minor axis of the ellipse are defined as *a* and *b*, respectively.
- The ellipse inclination to the horizontal (x,y) plane is *I*, which presents counterclockwise particle motion when it is less than $\pi/2$ and clockwise when it is more than $\pi/2$.
- Ω is the strike of the ellipse plane.

- φ is the phase measured concerning the time of a point at the maximum displacement.
- ω is the pitch of the semi-major axis, which has positive z coordinates.

For each frequency, f, these elements can be achieved through the estimation of the real and the imaginary parts of the 3-component spectra in terms of polarisation elements and then invert the results. For the sake of brevity, only the results are presented and for more explanation see (Pinnegar 2006).

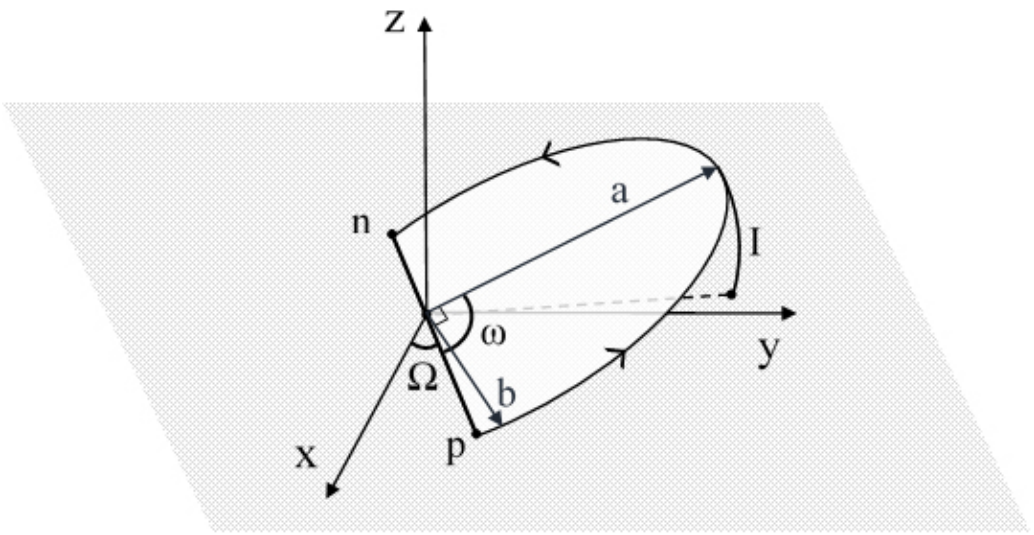

Fig. 3- 2 The ellipse of retrograde motion is plotted together with the polarisation attributes. p *and* n *are the nodes (intersection of the ellipse with the horizontal plane),* a *and b are the ellipse major and minor semi-axes, respectively, the angle* I *is the inclination of the ellipse plane concerning the horizontal plane. The angle* ω *is that between* pn *and* a*, measured on the ellipse plane, whereas* Ω *is that between* pn *and the* x *axis, measured on the horizontal plane.*

$$a = \frac{1}{\sqrt{2}}\sqrt{A+\sqrt{B^2+C^2}} \tag{3-19}$$

$$b = \frac{1}{\sqrt{2}}\sqrt{A-\sqrt{B^2+C^2}}$$

where

$$A = X_R^2 + X_I^2 + Y_R^2 + Y_I^2 + Z_R^2 + Z_I^2$$

$$B = X_R^2 - X_I^2 + Y_R^2 - Y_I^2 + Z_R^2 - Z_I^2$$

$$C = -2(X_R X_I + Y_R Y_I + Z_R Z_I)$$

$$I = \arctan\left\{\frac{[(Z_R Y_I - Z_I Y_R)^2 + (Z_R X_I - Z_I X_R)^2]^{1/2}}{(Y_R X_I - Y_I X_R)}\right\}$$

$$\Omega = \arctan\left\{\frac{(Z_R Y_I - Z_I Y_R)}{(Z_R X_I - Z_I X_R)}\right\}$$

$$\omega = \omega_0 - \pi\left(\frac{sign(\omega_0) - 1}{2}\right)$$

$$\varphi = \varphi_0 + \pi\left(\frac{sign(\omega_0) - 1}{2}\right) sign(\varphi_0)$$

where

$$\omega_0 = \arctan\left\{\frac{b[Z_R \cos(\varphi_0) - Z_I \sin(\varphi_0)]}{-a[Z_R \sin(\varphi_0) - Z_I \cos(\varphi_0)]}\right\}$$

$$\varphi_0 = \frac{1}{2}\arctan\left(\frac{C}{B}\right)$$

Finally, the sparse ST is used to have time-frequency representation of the elements defined in Eq. (3-19). In the case of substituting the real and imaginary parts of the time-frequency spectra of the signal in Eq. (3-19), the elements of the polarisation ellipse can be obtained in the time-frequency domain.

3-5-3 Results

3-5-3-1 Polarisation analysis of Synthetic data

The Green function for a strike slip earthquake with the epicenter distance of 500 km is generated by synthetic seismogram codes (Herrmann 2013) to evaluate the efficiency of the proposed method in diagnosing the wave polarisation. The model used is a model for North America craton with the sampling interval of 0.25. As can be seen in Fig. 3-3, the time-frequency spectrum of the 3-component achieved via sparse ST have higher resolution and are sparser than the ST.

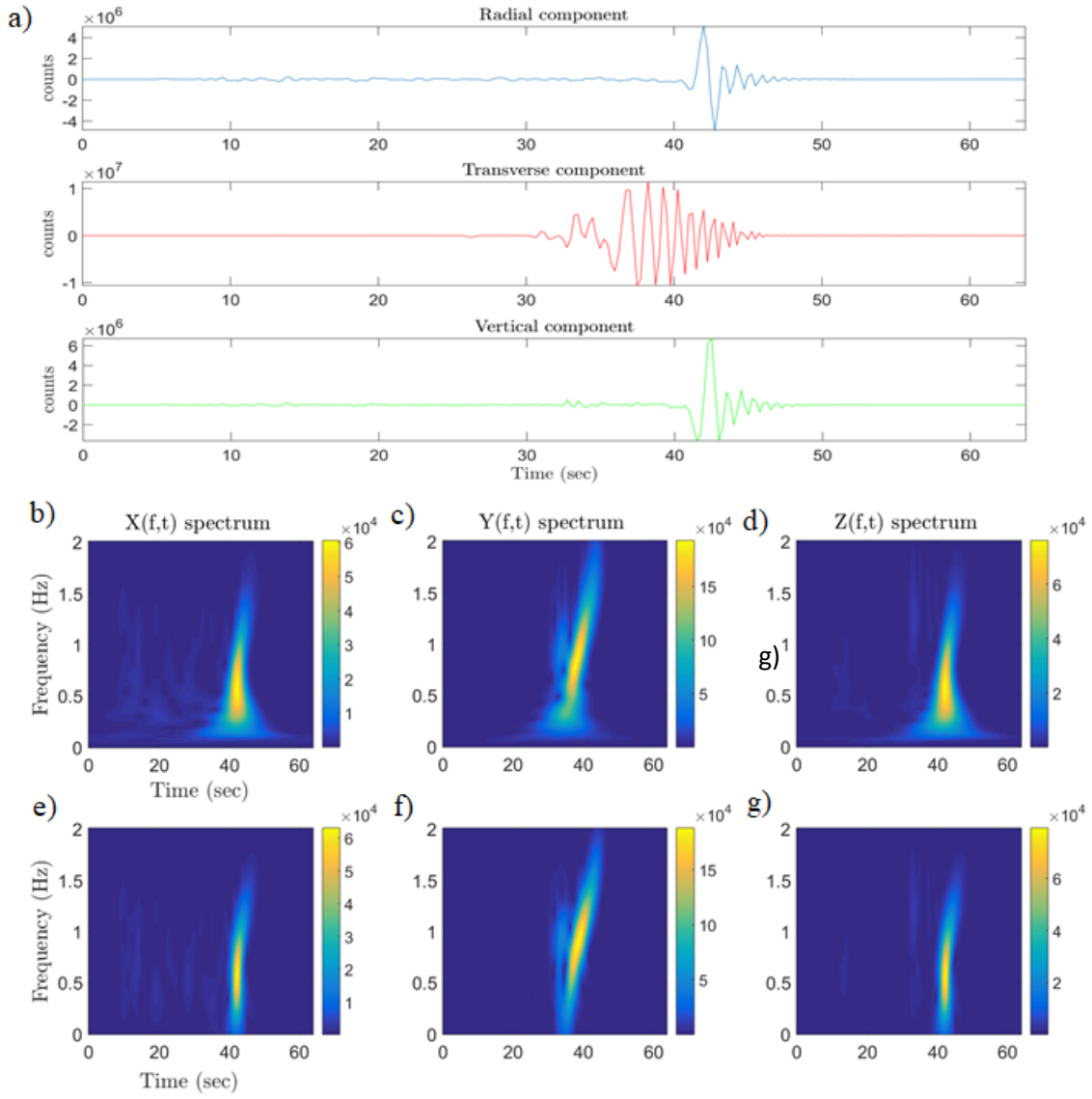

Fig. 3- 3 a) The three-component synthetic seismogram with their corresponding spectrum obtained via (b-c) ST and (d-g) sparse ST.

It is worthwhile to note that the Rayleigh wave can be detected on the radial component, whereas Love wave has more contribution to the transversal component. Furthermore, the velocity of the Love wave is higher than the velocity of Rayleigh wave, which leads to its sooner arrival. Therefore, the arrival of the Rayleigh wave is better highlighted in Fig. 3-3 (b and e), while the Love wave is more visible on the y-component (c and f in Fig. 3-3) by its large amplitude, which arrives sooner than Rayleigh wave packets. As can be seen in Fig. 3-3, the superiority of the proposed method in representing the TF map of the signals is obvious in term of the resolution, especially in low frequency parts, where the proposed method localized the signal more accurately both in time and frequency.

The S and Sparse S spectrum of semi-major and semi-minor axes, their difference, $a[\hat{\tau}, \hat{f}]-b[\hat{\tau}, \hat{f}]$ and the total power, $\sqrt{a[\hat{\tau}, \hat{f}]^2+b[\hat{\tau}, \hat{f}]^2}$ are shown in Fig. 3-4. As can be seen in semi-major plot, the first high amplitude event indicates the Love wave, and the second one pinpoints the Rayleigh wave. Two motions can identify the polarisation ellipse; the pure linear which can be determined by the amplitude spectrum of $a[\hat{\tau}, \hat{f}]-b[\hat{\tau}, \hat{f}]$ and the pure circular which is the effect of semi-minor axis amplitude. In the figure of the semi-minor axis, the low amplitude belongs to the Love wave, while the high amplitude spectrum depicts the presence of the Rayleigh wave. On the other hand, the low amplitude of the Rayleigh wave in the figure of $a[\hat{\tau}, \hat{f}]-b[\hat{\tau}, \hat{f}]$ is expectable since this figure pinpoints the pure linear motion (Fig. 3-4). The total power spectrum has an estimation of the energy density of all three components.

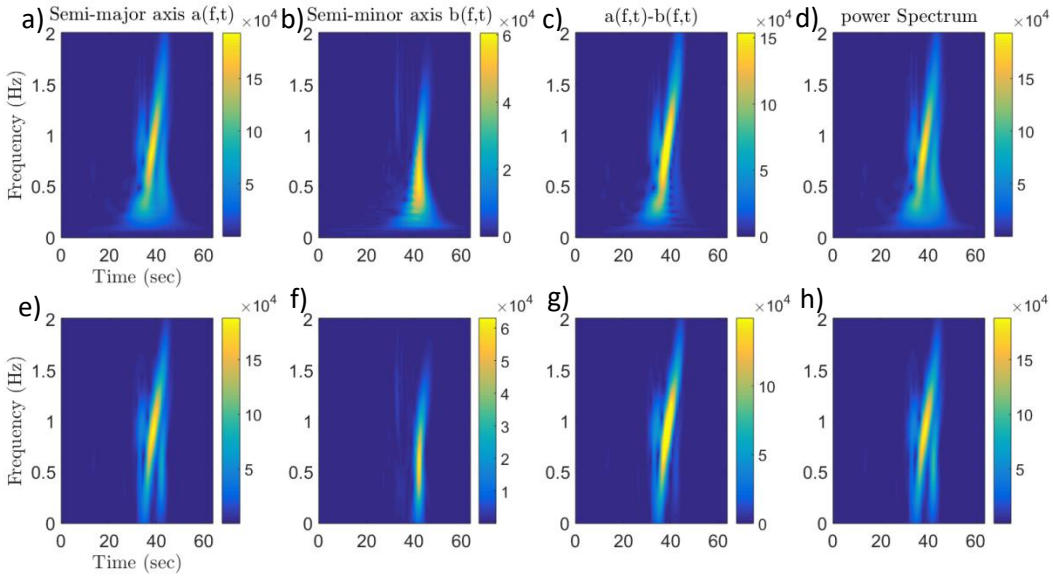

Fig. 3- 4 The spectrums of semi-major, semi minor, the difference of the ellipse axes, and the total power spectrum of the synthetic seismograms in Fig. 3-3 by S transform (a-d), and Sparse ST (e-h).

Considering the semi-major map, the proposed method defined the arrival of the Love and Rayleigh waves more distinctely than the one presented by ST method. The first high amplitude represents the Love wave (Figs. 3-4a and 3-4e), which is completely separated from the Rayleigh wave in Fig. 3-4e. The difference in resolution can also be seen in Figs. 3b and 3f, where the sparse ST estimated the arrival of the Rayleigh wave with less error in frequency range of 0 to 0.5 Hz. The efficiency of the proposed method in rendering more clear and accurate TF maps is obvious in obtaining the pure linear motion and energy density of the components (Fig. 3-4g and 3-4h, respectively).

3-5-3-2 Real data example

A recorded earthquake at the PEMO station with the azimuth 48.3^{O} north of west, Canada (45.68^{O} N, 77.25^{O} W) with the magnitude of 6.9, and epicentral distance of 7124 Km is chosen as an example to compare the efficiency of the sparse ST to conventional ST. The earthquake location is at the latitude 51.58^{O} N, longitude 176.67 ^{O} E in the Aleutian Islands occurred on 2003 June at the depth of 18 Km.

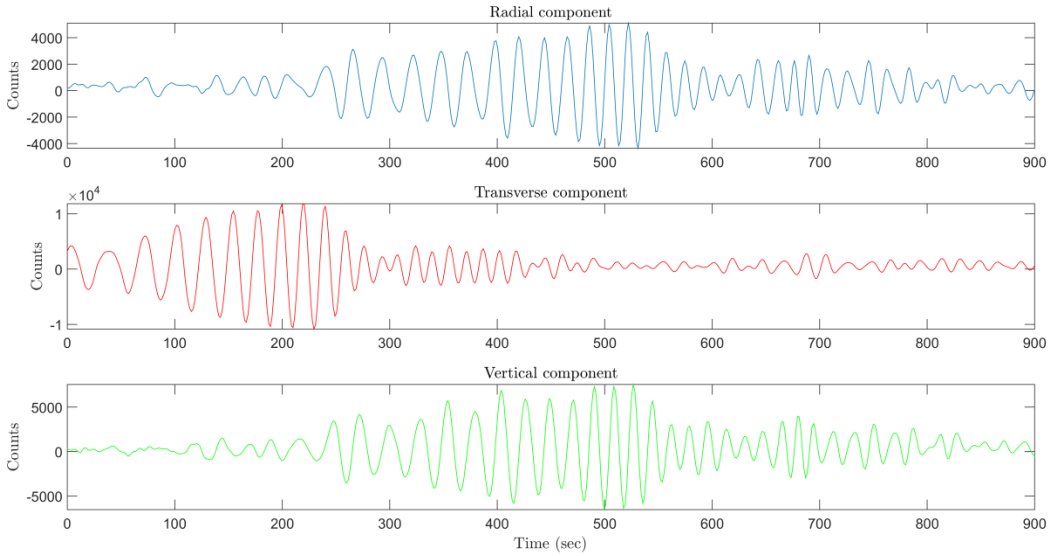

Fig. 3- 5 The radial, transverse, and vertical components of the excerpted displacement record for the earthquake registered at PEMO station.

The principal purpose of giving this example is its high rate of the signal to noise ratio. The part of this registration, which has the arrival of surface waves with distinct polarisation characteristics is excerpted for polarisation analysis. The original record is processed by removing mean, trend, conversion of the velocity to displacement, and decimation of the sampling interval from 0.01 s to 1.5 s accompanied by a Butterworth anti-aliasing filter. The radial and transverse components of the record are rotated 48.3^{O} counter-clockwise to align the x and y components, respectively, into the direction of wave propagation (Fig. 3-5).

Fig. 3-6 compares the S transform and sparse ST spectra for the 3-component seismogram in Fig. 3-5. It can be noted in Fig. 3-6 that the sparse ST distinguishes the energy density with higher resolution in time and frequency which can be a significant aid in our analysis procedure.

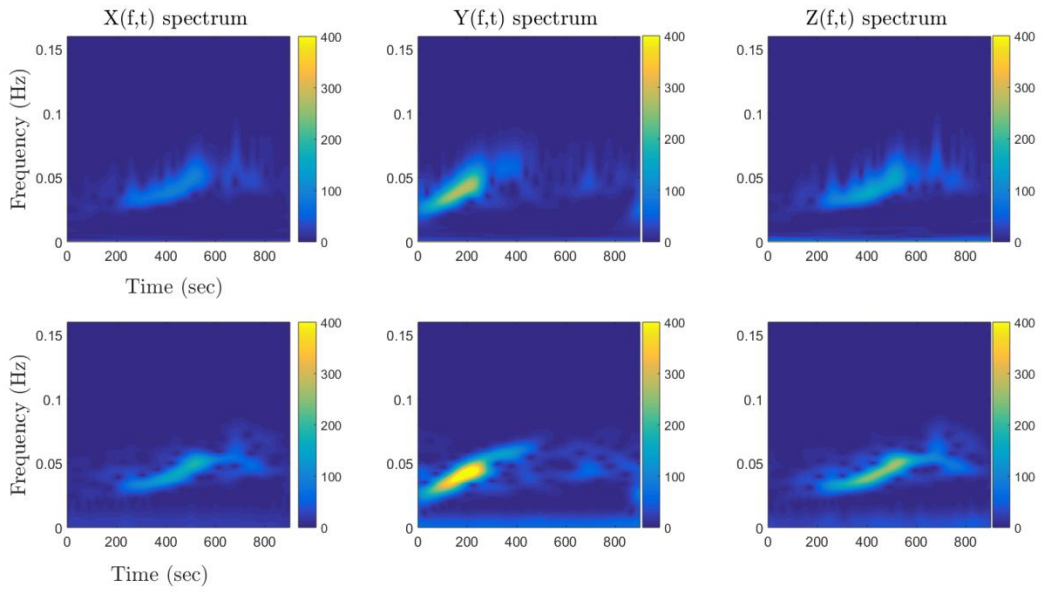

Fig. 3- 6 The amplitude spectrum of the X, Y, and Z components achieved by ST (top plots) and Sparse ST (bottom plots).

The x-component depicts the presence of the Rayleigh wave, while y-component shows the Love wave arrival more distinctly (Fig. 3-6). The dispersion feature of the Rayleigh and Love waves caused the arrival of the high-frequencies to penetrate shallow depth with a slight time delay. The higher resolution and sparser amplitude spectrum of the components benefited us to have more accurate polarisation attributes, which are estimated via S and Sparse S spectrum (Fig. 3-7).

The first high amplitude in semi-major plot shows the Love wave, and the second one with lower amplitude defines the Rayleigh wave. A comparison of the semi-major with semi-minor plots reveals the higher amplitude of the Rayleigh in semi-major about one and half of semi-minor axis. As can be seen in Fig. 3-7, the sparse ST defined higher amplitude for the Rayleigh and Love waves and sparser TF map of the polarisation attributes. The S and sparse S spectrum of the other elements of the ellipse are depicted in Fig. 3-8. The intricacy of the visual interpretation of these features provides the selection of the parts that have high amplitudes in the total power spectrum.

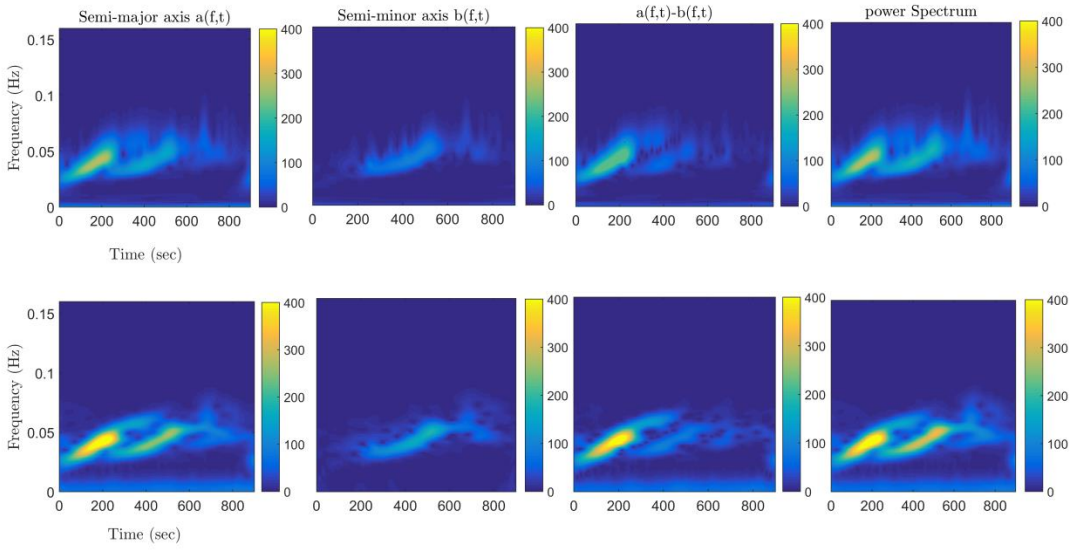

Fig. 3- 7 The spectra of semi-major, semi minor, the difference of the ellipse axes, and the total power spectrum of the seismogram in Fig. 3-5 by S transform (upper plots), and Sparse ST (lower plots).

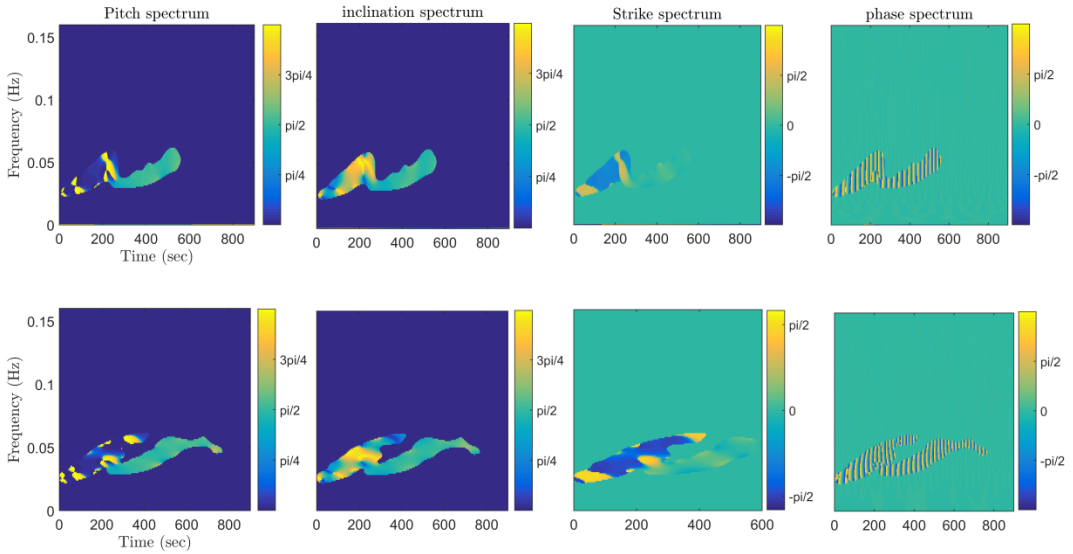

Fig. 3- 8 The spectrums of the argument of maximum $\omega\left[\hat{\tau}, \hat{f}\right]$*, inclination* $I\left[\hat{\tau}, \hat{f}\right]$*, strike* $\Omega\left[\hat{\tau}, \hat{f}\right]$*, and the phase* $\varphi\left[\hat{\tau}, \hat{f}\right]$ *of the seismogram in Fig. 3-5 by S transform (upper plots), and sparse ST (lower plots).*

Each of these attributes can be applied to define the polarisation ellipse; for instance, the inclination gives the dip of the ellipse plane relative to the horizontal and $\Omega\left[\hat{\tau}, \hat{f}\right]$ gives the strike of the ellipse plane.

Based on the characterization of the polarisation attributes defined in Fig. 3-8, it can be concluded that the first highlighted part, excerpted from the segments with high energy density in the total power spectrum, has the features of the Love wave, while the second one characterizes the presence of the Rayleigh wave. The importance of the sparser and more accurate TF maps of the polarisation attributes is more significant where the high energy density of the power spectrum needs to be highlighted. In the inclination spectrum, the Rayleigh wave is detected through a stable value of $\pi/2$, while this value is not stable for the Love wave in this spectrum and varies between 0 and π, provided that noise contributions can make variations in an almost linear motion.

As can be seen in Fig. 3-8, the linearity of the motion in the Love wave makes the strike of the ellipse plane, Ω, unstable which alternates between $-\pi/2$ and $\pi/2$ in this example. The reason for this variation is that the strike is perpendicular to the direction of wave propagation for the Love wave. However, the particle motion of the Rayleigh wave in the direction of wave propagation results in nearly zero value for the strike. The strike of the Rayleigh wave in this example asserts retrograde particle motion which means zero particle displacement towards positive radial direction when it soars via the horizontal plane.

The last attribute that can be used to distinguish the Rayleigh and Love waves is the pitch of the ellipse major axis. Considering the love wave has linear and horizontal motion, ω must be almost zero or π, while this value reaches $\pi/2$ for the Rayleigh wave because the semi-major of the motion ellipse is vertical (Fig. 3-8). The drawback of this method is defining I, ω, and Ω in the pure linear motion state since their values are 0 in Eq. (3-19) according to the fact that in the purely linear motion we have $\frac{X_I}{X_R} = \frac{Y_I}{Y_R} = \frac{Z_I}{Z_R}$. Notwithstanding, the presence of noise contamination in real seismograms makes this assumption impracticable.

3-5-4 Polarisation filtering

Our invertible sparse ST TFR aids to design adaptive polarisation filters to target the events with distinctive polarisation features. Multiple time-frequency filters can be devised by implementing the elements of the ellipse. However, the filter designed by Pinnegar (2006) was used in this paper to remove Rayleigh wave packets by applying the conditions $I \approx \frac{\pi}{2}, b \geq \frac{a}{2}$ and $\omega \approx 0$ in time and frequency domain as:

$$F_1(I)=\begin{cases}0, \left|I-\dfrac{\pi}{2}\right|<\dfrac{\pi}{10}\\ 1, \left|I-\dfrac{\pi}{2}\right|>\dfrac{\pi}{5}\\ \dfrac{1-\cos\left(10\left|I-\dfrac{\pi}{2}\right|-\pi\right)}{2}, \dfrac{\pi}{10}\le\left|I-\dfrac{\pi}{2}\right|\le\dfrac{\pi}{5}\end{cases} \tag{3-20}$$

$$F_2\left(\frac{b}{a}\right)=\begin{cases}0, b>0.6a\\ 1, b<0.5a\\ \dfrac{1+\cos\left[10\pi(b/a-0.5)\right]}{2}, 0.5a\le b\le 0.6a\end{cases}$$

$$F_3(\Omega)=\begin{cases}0, |\Omega|<\dfrac{\pi}{6}\\ 1, |\Omega|>\dfrac{\pi}{3}\\ \dfrac{1-\cos(6|\Omega|-\pi)}{2}, \dfrac{\pi}{6}\le|\Omega|\le\dfrac{\pi}{3}\end{cases}$$

The total filter is designed by the contribution of all the three filters in Eq. (3-20) as follows,

$$F[\hat{\tau},\hat{f}]=1-\left\{1-F_1(\mathrm{I}[\hat{\tau},\hat{f}])\right\}\left\{1-F_2\left(\frac{b[\hat{\tau},\hat{f}]}{a[\hat{\tau},\hat{f}]}\right)\right\}\left\{1-F_3(\Omega[\hat{\tau},\hat{f}])\right\} \tag{3-21}$$

The devised filter is versatile, and therefore various filters can be designed. We can diminish the amplitude of an aimed ellipse, set the ellipse strike to the orientation of wave propagation or feasibly target discrete time or frequency. However, our filter is based on the dip angle, ellipticity, and strike direction to detect Rayleigh waves. The total filter detailed in Fig. 3-9 removes all the parts that each filter in Eq. (3-20) rejected from the trace.

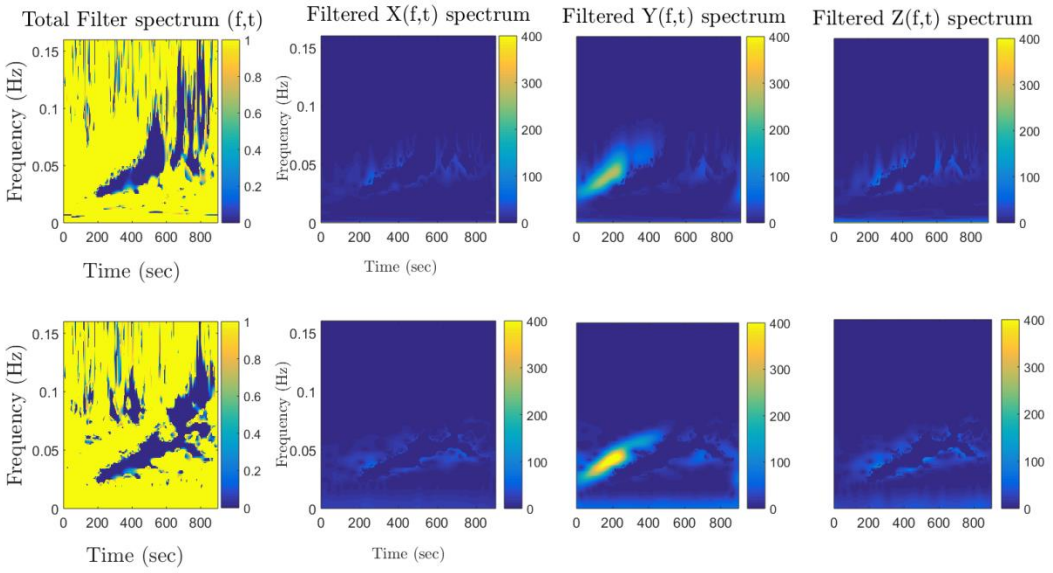

Fig. 3- 9 The total filter of Eq. (3-21) and the corresponding filtered spectrum of the 3-component signal of Fig. 3-5 achieved by S transform (top plots) and sparse S transform (bottom plots).

A major criticism of using ST is not obliterating all the targeted parts and is not sufficiently sparse. The given examples highlighted that our polarisation filter is more efficient in satisfying the demands. It is apparent from Fig. 3-9 that the sparse ST has removed the Rayleigh waves much more precisely than the ST, and more packets of Rayleigh waves are detected in this filter. Afterwards, the trace can be filtered by multiplying the time-frequency spectrum of each component to the total filter and then reconstruct the filtered signal by applying an inversion. The filtered spectra of the 3-component earthquake trace of Fig. 3-5 are shown in Fig. 3-9. The most striking result to emerge from the figure of filtered data via sparse ST is the consecutive presence of Rayleigh wave packets and sparsity of our proposed filter. The filtered sparse ST spectra in Fig. 3-9 represents the complete removal of Rayleigh wave from the spectrum of the 3-component data selected in Fig. 3-5.

3-5-5 Conclusions

This study has enhanced the perceiving of waves contribution in seismic signals through polarisation analysis. A cutting-edge solution was presented in this work for improving the resolution of the polarisation attributes spectra. This contribution provided a viable alternative to the ST in polarisation analysis and obtained comprehensive results proving the superior performance of the sparse ST. The ability of both time and frequency regularization and high resolution of the proposed spectral decomposition

approach was used to delineate the arrival of different phases more distinctly. Exploiting the sparsity, adaptivity, frequency dependency of this time-frequency decomposition, and its superiority over other TF in terms of robustness to noise, temporal and spectral interference resolution and the advantage of having only one free parameter to set, the polarisation attributes were obtained more effectively. The proposed procedure was a clear advance on current polarisation methods by improving the resolution of the attributes and reducing the computational complexity. Impressive results take advantage of the high-resolution polarisation attributes to predict the packets of Rayleigh wave to design a robust adaptive filter for their removal. The synthetic and real earthquakes with distinct Rayleigh and love polarisation were selected as examples to be analyzed via ST and sparse ST. The linear motion of the ellipse was obtained by the difference of the major and minor axes, while its circular motion was defined by the minor axis. Moreover, the ambiguity of the direction of particle motion was also relieved via the strike attribute. The polarisation attributes were obtained more accurately by regularization of the abrupt frequency changes. The comparisons of the results obtained by the ST and the sparse ST confirmed the superiority of the sparse technique in Rayleigh wave detection. The principal feature of this adaptive sparse approach is to restrain random noise pervasive in both time and frequency domains. This approach would lend itself well for use by seismologist in waveform tomography, characterization of surface waves, the splitting of shear waves and for seismic exploration such as oil & gas.

Chapter 4

Ambient noise

4-1 Ambient noise

The surface of the earth is constantly moving and altering which is the range of seismic frequencies to large earthquakes. Noise is a general word that is stated to minor earth vibration and has a small amplitude. It is worth to mention that these vibrations are sometimes called ambient noise or microtremor. In geophysics, noise refers to the signal that interferes with the desired acquisition; such as tide in the sea seismic, metal objects in electromagnetic and dense objects in a gravimetric acquisition. Whatever assumed noise in acquisitions is not absolute and can be changed into a valuable signal by varying the conditions.

Microtremors are vibration and ground displacement within the range of 0.1-1 micron and the velocity of particles of the waves is around 0.01-0.001 cm/s that can only be recorded by strong amplification seismometers. In recent years, numerous articles and researches have been done about microtremor and the significant point in these researches is the variation of microtremors in time and space. Nowadays it is known that microtremors are variable in time and space and their vibration is complex, irregular, and not repeatable. When microtremors appear simultaneously at different stations, it defines that they are not completely random and some of them are coherent waves that are in records. Microtremors are a collection of waves that are propagating in different directions. In the following part, the origin of microtremors will be discussed.

4-2 The origin of microtremors

As the number of processing techniques increases, based on the assumption that the noise wavefield is predominantly consisting of fundamental mode Rayleigh waves, knowing the origin of the ambient seismic noise wavefield becomes more important since the use of seismic noise in seismic hazard purposes is growing. Microtremors come from different sources that are divided into two groups: cultural sources that are human activities such as traffic, passing cars and trains, the activity of factories and natural sources

such as sea and ocean wave strikes, tide, rain, wind, atmospheric pressure discrepancy, and human footsteps, etc. Different types of sources are organized according to their frequency by Gutenberg (1958). The same conclusions in a noise review were achieved by Asten (1978) and Asten and Henstridge (1984) (Table 4-1).

Table 4- 1 summary of ambient noise sources according to frequency. Source: Gutenberg (1958) and Asten (1978, 1984)

	Gutenberg (1958)	**Asten (1978, 1984)**
Oceanic waves striking along the coasts	0.05-0.1Hz	0.5-1.2Hz
Monsoon/large scale meteorological perturbations	0.1-0.25Hz	0.16-0.5Hz
Cyclones over the oceans	0.3-1Hz	0.5-3Hz
Local scale meteorological conditions	1.4-5Hz	-
Volcanic tremor	2-10Hz	-
Urban	1-100Hz	1.4-30Hz

Based on this difference, these authors distinguish between microseisms as low and microtremors as high frequency events, corresponding respectively to natural and cultural sources. Considering the summaries of Gutenberg (1958) and Asten (1978), natural sources (ocean, large-scale meteorological conditions) are at low frequency (below 1 Hz); either natural (local meteorological conditions) or cultural (urban) sources are at an intermediate frequency (1 to 5 Hz); at higher frequencies, the sources are essentially cultural. A change of behavior in noise around 1 Hz, which can be a frontier between microseism and microtremor was indicated by the investigation of Frantti (1963). In the years after, Seo (1998) devised a more comprehensive classification for microtremor origin and classified them based on their periods into long and short. Short period microtremors are related to near-surface structures till 10 meters in-depth and the microtremors with the period more than 1 second (long period) can be relevant to the structures of several meters to bedrock with the shear velocity of about 3 km/s. This classification is presented in table 4-2.

Table 4- 2 Ambient noise classification. Source Seo (1998)

Group	**Period**	**Origin**
Long period microtremor	T>1s	Natural
Short period microtremor	T<1s	Human activity

Another classification is presented by Schimmel et al. (2011) who divided the ambient noise into hum and microseism which are the weakest and strongest ambient noise, respectively. The content of the hum, according to Suda et al. (1998), Tanimoto (2007), Roult and Crawford (2000), and Rhie and Romanowicz (2006) is free oscillations of the Earth, which are continuously excited in the range of 5-20 mHz. On the other hand, microseisms mainly consist of Rayleigh waves in the range of 0.04- 1 Hz.

Microseisms are separated into two forms: primary (PM) and secondary (SM) components, which are different in the sense of frequency and the way of generation. As Hasselmann (1963) mentioned, the primary microseisms is produced by the interaction of ocean waves with the sloping seafloor, while the secondary ones are generated by the interference of waves with nearly opposite wave numbers. Regarding the frequency, primary ones have the ocean gravity waves frequency and are strongest between 0.05 and 0.08 Hz, while the secondary ones are strongest between 0.1 to 0.16 Hz and are the dominant signal (Hasselmann, 1963; Tanimoto et al., 2006; Tanimoto, 2007; Kedar et al., 2008; Ardhuin et al., 2011). The fundamental mode of Rayleigh waves are the main modes in the SM between 0.1-0.16 Hz and above this frequency range, as Haubrich, R.A. and McCamy (1969) stated, according to the analysis of wave number-frequency spectra, higher modes are dominant.

Aster et al. (2008) presented a seasonal variability of the SM and show that the microseism power series correlate with continental-scale station distribution. Moreover, from time-frequency spectra which has been applied by Stutzmann et al. (2009), the latitudinal dependence of seismic noise is also observed. They also achieved the result that microseisms generated several thousands of km away could be recorded by continental stations. The seasonal variation is investigated by Tanimoto et al. (2006) by analyzing the variations of horizontal to vertical amplitude ratios (H/V) for Rayleigh waves and found that these changes of H/V ratios are related to seasonal variation of the source areas that effectively alter the relative excitation of higher modes to the fundamental mode of Rayleigh waves. However, from stabling of back azimuths, it can be inferred that the sources move to different water depths.

4-3 Application of the microtremors

The growth of many cities over the last decades causes the need for a careful and reliable assessment of site amplification phenomena. Resonance frequencies and amplification factor techniques were developed to identify the main characteristics of site responses for soft deposits. These techniques may be grouped into three main categories. The first is based on a numerical simulation approach (see

Panza et al. 2001 for a review of numerical simulation methods), and is coupled with classical geophysical and geotechnical tools. The second category of the technique includes directly measuring the site response based on earthquake recordings on specific stations located on carefully chosen sites. Its use in areas of low to moderate seismicity is limited by the time required to gather a significant number of recordings with a satisfactory signal to noise ratio. The last category is dedicated to ambient noise recording which has become more popular over the last decades since it is a low cost and convenient method to be used especially in urbanized areas.

To determine site response parameters, the simple horizontal to vertical Fourier amplitude spectral ratio (HVSR), and the more advanced array technique are the common methods that are used widely. The ability of the HVSR technique to provide reliable information related to site response has been repeatedly shown in the past (Nakamura 1989; Lachet and Bard 1994; Bard 1998). However, its theoretical basis is still ambiguous as two opposite explanations have been proposed. Nakamura (1989, 2000) removed the effects of surface waves and states that the horizontal to vertical spectral ratio mainly reflects the S-wave resonance in the soft surface layer, in this case, HVSR curves provide a consistent estimate of the site amplification function. Lachet and Bard (1994) and Bard (1998) contradicted this assumption in their papers, and highlighted the relationship between the HVSR and the ellipticity of fundamental mode Rayleigh waves. Assuming their theory, the peak of HVSR would be due to the elimination of Rayleigh waves vertical component in comparison to Nakamura theory that relates the peak to the amplification of S-wave on horizontal components. Regarding that the seismic noise wavefield is mainly constituted by surface waves, then new challenges arise such as the identification of the type of surface wave (Rayleigh or Love waves) and propagation mode (fundamental or higher modes). Since the interpretation of array microtremor recordings mainly focuses on the derivation of surface waves dispersion curve, knowing the response of the above challenges is very essential for the processing. For instance, in the processing of horizontal components, the simultaneous existence of both Rayleigh and Love waves needs to be considered (Bonnefoy-Claudet et al. 2004). The inversion of S-wave velocity profile might seriously bias if wrong identification of surface waves type (Rayleigh or Love) or order (fundamental or harmonics) is chosen (Kuwayama 1992; Beaty et al. 2002; Zhang and Chan 2003).

4-4 Composition of the seismic noise wavefield

Separation of the noise wavefield into body waves (P, SV, SH) and surface waves (Rayleigh and Love waves), and quantifying the contribution of each type of waves would be the desired purpose which

is a cumbersome task. Comparison of the depth dependence of the noise Fourier spectral amplitude with theoretical values for Rayleigh and P waves was carried out by Douze (1967) with several noise measurements in a deep borehole. In one of these measurements, the Apache borehole (2917 m deep, Oklahoma), the significant decrease of the depth-to-surface noise Fourier spectral ratio at periods shorter than 2–3 s, suggests that the noise energy is mainly carried by surface waves. Since there is no decrease in Fourier spectra amplitude with depth beyond 3 s, which gets close to 1, these waves are mainly body waves. The nature of the seismic noise on sedimentary sites was discussed by Horike (1985) and Li et al. (1984) using array analysis. A comparison of phase velocities derived from array observations with f–k processing with the theoretical expected wave velocities corresponding to the soil structure was conducted. A mixture between higher Rayleigh modes and P waves was concluded by Li et al. (1984) at Lajitas (southwest Texas), in microtremors in the 1–20 Hz frequency range. An investigation was done by Horike (1985) using an f–k processing in lower frequency ranges on an eleven-station array for the noise within the Osaka basin (Japan). It is found in this analysis, that higher mode could be detected in addition to the fundamental Rayleigh mode for frequencies between 0.9 and 3 Hz in the case that noise consists of fundamental Rayleigh waves between 0.5 and 0.9 Hz.

Bonnefoy-Claudet et al. (2006) used array analysis to investigate the composition of synthetic noise wavefield computed at the surface of a simple horizontally layered medium consisting of one soft layer over a half-space. In their investigation, a link between the relative proportion of Rayleigh waves to body waves and the spatial noise source distribution (in terms of source–receiver distance and source depth) was found. Only non-dispersive body waves are present in the noise wavefield if the sources are below the sedimentary layer (i.e., inside the bedrock). Such a situation may be representative only for microseism with a distant origin since cultural noise sources are located on the surface. In the case of surface sources, their distance from the receiver plays an important role: in the case of far distance (i.e., more than twenty times the sedimentary layer thickness), the vertical noise wavefield consists of a mixture of Rayleigh and body waves (head waves propagating along the sedimentary/bedrock interface); if the sources are close, the vertical noise wavefield mainly constitutes of fundamental mode Rayleigh waves. A comparison between observed HVSR curves and theoretical ellipticity curves of the fundamental mode of Rayleigh waves for sedimentary sites was shown by Yamanaka et al. (1994) using continuous noise measurements in the northwest part of Kanto plain (Japan). HVSR curves have been observed for a different time during day and night. The good fit between the two curves leaded Yamanaka et al. (1994) to suggest that microseisms over the frequency range 0.1 to 1 Hz mainly consist of the fundamental mode of Rayleigh waves.

The comparison between the HVSR curve and the ellipticity curve of the fundamental mode of Rayleigh waves was also done by Bonnefoy-Claudet (2004) but synthetics noise, synthetics computed at

the surface of various horizontally layered media excited by random surface sources. This kind of simulation is thus valid only for cultural noise resulting from local surface sources, and cannot yet be extended to low-frequency microseisms caused by distant oceanic sources. Analysis of the HVSR curve shows that the noise wavefield is dominated by surface waves, only in the case that the velocity contrast between the surface and the underlying bedrock is above 3–4 which represent a large impedance contrast, while for smaller velocity contrast (below 3), the wave field also includes body waves generated by close surface sources (Bonnefoy-Claudet 2004). Microseisms consist mainly of the fundamental mode of Rayleigh waves (Horike 1985; Yamanaka et al. 1994) at frequencies below 1, as far as only the surficial structure is concerned (top kilometers to 100 m). About the higher frequencies, there are controversial ideas about the nature of seismic noise between the authors.

4-5 Contribution of Rayleigh waves in the noise wavefield

Access to 3-component seismograms was the key point in the investigation of Rayleigh and Love waves. Ohmachi, T. (1998) simulated noise propagation in simple 1D models. The results show a strong variation in the Rayleigh to Love waves ratio in the synthetic noise, as it depends on the type of excitation (vertical, transverse, or radial forces), on the observation direction, and the impedance soil contrast. This ratio varies between 10% and 90% with an average of around 30%, and it seems difficult to establish reliable conclusions concerning the proportion of Rayleigh waves in actual noise. Therefore, they decided to work on array measurements such as SPAC. Yamamoto (2000) used the SPAC technique to approximate the energy ratio between Rayleigh and Love waves for three sites in the city of Morioka, Japan. It is presented that Love waves carried 60% to 85% of the noise energy in the 3–8 Hz frequency range. An f–k analysis on radial and transverse motion and a three-dimensional SPAC approach were used by Arai and Tokimatsu (1998), while both methods yielded entirely similar results. The energy ratio of the Rayleigh to Love waves differs around an average value of 0.7.

Although different quantitative Rayleigh to Love waves ratios is prevailed by Arai and Tokimatsu (1998) and Yamamoto (2000), they all concluded on highlighting the supremacy of Love waves in the noise wave field. However, below 1 Hz, at lower frequencies, agreement between different authors seems difficult. The relative contribution of Rayleigh to Love waves in the seismic noise wavefield might be affected by the site geology and geometry (sediment thickness, slope, the geometry of the sediment-to-bedrock interface) as well as the source properties (see Ohmachi, T., Umezono (1998)).

Table 4- 3 Summary of Rayleigh to Love waves ratios contained in seismic noise wave field

	Frequency range	**Rayleigh waves proportion**	**Love waves proportion**	**Sites**
Chouet et al. (1998)	>2 Hz	23%	77%	volcanoes
Yamamoto (2000)	3-8 Hz	<50%	>50%	Sedimentary (thickness<100m)
Arai, H., Tokimatsu (2000)	1-12Hz	40%	60%	Sedimentary (thickness<100m)
Cornou (2002)	0.1-1Hz	50%	50%	Sedimentary (thickness~500m)
Okada (2003)	0.4-1Hz	<50%	>=50%	Sedimentary (thickness~50m)

4-6 Relative contribution of the fundamental mode of Rayleigh waves

It is almost unfeasible to predict the actual energy distribution for various modes of Rayleigh waves due to the heterogeneous ground conditions. HVSR analysis can give indirect information described by Stephenson (2003) who investigated the link between HVSR and ellipticity of particle motions of Rayleigh waves, and concluded that in the case of having only the fundamental mode of Rayleigh waves then the HVSR curves should have a peak/trough structure. Konno and Ohmachi (1998), who show peak/trough structure on actual HVSR curves have also confirmed this statement. A consistent second peak on HVSR curves was also determined by Bodin et al. (2001) in the Memphis basin. This peak was defined as the first higher harmonic of Rayleigh waves. Nevertheless, in the Bonnefoy-Claudet (2004) simulation, higher peaks in the case of distant predominant noise sources are defined as body waves resonance. A synthetic source was used by Tokimatsu (1997) to show the effectiveness of higher modes in creating velocity inversion when a superficial layer overlies a softer layer.

4-7 Horizontal to vertical spectral ratio

The Horizontal-to-Vertical Spectral Ratio (HVSR or H/V) technique is a low cost and fast way to study the shallow-subsoil seismic properties (which are of engineering interest). The single-station

measurements carried out on the Earth surface makes this technique more popular for near surface engineering. The most significant application of this method is to analyse seismic-amplification effects in terms of S-wave resonance frequency and constraining the elastic properties of the shallow geological structure method in seismic exploration. However, there are controversial ideas for the results obtained from this technique which has direct effect on the inversion process and consequently on imaging the subsoil profile. To apply this technique, 3-component ground motion velocity spectra, displacement or acceleration measurements has to be taken into account and horizontal to vertical Fourier spectrum ratio, H/V (or HVSR) curve, which is a function of the frequency should be averaged on adequate samples.

4-7-1 H/V technique review

In order to infer seismic subsoil properties, Kanai (1961) used the ambient-vibration horizontal-motion spectra, although they were aware of the dependence of ambient vibration features on both ambient-vibration sources characteristics and site mechanical-properties. However, it is believed that the sources characteristics are usually more reflected by ambient-vibration spectra rather than the subsoil ones (cf. Tokimatsu (1997). Nogoshi and Igarashi (1971) were pioneers in applying a technique using H/V ratios of the microtremors to estimate the site effects particularly in urban areas, popularized by Nakamura (1989). Konno and Ohmachi (1998) defined site effect as a technique later on earthquake ground motion by near-surface sedimentary deposits. The theoretical models in the last decades show the expansion of the H/V spectral ratio into two main research lines: while in one of them the H/V curve is studied by considering the whole ambient-vibration wavefield, the other one is regarding the Rayleigh ellipticity.

4-7-2 The H/V Origins: Body-Wave Based Theories

After Nogoshi and Igarashi's (1971) work, the H/V technique was developed by Nakamura (1989). The effects of the source are expected to be minimized while normalizing the horizontal ground-motion spectral component by the vertical one. Nakamura (1989) in his first theoretical explanation assumed that ambient vibrations are composed by Shear and Rayleigh waves, however, Rayleigh waves effect would vanish if the H/V spectral ratio is defined as

$$HV\ (\omega) \equiv \frac{A^{FW}_{H\ ,surface}(\omega)}{A^{FW}_{\mathrm{V},surface}(\omega)} \tag{4-1}$$

where $A^{FW}_{H,surface}(\omega)$ and $A^{FW}_{V,surface}(\omega)$ are the total spectral amplitudes of the horizontal and vertical ground-motion at the surface of the Earth, respectively, ω is the angular frequency and FW means full-wavefield. The ratio in Eq. (4-1), which can be used as the horizontal soil transfer-function is normalized by the vertical one under the conditions that the similar H/V spectral ratio computed at the bedrock is nearly unitary and that the vertical motion does not experience any stratigraphic amplification. Based on the above assumption, the amplification phenomena affecting the horizontal ground-motion would be directly indicated by the H/V ratio. Nakamura modified his interpretation of H/V spectral ratio in 2000, after receiving criticisms. In his new aspect, he considered vertically incident P and S waves along with Rayleigh waves as the main constitution of the ambient-vibration wavefield. These components were separated by writing the horizontal and vertical spectral ground-motion amplitudes at the Earth's surface as

$$A^{FW}_{\delta,surface}(\omega) = A^{BW}_{\delta,surface}(\omega) + A^{SW}_{\delta,surface}(\omega) = \mathrm{T}_{\delta}(\omega).A^{BW}_{\delta,bedrock}(\omega) + A^{SW}_{\delta,bedrock}(\omega)\,, \qquad (4\text{-}2)$$

where δ = H, V defines horizontal and vertical components, BW signifies body waves, SW is surface-waves and T_δ is the horizontal and vertical transfer functions. It can be derived from Eq. (4-1)

$$\begin{aligned} HV(\omega) &= \frac{T_H(\omega).\mathrm{A}^{BW}_{H,bedrock}(\omega) + \mathrm{A}^{SW}_{H,surface}(\omega)}{T_V(\omega).\mathrm{A}^{BW}_{\mathrm{V},bedrock}(\omega) + \mathrm{A}^{SW}_{V,surface}(\omega)} \\ &= \frac{\mathrm{A}^{BW}_{H,bedrock}(\omega)}{\mathrm{A}^{BW}_{\mathrm{V},bedrock}(\omega)} \cdot \frac{T_H(\omega) + \dfrac{\mathrm{A}^{SW}_{H,surface}(\omega)}{\mathrm{A}^{BW}_{\mathrm{H},bedrock}(\omega)}}{T_V(\omega) + \dfrac{\mathrm{A}^{SW}_{\mathrm{V},surface}(\omega)}{\mathrm{A}^{BW}_{\mathrm{V},bedrock}(\omega)}} \end{aligned}\,, \qquad (4\text{-}3)$$

which is named "quasi transfer spectrum" (QTS). Unity of the H/V spectral ratio at the bedrock is assumed, i.e.

$$\mathrm{A}^{BW}_{\mathrm{H,bedrock}}(\omega) / \mathrm{A}^{BW}_{V,\mathrm{bedrock}}(\omega) \approx 1 \qquad (4\text{-}4)$$

Neglecting of surface-wave contribution in Eq. (4-3) causes that the function HV reaches T_H/T_V. The vertical and horizontal ground-motion is related to the P-wave and S-wave oscillation respectively if just vertically incident body-waves are included. Based on this assumption, P-wave velocity is defined to be many times greater than the S-wave one. The S-wave transfer function can be estimated by the peak frequency of the function HV. As Nakamura stated in the case of governing Rayleigh waves, the peak frequency of the ratio $\mathrm{A}^{SW}_{H,surface} / \mathrm{A}^{SW}_{V,surface}$, which is the approximation of the function HV, can estimate the

S-wave site resonance frequency. Bard (1998) had fundamentally contentious opinions; he believes that the site S-wave lower resonance-frequency and the relative amplification factor can be detected by the H/V peak. The above assumptions were the premier theoretical clarification of the H/V curve, which relates the peak frequency to the S-wave resonance frequency and amplitude of the function HV to the amplification factor of the site. Although it was not a complete explanation, it opened the door to further investigation about the H/V technique. In most cases, the amplitude of the H/V curve does not give a good estimation of the amplification factor, on the other hand, the peak frequency of the curve is in good agreement with the S-wave resonance. Malischewsky and Scherbaum (2004) represented that the analytical formulae for the Rayleigh ellipticity explains the peak frequency if the impedance contrast is high enough. While Nakamura's theory demonstrates the H/V curve to be important just around its main peak frequency, Bard (1998) assumption extended the theory to the whole H/V curve.
Herak (2008) similar to the first version of the Nakamura theory, which did not regard other seismic phases except vertically incident P and S waves, suggested a way to compute the H/V curve, however, he did not make any assumption about the P-wave site amplification. The H/V curve can be computed as below, considering that Eq. (4.4) holds on at the bedrock

$$HV(\omega) \equiv \frac{\mathrm{A}^{BW}_{\mathrm{H},surface}(\omega)}{\mathrm{A}^{BW}_{\mathrm{V},surface}(\omega)} = \frac{AMP_S(\omega)}{AMP_P(\omega)}$$
$$HV(\omega) \equiv \frac{A^{FW}_{H,surface}(\omega)}{A^{FW}_{\mathrm{V},surface}(\omega)}, \qquad (4\text{-}5)$$

where $A^{BW}_{H,surface}$ and $A^{BW}_{V,surface}$, which are computed at the Earth's free surface, are given by the S-wave spectral amplitude and the P-wave spectral amplitude, respectively. Herak's method, following Tsai (1970) computed the AMPP and AMPS, which are the P-wave and S-wave amplification functions between the bedrock and the free surface. It can be noticed from Eq. (4.5) that H/V curve cannot always give a direct estimation of the S-wave transfer function, since for all desired frequencies $H/V(\omega) \approx AMP_s(\omega)$ just in the case that $P_p(\omega) \approx 1$. This estimation can be considered just when P-waves propagates much faster than S-waves through the topmost layers, which means relatively high Poisson's ratios, hence their resonance frequency is very higher than S-wave one.

4-7-3 The Role of the Surface Waves

Although all authors unanimously state that microtremors are constituted of all seismic phases, the proportion of the different seismic phases has not been obviously defined till today (see, e.g., Bard and SESAME Participants (2004)). Although there is a disparity in field experiments and in numerical simulations, subsoil stratigraphy and sources characteristics can significantly influence the composition of different seismic phases in different frequency ranges. While many theories based on the contribution of body waves in the microtremors exist, theories that consider surface-wave dominance have arisen. Nogoshi and Igarashi (1971) found that Rayleigh's fundamental-mode is the dominant phase in microtremors by comparing H/V curves from microtremors with the ellipticity pattern of Rayleigh fundamental-mode. Afterward, his theory was confirmed by other authors (e.g., Tokimatsu 1997; Konno and Ohmachi 1998; Wathelet et al. 2004), which can be due to the Rayleigh waves energetic predominance.

Tokimatsu (1997) followed Nogoshi and Igarashi (1971) and interpreted H/V curve by the ellipticity of the first mode of Rayleigh waves. Konno and Ohmachi (1998) based their interpretation on the surface waves and stated that the ellipticity of the fundamental Rayleigh mode and the airy phase of the fundamental Love mode can illustrate the microtremors H/V peak. They also tested the role of the first higher Rayleigh mode. The Nakamura's theory (the H/V-peak amplitude roughly approximates the S-wave amplification factor) is imitated by these authors except in terms of surface waves in return of body waves since distinct proportion between Rayleigh and Love waves is reported. The H/V ratios of observed microtremors and those of fundamental mode Rayleigh waves estimated from geological data are very similar at many sites (e.g., Tokimatsu and Miyadera, 1992). The jth-mode of Rayleigh wave was estimated by Harkrider (1964) at the ground surface via applying a vertical point force L(ω) to the surface, which causes the excitation of horizontal and vertical amplitudes (Eq. (4-6)).

$$\begin{aligned} \dot{u}_j(\omega, r) &= [L(\omega)/2][\dot{u}/\dot{w}]_j \, A_j H_1^{(2)}(k_j r).\omega \\ \dot{w}(\omega, r) &= [L(\omega)/2] A_j H_0^{(2)}(k_j r).\omega \end{aligned} \tag{4-6}$$

where $\dot{u}(\omega, r)$ and $\dot{w}(\omega, r)$ are radial and vertical velocity amplitudes at the surface, respectively, ω is circular frequency, r is the distance between the point force and an observation station, $[\dot{u}/\dot{w}]_j$ is H/V ratio at a large distance r as defined by Haskell (1953), A_j is the medium response, and k_j is the wavenumber. Meanwhile, $L(\omega) \propto \omega^{-2}$ gives a good fitting for observed spectra of microtremors, especially at the longer

periods. Fig. 4-1 shows a sample model to study the three types of particle orbits during the propagation of fundamental-mode Rayleigh waves.

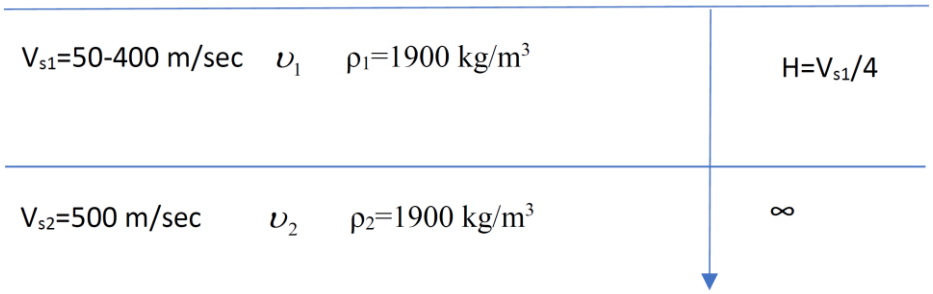

Fig. 4- 1 Model of an elastic layer over a half-space. Poisson's ratios, υ , were determined from V_s as follows: υ =0.499-1.16.10^{-4} (V_s -150), for $V_s \geq$ 150m/sec. Source: Konno and Ohmachi (1998).

Type 1 (fig. 4-2), which has a low-velocity contrast between the two layers ($V_{s2}/V_{s1} \leq 2.5$) shows retrograde particle motion in all periods, while the fairly high contrast ($V_{s2}/V_{s1} \cong 2.5$) in type 2, causes the variety of motions. By increasing the periods, the motion changes as follows: it moves with retrograde then vertical only, prograde, vertical only, and finally retrograde. In Fig. 4-2, at the periods T_1 and T_2, the H/V ratio becomes 0. High-velocity contrast ($V_{s2}/V_{s1} \geq 2.5$) in type 3 causes the particle motion to be in the order retrograde, vertical only, prograde, horizontal only, and retrograde with the increasing period. Hence, the H/V ratio becomes 0 at T_1 and infinite at T_2. It needs to be mentioned that T_1 is nearly half of T_2 in type 3. It can be derived that type 1 and type 2 do not have any sharp peaks, whereas type 2 has two deep troughs. Type 3 has a sharp peak and a sharp trough, which is nearly half of the peak period.

Asten (2004) also studied the particle motion and found that it is a function of the period for layered earth. High Vp/Vs ratio and high shear-velocity contrasts in layers may change the particle-motion from retrograde to prograde ellipses, which degenerates into pure vertical or horizontal motion at particular frequencies (Boore and Toksöz 1969). Such transitions occur for soft layers where Vp/Vs exceed 2, and the shear velocity ratio between the layer and its substrate exceeds 2.5 as shown in Stephenson (2003).

The theoretical explanation for the ‘‘holes’’ in the observed vertical-component spectra mentioned by Bodin et al. (2001) is due to the absence of vertical motion energy at periods corresponding to the horizontally degenerate particle-motion ellipse. Moreover, the numerical simulation performed by Lachet and Bard (1994) showed that the fundamental mode of Rayleigh waves is dominant at the longer periods of the H/V ratios.

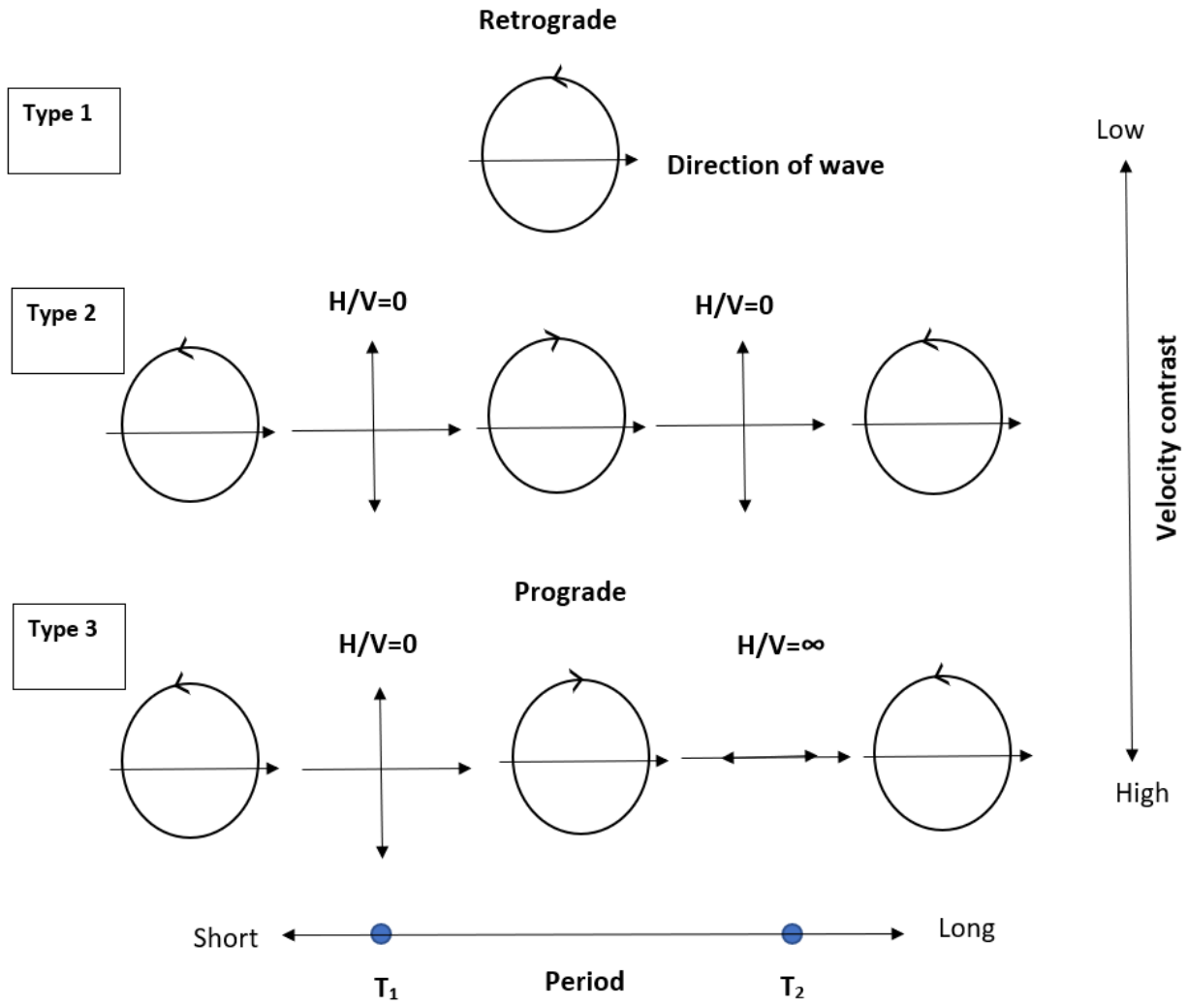

Fig. 4- 2 Particle orbit of three types of fundamental-mode Rayleigh waves for the models in Fig. 4-1. Source: Konno and Ohmachi (1998).

In the microtremor H/V ratios, it is possible not to see the trough of fundamental-mode Rayleigh waves when higher-mode Rayleigh waves significantly dominant in microtremors. The reason is that the peak periods of the H/V ratios of the first higher-mode Rayleigh waves are slightly shorter than the trough periods. In order to investigate the relation between the peaks of H/V ratio and the noise wavefield composition, a comprehensive H/V and array analysis was applied on the noise synthetics for the considered soil model here (Bonnefoy-Claudet 2004).

(1) Assuming near sources (4 to 50 times the layer thickness) which are on the surface:

one single peak is obtained in H/V curves, and the Rayleigh waves are dominant waves in the array analysis

(2) In the case of distant sources (more than 50 times the layer thickness) which are located inside the sedimentary layer:

The H/V curve presents two peaks, and the array analysis indicates both Rayleigh waves and strong *S* head waves; fundamental Rayleigh waves and resonance of head *S* waves are dedicated to the first peak, while the second is because of the resonance of head *S* waves;

(3) In this case, no matter is the distance, however, sources are deep (located inside the bedrock):

H/V ratio shows peaks at the fundamental and harmonic resonance frequencies, and only non-dispersive body waves are defined in the array analyses; multiple reflections of *S* waves within the layer create the H/V curve. Regarding the actual noise measurement, in most cases, only one peak is shown in H/V ratio, because the H/V ratio is mainly shaped by the ellipticity of the fundamental Rayleigh waves and thus, controlled by local surface sources. Therefore, the estimation of site amplification factor is not achievable by the amplitude of H/V peak.

Nakamura (1989) believed that fundamental resonance frequency and site amplification factor would be obtained straightforwardly since the shape of the H/V curves is controlled by the *S*-wave resonance within the sediments. On the other hand, authors such as Lachet and Bard (1994); Bard (1998); Konno and Ohmachi (1998) related the shape of the H/V curves to the polarisation of fundamental Rayleigh waves, which means that an indirect correlation between the H/V peak amplitude and the site amplification would exist. Finally, the results of Lachet and Bard (1994), which show that the H/V ratio is weakly dependent on the source time function type (its frequency is clearly independent, while the amplitude is weakly sensitive) are confirmed by other authors. Measurements of phase velocity of microtremor energy using small seismic arrays consistently show that the vertical-component energy is associated with Rayleigh-wave propagation. From the above discussion, when the ground structure has high-velocity contrast, it can be concluded that the fundamental periods of the S-wave transfer functions are in a good correlation with the H/V peak periods of fundamental-mode of Rayleigh waves and Airy phase periods of fundamental-mode of Love waves.

4-7-4 Achieving amplification factor from H/V ratio

In the first step, smoothing function is the main topic that needs to be considered. To find a correlation between amplification factors for S waves and the H/V ratios of Rayleigh waves seems to be impossible as the H/V ratios of fundamental-mode of Rayleigh waves become infinite at some peak periods. At this stage, the smoothing function can solve the problem when applied before calculating the H/V ratio of the Rayleigh waves. An appropriate smoothing function needs to be used, therefore a newly proposed logarithmic one expressed (Konno and Ohmachi 1998) as

$$W_B(f,f_c) = [\ \sin(\log^{10}(f/f_c)^b/\log_{10}(f/f_c)^b\ ]^4\ \ , \qquad (4\text{-}7)$$

where b is a coefficient for bandwidth, f is frequency and f_c is the center frequency. Konno and Ohmachi (1998) found the relation between H/V peak value, R_B, of fundamental-mode of Rayleigh waves and amplification factors, A_s, for vertically incident S waves for 85 models obtained from soil data measured by the downhole method. Amplification factors can be estimated from the A_s versus R_B relation as in Eq. (4-8) if fundamental-mode of Rayleigh waves is the only contribution of microtremors.

$$A_s=2.5R_B. \qquad (4\text{-}8)$$

In the case of a combination of fundamental-mode of Rayleigh and Love waves, the H/V ratio of the microtremors can be decomposed as

$$R_M(T)=[H_R(T)+ H_L(T)]/V_R(T), \qquad (4\text{-}9)$$

where T is period, $H_R(T)$, and $H_L(T)$ are horizontal components of the Rayleigh and Love waves, respectively, and $V_R(T)$ is a vertical component of the Rayleigh waves. The proportion of the Rayleigh waves in horizontal components of microtremors is expressed as

$$\beta(T)=H_R(T)/[H_R(T)+H_L(T)]. \qquad (4\text{-}10)$$

Combining Eqs. (4-9) and (4-10) leads to

$$R_M(T)= H_R(T)/[\ \beta(T).V_R(T)], \qquad (4\text{-}11)$$

where $H_R(T)/V_R(T)$ denotes the H/V ratio of the Rayleigh waves. After smoothing with the function W_B, H/V ratios of microtremors are expressed as

$$R_{MB}(T)=R_B(T)/\ \beta(T), \qquad (4\text{-}12)$$

where $R_{MB}(T)$ and $R_B(T)$ are the H/V ratios of microtremors and the Rayleigh waves, respectively. Substituting Eq. (4-8) into Eq. (4-12) leads to

$$A_s=2.5\ \beta R_{MB}, \qquad (4\text{-}13)$$

where R_{MB} and A_s are the values of $R_{MB}(T)$ and $A_s(T)$ at their peak periods. Amplification factors can be obtained if the value of β at each site is defined by using Eq. (4-13). It is worth to know that the information about *in situ* β(T) is not widely available. The range of β is varying based on sites and it is between 0.3 and

0.5 according to a spatial autocorrelation study by Miyadera and Tokimatsu (1992). Therefore, A_s formula becomes very similar to Nakamura's method by substituting $\beta = 0.4$ in Eq. (4-13).

$$A_s = R_{MB} \tag{4-14}$$

Chapter 5

Polarisation analysis on Ambient noise

5-1 Basic principles

Transforming the recording into a complex-valued analytic signal using an instant-by-instant analysis of an ambient noise recording can detect Rayleigh waves. The analytic representation of a single-component time series $u(t)$ is as

$$u_c(t) = u(t) + j\hat{u}(t) = A(t)\,e^{j\Phi(t)}, \tag{5-1}$$

where j is the imaginary unit and $\hat{u}$ (t) is the Hilbert transform of u(t). The vector modulus A(t) is regarded as an invariant part of the instantaneous phase rotation since it changes more slowly than its phase Φ(t). Since phase changes cause quicker variations of signal, an envelope was devised to adjust it (Morozov 1996). For different components of ground motion, we can calculate instantaneous values of A(t) and compare their amplitudes using Eq. (5-1). The scalar form of Eq. (5-1) can be substituted by a vectorial equation when the analytic transformation needs to be extended to multicomponent signals.

$$\vec{u}_c(t) = \vec{u}(t) + j\,\hat{\vec{u}}(t) = \vec{A}(t)\,e^{j\Phi(t)}, \tag{5-2}$$

where $\vec{A}(t)$ is a complex vector and Φ(t) is a real phase. According to Morozov (1996) the multicomponent signal $\vec{u}$ (t), which can be considered as the projection of a vector moving in a multidimensional complex space obeys an elliptical route with variation in direction and length of axes. In the case of 2-D signals, the instantaneous elliptical route places on the plane of the two components, while 3-D signals stay on a plane with a variable attitude in the space. To define semi-major and minor axes of the instantaneous elliptical routes, a value of the Φ in equation (5-2) should be searched that maximizes the modulus of its real part. The particular Φ can be readily defined based on the equation of Morozov (1996).

$$\Phi_0 = \frac{1}{2}\arg\left[\frac{1}{2}\sum_k (u_k + j\hat{u}_k)^2\right], \tag{5-3}$$

where the summation in the square brackets can be extended for two or three components signals. Based on the above computations and assumption, the ellipse semi-major axe $\vec{a}$ (t) and semi-minor axe $\vec{b}$ (t) are defined as

$$\vec{a}(t) = \mathrm{Re}[e^{-j\Phi_0}.\vec{u}_c(t)], \tag{5-4}$$

$$\vec{b}(t) = \mathrm{Re}[e^{-j(\Phi_0+\frac{\pi}{2})}.\vec{u}_c(t)]. \tag{5-5}$$

The planarity vector $\vec{p}$ (*t*) produced by vectors $\vec{a}$ (t) and $\vec{b}$ (t) is defined in the case of 3-D signals to study the behavior of the instantaneous elliptical trajectory. All three vectors are mutually perpendicular. $\vec{a}$ (t,f) and $\vec{b}$ (t,f) are in the plane of the motion ellipse, while $\vec{p}$ (t,f) is perpendicular to the plane. In the case of $|\vec{a}(t)| >> |\vec{b}(t)|$, the elliptical route tends to degenerate in rectilinear ground motion. According to Schimmel and Gallart (2004), the rectilinearity can be measured as in Eq. (5-6) which presents the value 0 for the completely circular polarisation and 1 for the linear polarisation.

$$rl = 1 - \frac{|\vec{b}(t)|}{|\vec{a}(t)|} \tag{5-6}$$

5-2 Analysis procedure

The previous principals and formulas were applied in this part to extract the Rayleigh waves packets from the ambient noise and to define the polarisation direction and ellipticity. To study the variation of ellipticity and polarisation direction with frequency, the analytic transformation can be applied to time-series obtained from a recording by passing it through different narrowband filters with varying central frequency *fc*. The maximum amplitude H_{max} of ground motion on the horizontal plane accompanied by its direction can be derived by the analytic transformation of the two horizontal components, from the calculation of the vector $\vec{a}$ (t) while a measure of vertical component amplitude V can be obtained by the analytic transformation of that component. Hence, the H/V which is defined as the ratio between the amplitude of the horizontal and vertical components of ground motion accompanied by the relative azimuth

can be achieved at each instant and for the analysed frequency by dividing H_{max} by V. Different and rapid changing phases of different components have a significant effect on the instantaneous ratio between horizontal and vertical components of ground motion $\vec{u}$ (t) while the H_{max}/V ratio is behaving differently. HVIP is the new acronym that defines the H/V ratios estimation obtained from instantaneous polarisation analysis. In the classical H/V method, different H/V curves values are observed since variable types of waves emitted from noise sources that are spatially distributed widespread are overlapping.

Nevertheless, more coherent properties may be presented if Rayleigh waves are separated in the ambient noise. This kind of Rayleigh waves filtering needs the analytic transformation to be applied to all three components to obtain vectors like $\vec{a}$ (t) and $\vec{b}$ (t) and the planarity vector $\vec{p}$ (*t)* and also rectilinearity rl. The Rayleigh waves isolation can be done by detecting the polarisation of Rayleigh waves of ground motion. The Rayleigh polarisation can be in three forms; first, the case of having vertical plane including instantaneous routes and the second one is that when $\vec{a}$ (t) is horizontal so $\vec{b}$ (t) is vertical and then H/V will be greater than 1, in the last case $\vec{b}$ (t) is horizontal and similarly $\vec{a}$ (t) is vertical and then the value of H/V will be lower than 1. However, deviations from perfectly horizontal to vertical of $\vec{p}$ (*t),* $\vec{a}$ (t) and $\vec{b}$ (t) may also occur because of contamination of Rayleigh waves with noise from other types of waves. Although deviations were expected, a limitation in the definition of their ellipticity and polarisation must be considered to separate the part of the signal that Rayleigh waves have the most contribution. The angular threshold ldipp is defined for the deviations of $\vec{p}$ (*t),* from horizontality which should not exceed this threshold while for deviations of $\vec{a}$ (t) and $\vec{b}$ (t) from the horizontal to vertical directions the ldipa is defined which is a threshold not to be exceeded

In the case of Love waves separation, the threshold changes to ldipaL which means the $\vec{a}$ (t) inclination cannot exceed this value while rl must be close to 1 and more than the threshold rlim. To have a more reliable detection of Rayleigh or Love waves, a coherent type of polarisation in more consecutive samples, at least equal to nmin must be available. A more complicated but similar procedure has been applied in Schimmel and Gallart (2003, 2004) to measure polarisation stability over time using the degree of polarisation. Later investigation of them has been formed to detect Rayleigh waves in larger-scale studies (Schimmel et al. 2011).

In the end, an average of $HVIP_R$, which are the HVIP values achieved from Rayleigh type wave packets within each filtered time series, was taken to obtain a curve of $HVIP_R$ values as a function of filtering central frequency f_c versus frequency. This curve is an estimation of Rayleigh wave ellipticity as a

function of frequency. By measuring the root mean square of $HVIP_R$ deviations from $HVIP_R$, the scatter of the instantaneous $HVIP_R$ values around their average, which shows the uncertainty of computing ellipticity, can be obtained. One of the main advantages of this procedure is defining the site response directivity which can be achieved by evaluating the distribution of the azimuths of $HVIP_R$ directions; therefore, the preferential signal polarisation can represent the site response directivity.

5-3 Analyses of synthetic data

Recordings were acquired for 900 seconds with a sample interval 0.01 per second and then analysed with the standard Nakamura's technique. The HVIP analysis was also applied in the study to compare the difference in the results with the classic Nakamura method. In the first step, the recording spectral amplitude at frequency f is multiplied by the function G(f) to apply Gaussian filtering. The G(f) function is defined as

$$G(f) = e^{-\frac{(f-f_c)^2}{2\beta^2}} \tag{5-7}$$

where *fc* and β are the central frequency and the filtering bandwidth, respectively. At first, six different β values (0.05, 0.1, 0.2, 0.3, 0.4 and 0.5) were examined in filtering of 64 central frequencies from 0.50 to 16.25 Hz, spaced by 0.25 Hz. In the next step. The angular thresholds *ldipp* and *ldipa*, are chosen 5° and 10° as alternative values for Rayleigh wave identification. For *nmin* values, two alternatives 10 and 20 are considered and rlim, which is the rectilinearity limits, is varied from 0.90 to 0.98. The parameter combination providing a minimum scatter of $HVIP_R$ values around their averages $HVIP_R$ can be obtained after applying the filter for different β values. However, if after filtering very few wave packets remains, it may show a low scatter, and to overcome this problem, parameter combinations resulting in the selection of less than 1 percent of the recording data were excluded since less than this percentage the reliability of the $HVIP_R$ estimation is mitigated.

After testing with the angular threshold *ldipp* (5°), in the next step, we increase its value to 10°. Afterward, by changing the rectilinearity threshold (rlim) from 0.90 to 0.98, H/V larger than a maximum permissible value varying from 10 to 50 is excluded. In this process, samples having Rayleigh-type polarisation that have ellipticity larger than $1/(1-rlim)$ are excluded. Moreover, by increasing the rlim values, $HVIP_R$ is also surging. The optimal threshold for rlim is defined when increasing of rlim does not have a remarkable effect. The parameter combinations adopted at our model for the analysis of recordings were summarized in Table 5-1.

Table 5- 1 HVIP analysis parameters selected through the preliminary tests: β *= parameter controlling the filtering bandwidth;* ldipp *= maximum permissible inclination for planarity vector;* nmin *= minimum number of consecutive samples with coherent polarisation used to identify Rayleigh wave packets and* rlim *= rectilinearity thresholds used to distinguish Rayleigh from Love waves; fcmax= frequency of hvfcmax; hvfcmax= maximum of the H/V averages calculated from the analysis of the data among all comparison frequencies for comparison azimuths; nRfmax= number of samples of Rayleigh type for comparisons azimuth at the fcmax frequency; pRfmax= percentage of samples classified as Rayleigh for comparison azimuths on the total of those classified at the frequency fcmax; nRmed= average number of samples of Rayleigh type for the azimuths of comparison between all the comparison frequencies.*

rl	**ldipp**	**nmin**	**beta**	**fcmax**	**hvfcmax**	**s.d**	**s.d.log**	**nRfmax**	**pRfmax**	**nRmed**	**Scatter**
0.90	10	20	0.05	2.000	9.265	0.389	1.043	74	27.612	247	1.083
0.90	10	20	0.10	1.250	5.506	2.562	1.822	136	5.356	236	1.308
0.90	10	20	0.20	1.500	7.024	1.818	1.334	11	4.435	202	1.385
0.90	10	20	0.30	1.250	6.212	0.879	1.140	26	7.242	162	1.321
0.90	10	20	0.40	2.000	5.494	1.817	1.441	33	14.163	136	1.394
0.90	10	20	0.50	1.500	7.849	0.899	1.138	20	7.692	110	1.330

In the last stage the ambient noise is analysed again but this time the number of frequencies is increased to 460 between 0.05 and 23.00 spaced by 0.05 Hz to have a better knowledge of the variation of Rayleigh wave ellipticity with frequency. The $HVIP_R$ values were grouped into azimuth intervals of 10° according to the direction of the elliptical motion. Remarkable oscillations are detected within small-frequency variations by evaluating the $HVIP_R$ averages estimated for each azimuth bin as a function of filter central frequencies. Then, a Konno and Ohmachi (1998) filter was used.

Conclusively, the H/V curve achieved from Nakamura's method was compared with the smoothed mean values of Rayleigh wave ellipticity $HVIP_R$, expressed as a function of frequency and azimuth to clear the advantageous of the mentioned filtering (Fig. 5-1). The code *gpell* (Wathelet 2005) was applied to calculate theoretical Rayleigh wave ellipticity through 1-D modelling and hence to verify the reliability of the HVIP analysis results. Different vibration modes can be one reason to justify the presence of multiple peaks. Ellipticity curves modeled for the fundamental and first higher mode of Rayleigh waves are compatible with the ellipticity peaks at 2.4 and 6 Hz in the $HVIP_R$ curve (Fig. 5-3). The same noise recording analysed by HVIP and Nakamura's (1989) method and their H/V curves were compared with each other. The project SESAME (Bard and SESAME Participants 2004) was used in data processing to have reliable results. The process has the following steps:

(1) Time windows 30 s was chosen to divide noise recording and those showing anomalous H/V ratios were excluded.

(2) Konno and Ohmachi smoothing filter spectra were applied to the horizontal and vertical components.

(3) In each time window, horizontal component which is the geometric mean of the two horizontal components was divided by the spectral amplitude of the vertical component.

(4) An average is taking from all time windows on the spectral ratios HVNR.

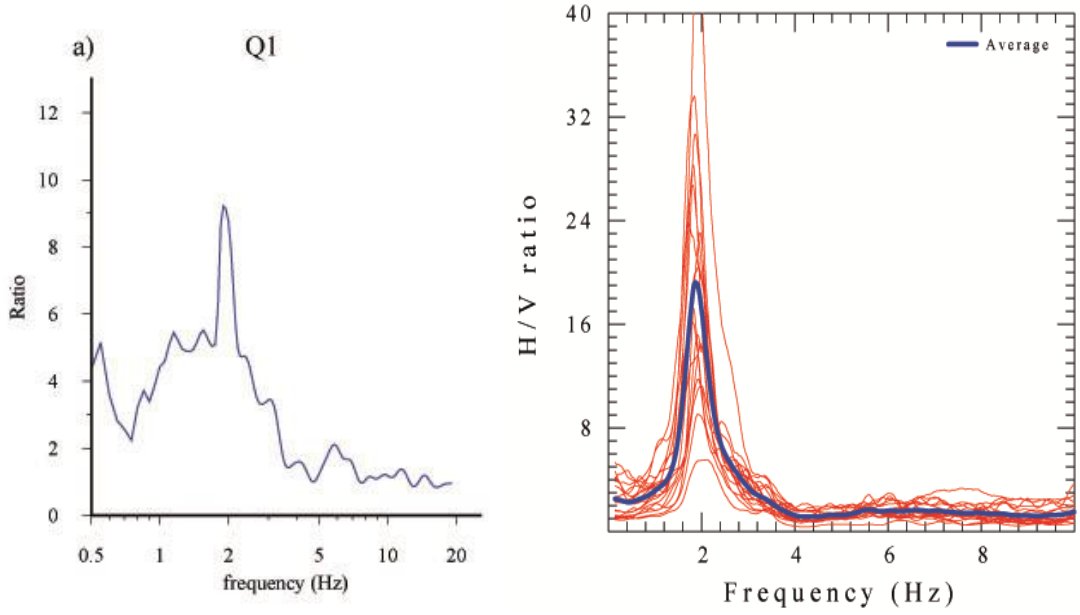

Fig. 5- 1 Comparison of HVIP (left figure) and Nakamura (right figure) H/V ratio

Furthermore, the HVNR values were computed for horizontal components with azimuths between 5° and 355° spaced by 10° to define the directional variations of spectral ratios. Fig. 5-2 shows the distribution of azimuths of HVIP maxima found in the directional analysis at different frequencies.

Comparing the result of HVIP with the HVNR, it becomes clear their similarity in the direction of maximum frequency which verifies that application of the HVNR directional variations analysis can detect frequency and orientation of directional resonance while regarding the value of the H/V ratios, HVIP shows more reliable value than HVNR. If the geometric mean of the horizontal components is used to calculate HVNR, this underestimation of the H/V ratios becomes more pronounced. Moreover, detail about the other secondary peaks which is relative to the first higher mode at 6 Hz is not defined in the HVNR analysis. The underestimate of the H/V ratios appears particularly pronounced if HVNR values are calculated as a geometric mean of the horizontal components. It can be inferred that H/V curves obtained by the use of the geometric mean can be rather specious if sites are affected by a pronounced directivity in dynamic response.

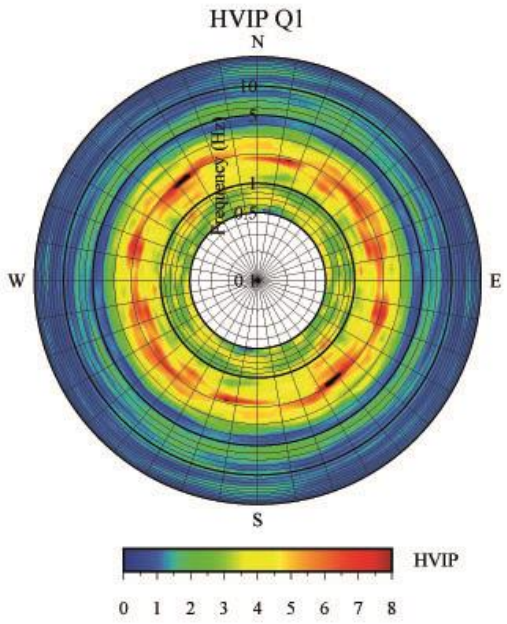

Fig. 5- 2 Polar diagram of polarisation between azimuths 0^O to 360^O

5-4 Discussion & Conclusion

Analyzing our synthetic data by the HVIP method caused a problem to select a single $HVIP_R$ curve to regard as site response properties. The directional distribution of $HVIP_R$ maxima was studied and a single strong preferential direction was not observed (Figs 5-2). It can be derived that source location and properties have an effect on the directional maxima of ground motion. Considering mechanism and size, different frequencies of waves can be polarized by sources of seismic events and noise. The direction of ground motion maxima at different frequencies led by polarized waves depends on the location and mechanism of the sources that at these frequencies have the most energized spectral response.

As shown in Fig 5-2, site responses do not show a preferential directivity, this phenomenon could mask the scattering of source-controlled polarisation. Hence, in an anisotropic distribution of sources, a single directional curve of $HVIP_R$ is not able to give complete information on site response at any frequencies.

The $HVIP_R$ values obtained in all directions can be averaged for each frequency in order to have some general indications. Such a curve shows a maximum at 2 Hz in 145, which has the highest ratio (Fig. 5-2). The averaging of $HVIP_R$ to define the directional variations of $HVIP_R$ underestimate the ellipticity measurement and therefore details on secondary peaks are eliminated. However, analysing the $HVIP_R$ curve for the particular azimuth interval, which has a maximum close to the peak frequency of the average curve

(i.e. at 2.4 Hz) can give details at least on some of the secondary peaks and also the ellipticity peak value appears larger than the average curve.

From the above discussion, it is concluded that the Nakamura's method can work properly under the condition that both site response and noise source are distributed isotropically. Directional analysis of HVNR values is able to define the main resonance frequency if the noises are azimuthally distributed irregularly around the measurement station, nevertheless, the maximum ellipticity obtained by the HVIP analysis is more reliable than this peak and also the secondary peak is missed in HVNR.

In some cases that noise sources insufficiently energizing the frequency band of maximum site amplification, HVNR estimation is less than HVIP since the latter at least can show some reliable peaks in some particular directions while the Nakamura's method shows small peaks not only at frequencies that are not significantly amplified but also with the underestimate of amplification. To sum up, a directional analysis by Nakamura's technique can have reliable results if the site response is simple.

To carry the HVIP analysis some parameters need to be defined:

1- The filtering bandwidth controlled by the factor β
2- *ldipp* which is the maximum admissible deviation of planarity vector from horizontality
3- *nmin* which is the minimum number of consecutive samples with coherent polarisation
4- *rlim* the rectilinearity threshold applied for separation of Rayleigh from Love waves.

The best combination of values varies from case to case, therefore, to find the best combination of the parameters that results in a minimum scattering over a data set, preliminary tests are needed.

In the case of having lower SNR, a larger filtering bandwidth is required in the first step to exclude the parts that do not represent polarisation of Rayleigh waves. If a lower number of Rayleigh-type data grouped in shorter wave packets, larger β values are the best option for recordings as *nRav* and *nRp* in Table 5-1. This condition may happen when the level of noise is higher. Choosing the nmin is less crucial since it is just defined to exclude very short time-series that could consist of incoherent noise, which accidentally may pass the Rayleigh wave identification criteria. Choosing the value 10-20 for nmin is acceptable since it relates to the interval of 0.1 to 0.2 seconds which is much shorter than the mean length of Rayleigh wave packets. However, choosing alternative values do not have a significant influence on the results. On the other hand, the threshold rlim needs much more considerations since this threshold could exclude Rayleigh waves at frequencies very close to resonance conditions, for which ellipticity tends to infinity. To have more reliable results of $HVIP_R$, the value of rlim is increasing till more increasing does not have a remarkable effect on the ellipticity peak. However, the elimination of the vertical component and in conclusion the infinity of H/V does not occur in real data since the data is contaminated with noise. Overlapping of different kinds of waves causes that most of an ambient noise recording consists of signals without a coherent type of polarisation.

Generally, a small fraction of the recording samples and, on average, for time intervals shorter than 1 s, which relates to the arrival of the most energetic part of Rayleigh waves is dedicated to Rayleigh-type polarisation. The main discrepancy between HVIP and Nakamura's method is that the Nakamura average the H/V estimates over the length of the recording in which different types of waves can come along with Rayleigh waves.

The main objective of applying HVIP is to study the site response more accurately due to the ambiguous characteristic of ambient noise. There are some similarities between the HVIP method and other techniques of polarisation analysis. For instance, Jurkevics (1988) polarisation analysis has been applied in site response studies based on the analysis of earthquake recordings. The instantaneous properties of the particle motion are calculated in Vidale (1986) to analyse earthquake recordings which shows the most similarities to the HVIP approach, while Burjánek et al. (2010) tested on ambient noise. Applying polarisation analysis simultaneously to the three components of the recording to identify Rayleigh wave packets makes the HVIP approach different from Burjánek et al. (2010). To calculate ellipticity, Hmax and amplitude V are computed by applying analytic transformation separately to the horizontal and vertical components, respectively. The contaminations have effects on the deviations of the plane of the Rayleigh wave particle motion from verticality, the deviations of the axes of the elliptical trajectory from horizontal/vertical directions, and the deviations of the horizontal component of Rayleigh waves from rectilinearity. Therefore, all these deviations can be diminished if Hmax/V is calculated instead of the ratio a/b between the axes of the elliptical trajectory. However, the interpretation of single recording data can be objective since some results may be biased by the presence of sources exciting strongly polarized signals in a wide frequency range. For instance, dominant winds can cause high trees and buildings to oscillate in the same direction with different oscillation periods.

To overcome this ambiguity, analysing the HVIP under different environmental conditions should be applied to determine whether the $HVIP_R$ curves are relevant to site-specific properties of ground vibration or to noise source characteristics. We have no predictability in justifying the ellipticity curve at sites that show multiple and differently oriented maxima by the dynamic response. It implies the effect of factors controlling amplification at different frequencies. These factors, which appear along directions of source-controlled wave polarisations, may act isotropically or have different directionality. HVIP analysis interpretation becomes cumbersome when the whole of the spectral band is not energized by noise sources and also when they have an anisotropic spatial distribution around the recording station. In the discussed conditions, the real ellipticity curve for the entire frequency band cannot be achieved by the $HVIP_R$ curves obtained along any selected azimuth or a curve averaging Rayleigh-type signal with any polarisation.

In conclusion, the ill-conditions of noise excitation during data acquisition, which does not allow having a correct interpretation, are the most significant limitation in using HVIP analysis. One of the main

applications of this analysis is on the complex site response, multiple resonance frequencies with site-specific directivity, which can present site response better than Nakamura's method. However, in flat horizontal layering where site response is characterized by a single sharp maximum Nakamura's technique can also be acceptable.

Chapter 6

Application of polarisation analysis of ambient noise in defining site response directivity in landslide-prone slopes

6-1 Introduction

The damages every year caused by slope failures motivate near-surface engineers to find solutions to diminish them. Among the factors responsible for slope destabilization, earthquakes deserve special attention for their capacity for activating a large number of simultaneous mass movements, aggravating the management of seismic emergencies. These phenomena can be favoured by the dynamic response of marginally stable slopes under seismic shaking, depending on a variety of factors such as the slope material properties, the presence of discontinuity systems, the shape of geological bodies, and topography. Slopes prone to landslides when subjected to seismic effects can be more easily mobilized during earthquakes in presence of ground motion amplification due to subsoil physical properties (Bourdeau and Havenith 2008) or topography (Sepúlveda et al. 2005), characterized by directional variations of resonance phenomena. The effects of directional resonance have been studied on soil slopes by measuring seismic ground motion at slopes susceptible to landslide, which revealed the occurrence of stronger spectral amplifications aligned with the maximum slope direction at site-specific frequencies (Del Gaudio and Wasowski 2011). A similar result was attained by Burjánek et al. (2010) at the Randa rock slope in Switzerland, where the maximum ground motion amplification was oriented along the steepest slope.

The most direct way to evaluate such phenomena is through the SSR (standard spectral ratio) technique, which requires acquiring several recordings of seismic events at study sites and at a nearby reference site to compare site response characteristics. However, the scarcity of ground motion recordings acquired on the rough topography of landslide-prone regions through long-term accelerometer monitoring has reinforced the necessity of using other techniques to have an exhaustive evaluation of site effects. The study of subsurface geology via boreholes and other geophysical approaches can be very costly and is generally restricted to post-failure investigation. However, numerically modelling slope behaviour is complex due to intricacies in geotechnical data acquisition for sites with unique topography and lithology. The limits and constraints of different methods motivate researchers to adopt short-term ambient noise recording as a suitable and cost-effective alternative method in monitoring landslide-prone slopes (Vella et

al. 2013). Using appropriate instruments, ambient noise, which is observed ubiquitously, can provide information about the role of subsurface structure on site response at observation stations. Spectral amplification studies on landslide regions show that the orientation of a sliding mass can influence directional resonance (Del Gaudio et al. 2008).

The most commonly used approach for ambient noise analysis is Nakamura's method, also known by the acronym HVSR (horizontal-to-vertical spectral ratio—Nakamura 1989), in which the spectral ratios, H/V, between the horizontal and vertical components of ambient noise recordings are analysed, revealing site-specific resonance frequencies through H/V curve peaks. Directional resonance can be recognized through analysing azimuthal variations of spectral ratios.

Evaluating resonance at low frequencies, which can favour triggering large landslides, can be problematic for the presence of distant persistent sources of polarised noise. One solution to resolve this problem is using simultaneous recordings at different sites in the same study region to define the low-frequency polarisation. Additionally, measurements can be repeated in different seasons to clarify if the polarisation is a site characteristic or presents seasonal variations. It is worth mentioning that some sites are more susceptible to undergoing stronger shakings in a specific direction and frequency range, which is of interest for earthquake engineers. Landslides can be responsible for some of the directional peaks but other factors, such as topography, geology, lithological and tectonic features, are involved in generating this phenomenon (Del Gaudio et al. 2018; Kleinbrod et al. 2019). Moreover, pre-existing landslides can increase the susceptibility of slopes to seismically induced failures due to seismic wave trapping generated by a high impedance contrast with the underlying stratum and the 3D geometry of a landslide body. This phenomenon makes studying pre-existing landslides more important.

The primary aim of the present study is to evaluate the feasibility of detecting directional site amplification that could favour land sliding on an unstable slope, threatening the village of Nargeschal in a mountainous area of northern Iran. The first step in a comprehensive risk assessment is a site response survey. Therefore, an approach based on ambient noise analysis was conducted at four sites, the crown of the landslide, the ridge of the sliding mass, the body of the mobilized mass and a reference station (Fig. 6-1). The ambient noise analysis was preferred to other methods due to the rare occurrence of strong earthquakes and lack of permanent seismic and portable networks in the region.

The application of the Nakamura's method to site conditions characterized by topographic relief and complex geology can show limitations even in the recognition of the resonance frequencies when amplification acts at multiple frequencies and with a pronounced directional variation (Del Gaudio et al. 2008; Del Gaudio 2017). Landslides can be responsible for some of the directional peaks, although other factors, such as topography, geology, lithological and tectonic features, are involved in creating this phenomenon (Del Gaudio et al. 2018; Kleinbrod et al. 2019). Therefore, we used the new ambient noise

analysis, defined with the acronym HVIP (horizontal to vertical instantaneous polarisation: (Del Gaudio 2017)), to provide more reliable results under complex site conditions (Del Gaudio et al. 2018, 2019).

The combination of active river erosion, abundant rainfall and the seismic potential of the study region increase the possibility of various types of mass movements. The complexity of the area strengthens the necessity of using more tools in investigating the sliding mechanism and substratum materials. Therefore, electrical resistivity tomography (ERT) and geotechnical surveys were also conducted to provide a more precise insight of substratum materials and sliding surface depths. Finally, ambient noise recordings were analysed to provide additional constraints on the factors inducing a landslide.

Our results present ambient noise analysis as a low-cost, agile and easy to operate reconnaissance technique for seismic landslide hazard assessments on slopes susceptible to hazardous consequences of directional amplification. The outcomes will be constructive in solving the difficulty of understanding the factors responsible for site response directivity. Additionally, we believe that our findings may improve knowledge about the substratum materials, and consequently, the sliding mechanism in the area. Our procedure could be applied to detect fracture systems in fault zones and to identify sites potentially exposed to site response directivity, defining the slide direction of mass mobilisation. It also has application in earthquake hazard reduction programs and land use planning.

6-2 Region survey

The study area located in the mountainous village of Nargeschal, in Golestan Province in northern Iran (Fig. 6-1). The area is in the third unit of the Shemshak Formation, which is divided into four sub-units and includes marl, weathered shale, sandstone and conglomerate. According to the landslide hazard zone map of the province provided by GSI (Geological Survey & Mineral Exploration of Iran), this range is in a high-risk zone, which makes a landslide the most significant geological hazard in the study area. A topography with steep slopes (almost 30^{o}) along with the sequences of soft and sticky rocks with relatively hard and fragile rocks provides conditions for moving in direction of gravity. Also, the region's tectonic activity stores dynamic stresses from earthquakes.

Many of the evidences, such as alteration of surface morphology (Schuster and Highland 2003), tilted trees (Singh et al. 2014), ground-level differences, different slope angles of the sliding mass compared to the surrounding surface (van Westen et al. 2006), sedimentation (Chen 2009) and so on, could help identify old landslides. Based on these shreds of evidence, 18 small, old landslides have been identified in the study area. The vector of their motions is often towards the slope dip in the northeast direction. These small landslides are mainly on the bed or the outskirts of rivers passing through the village and have been stimulated by the larger landslide. In the study area, large landslides have also occurred, which are older

than the small ones, and a large area is affected by their movements. The great adaptation and convergence between the old landslides and the new ones in many areas show that the new mass movements occurred on the sliding surface of the old landslide. This fact verifies that the Nargeschal landslide has a long history and is still active.

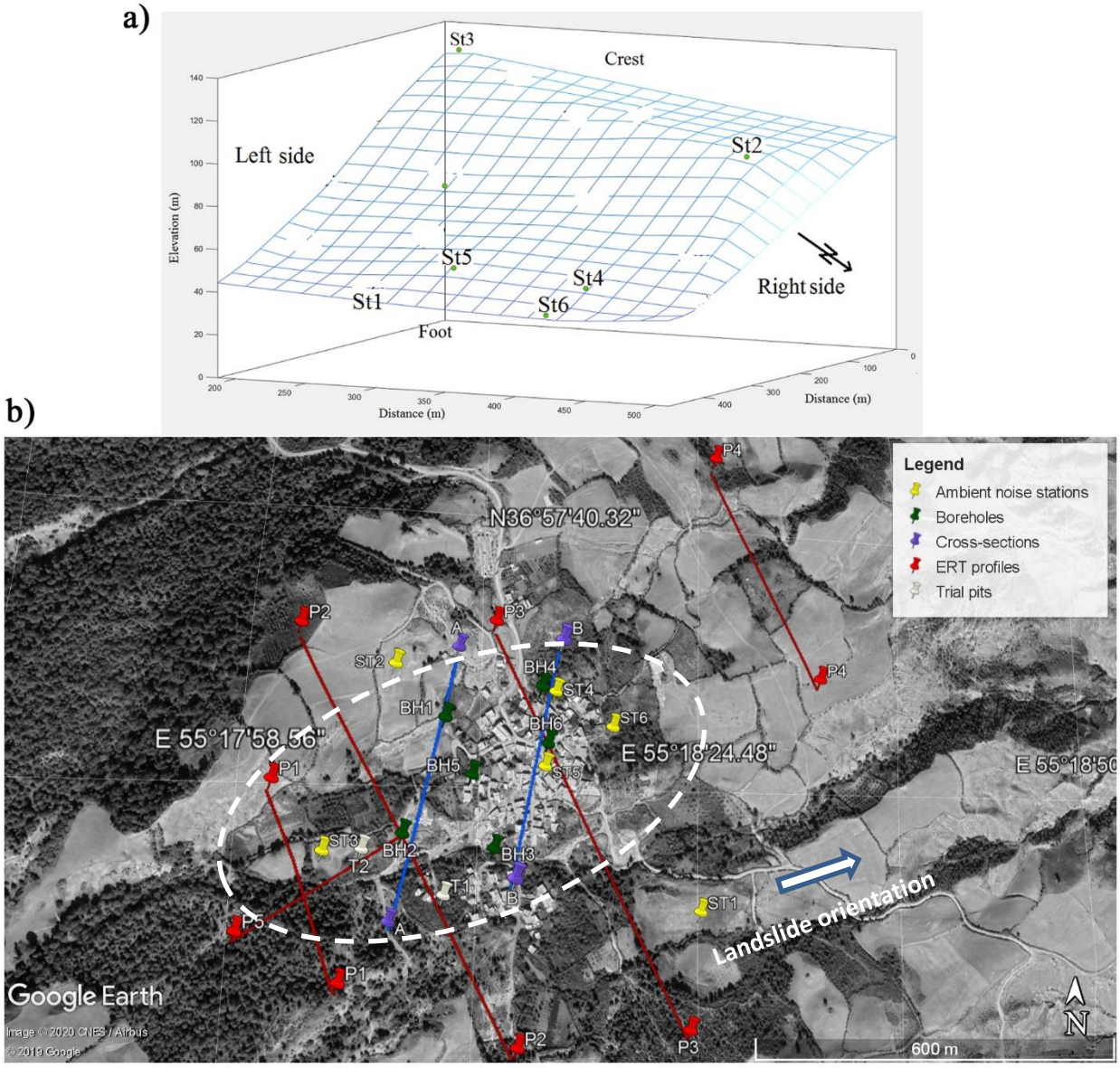

Fig. 6- 1 a) Topography of the stations, b) Aerial map of Nargeschal village with the locations of boreholes and trial pits, cross-sections A and B, ambient noise stations (ST1-6) and ERT profiles, (P5 is in the direction of moving mass, P1-4 are perpendicular to the sliding direction), the white-dashed ellipse delimits the landslide area, b) Topography of the stations.

Generally, there are two types of landslides in the study area, old ones, whose effects are visible on the ground surface, and recent ones, which mostly adhere to the pattern of old landslides. In many areas, the new sliding surfaces are consistent with the old ones; hence, the sliding mechanism and the factors affecting their occurrence is conceivably the same. The zonal landslide pattern represents two different movements with two distinct mechanisms. The principal and permanent movement are in the river course leading to Nargeschal village in an approximately east direction. The other movement is a function of slope dip and has created small and local landslides. The vectors of motion in the landslides of the region show three main directions towards the northeast, east and southeast (Fig. 6-2). The vector of the principal sliding movement is toward the east, while smaller slides follow the two other trends.

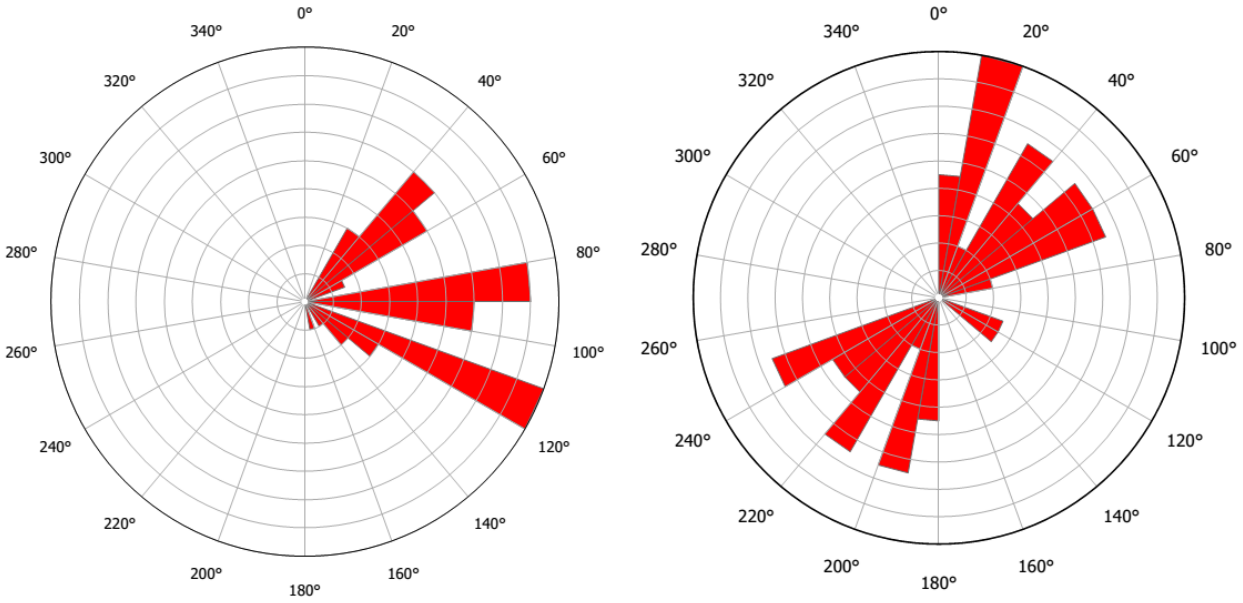

Fig. 6- 2 Rose diagram representing the main vector of landslide movements based on the Nargeschal region landslide map (left figure) and the fracture and fault orientations (right figure) in the study area.

In general, several factors favour landslide mobilizations: a) increasing shear stress, such as fatigue stresses, due to earthquakes, traffic, lightning; b) increasing slope due to regional elevation; c) application of lateral pressure (water pressure, freezing, inflation) and d) decreasing shear strength due to weathering slope material (Guzzetti et al. 2008). The sequences of shale, marl, sandstone, siltstone and their bedding dip similar to that of slopes have provided conditions for increasing shear stress by increasing the dip, notwithstanding the lateral pressures due to material saturation, are the primary internal factors for increasing shear stress in the region. However, the presence of water increases the weight of the material overlying the sliding surfaces. Additionally, recent investigations on the Nargeschal landslides showed that earthquakes could be a triggering factor for sliding in the study region.

On June 1, 2014, three days after severe precipitation, a magnitude 3.6 earthquake with 8 km epicentre and five aftershocks occurred on two sides of the Sorkhdareh active fault. The Nargeschal landslide occurred three days after these earthquakes and displaced approximately 2 Mm^3 with translational movements. The earthquake may have been a predisposing factor for the Nargeschal landslide and, together with flooding in the Nargeschal basin, may have accelerated exceeding the equilibrium limit.

6-3 Geotechnical surveys

Geotechnical surveys in this thesis cover the boreholes, laboratory and field tests.

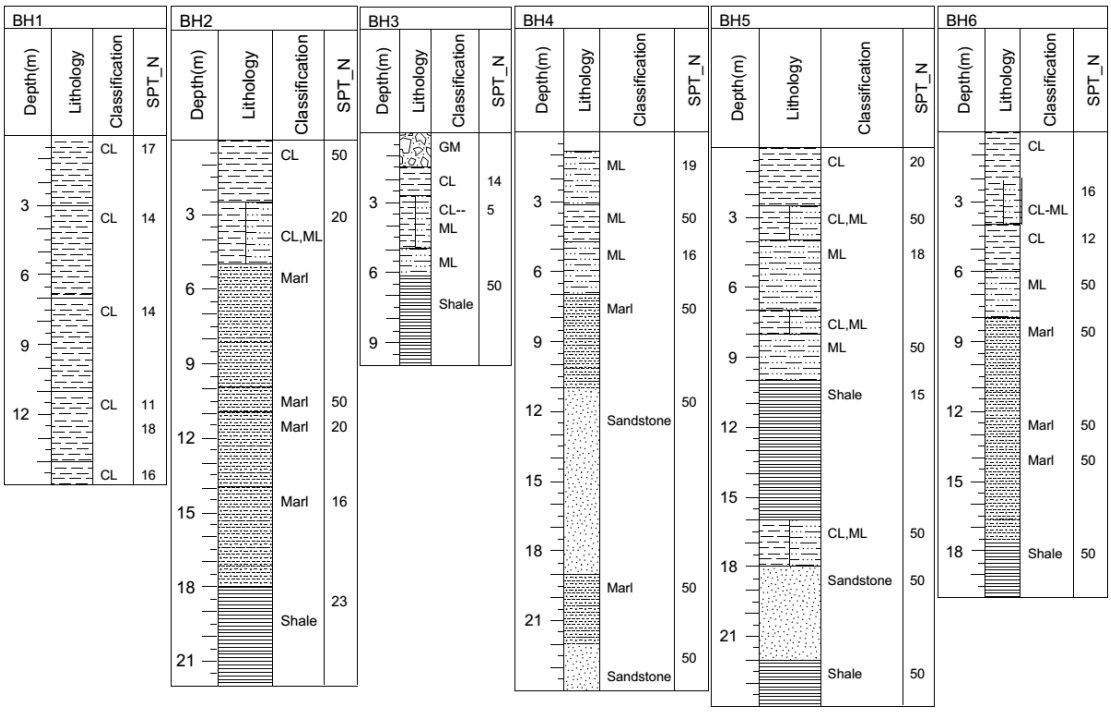

Fig. 6- 3 Boreholes drilled in the study area with their corresponding lithology

To acquire sub-level information, six boreholes were drilled for a total of 114.5 meters (Fig. 6-3) down to the bedrock or the hard material; the water level was seen in all boreholes. The samples taken from the boring operation were used in laboratory tests such as soil particle analysis, unit weight evaluation, specific gravity determination, moisture content measurement, Atterberg limits, and direct shear test. Furthermore, standard penetration test (SPT), which is a popular test for studying the geotechnical properties of soils of weathered rock was conducted (Oh and Sun 2008). Landslide material stiffness, which is useful in slip surface detection, can be achieved via SPT-N (Mori et al. 2013; Topsakal and Topal 2015).

Besides the boreholes, two trial pits were also drilled down to 4-5 m below the surface to verify the ERT results and as a tool for slip surface determination (Fig. 6-1). One perk of trial pits compared to borings is that the soil can be visually seen in trial pits. The geotechnical properties of the slip surfaces obtained from laboratory tests are detailed in Table 6-1. The slip materials are mainly clay and silt loam according to the boreholes and geotechnical tests. The shallow sliding depth detected in BH2 and BH5 is due to the surface rupture while the deeper one represents the basal slip surface. These surfaces can also be detected via the deformation in the core samples collected from boreholes since the soil under the slip surface is stiffer during the trial pits drilling.

Table 6- 1 Geotechnical properties of the slip surfaces

Boreholes	**Sliding depth**	**Natural moisture**	**Plastic limit**	**Liquid limit**	**Slip**
BH1	11	15	22	30	Clay
BH2	5, 15	19	20	37	Marl
BH3	3.5	34	25	30	Silt loam
BH4	6	18	25	30	Silt
BH5	6, 11	21	23	33	Silt
BH6	6	15	18	30	Clay

The results of borehole data and the rock layers outcrop of geological profiles are mapped in two approximately perpendicular directions to the general sliding orientation to investigate the underlying geological situation (Fig. 6-1). The sliding surface and the separation of sedimentary units are defined according to the surface survey data and geotechnical findings. The geological cross-sections illustrate six sedimentary sequences from the Shemshak Formation (Fig. 6-4).

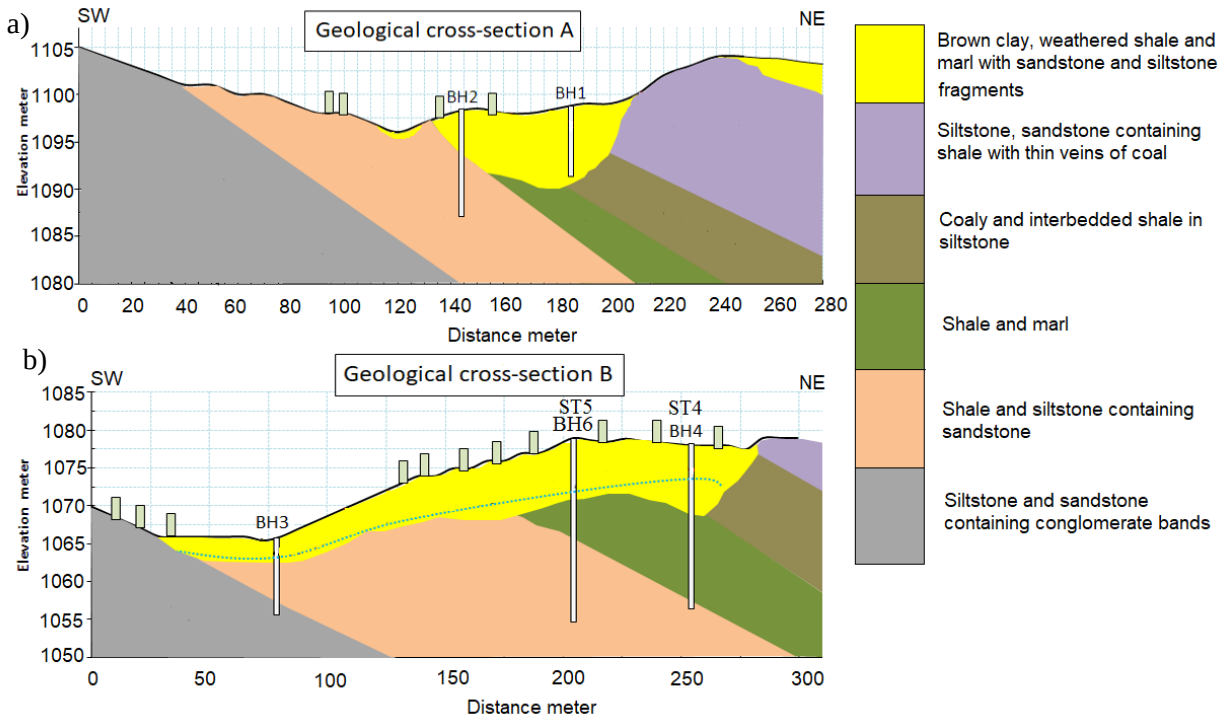

Fig. 6- 4 Geological cross-sections A and B, as located in Fig. 6-1. The blue dotted line in (b) represents the water content

6-4 ERT results

Electrical resistivity tomography is one of the most employed approaches in the geophysical prospecting of shallow structures (Telford et al. 1990). This method measures the electrical potential difference between two electrodes while direct current is introduced into the ground between two others. Different electrode layouts can be used: one, aimed at vertical electrical sounding (VES), acquires information on resistivity at increasing depths and other measures along a horizontal profile. The heterogeneity of materials along with the lateral variation of physical parameters in landslides makes interpretation difficult for 1D techniques. Therefore, the combination of the two acquisition modalities renders information on 2D resistivity variations in a form named ERT. The main reason that this technique is effective in landslide investigations is its sensitivity to various factors relevant for slope stability, like the water content, fractures, clay percentage and its potential in detecting the sliding surface.

Despite the simplicity of this technique, more consideration is required in choosing an array configuration. Therefore, the array Wenner-Schlumberger (WS) owing to horizontal and vertical resolution with high signal strength is preferred in this study to obtain five ERT profiles. Resistivity data were collected on 5 profiles: P1, P2, P3 and P4, distributed from the landslide head to the toe along directions perpendicular to the landslide movement and P5 in the upper part of the landslide, parallel to the movement direction. For three of them (P1, P4 and P5) an ABEM Terrameter SAS 4000 was first used with a 10 m

electrode spacing, whereas the other two profiles (P2 and P3) were measured by Geomative-GD10 owing to its fast and accurate measurements later after the first measurement (Fig. 6-1). The profiles initiated outside the landslide region to detect the lateral slip surface of the landslide. The electrical resistivity was obtained by inverting the measured data using RES2Dinv software, which relies on the least square approach and the finite element (FE) solutions. For all profiles in this study a RMS less than 5% was obtained for the inverted models (Table 6-2), which is commonly used as an acceptable limit for the misfit between theoretical and experimental values (Devi et al. 2017).

Table 6- 2 The details of the profiles and inversion parameters

Profile	**P1**	**P2**	**P3**	**P4**	**P5**
Length (m)	190	470	470	190	190
Array	WS	WS	WS	WS	WS
Number of iterations	5	4	4	4	5
RMS (%)	3.98	3.17	2.47	4.01	3.19

The ERT study aims at defining the landslide geometry (lateral and basal limits of the sliding surface). The sliding surface varies from ground level to a depth of about 20 meters were identified in different profiles (dotted lines in Fig. 6-5). The location of lower resistivity zones, related to the water content, is consistent with that of the springs that have been recognized in the field surveys.

According to the ERT results, the field observations, geotechnical and geological information, sandstone and conglomerate show high electrical resistivity while clay and silt are characterized by low electrical resistivity in the study area, which is representative of the slip surface (Rezaei et al. 2019; Kazemnia Kakhki et al. 2020)

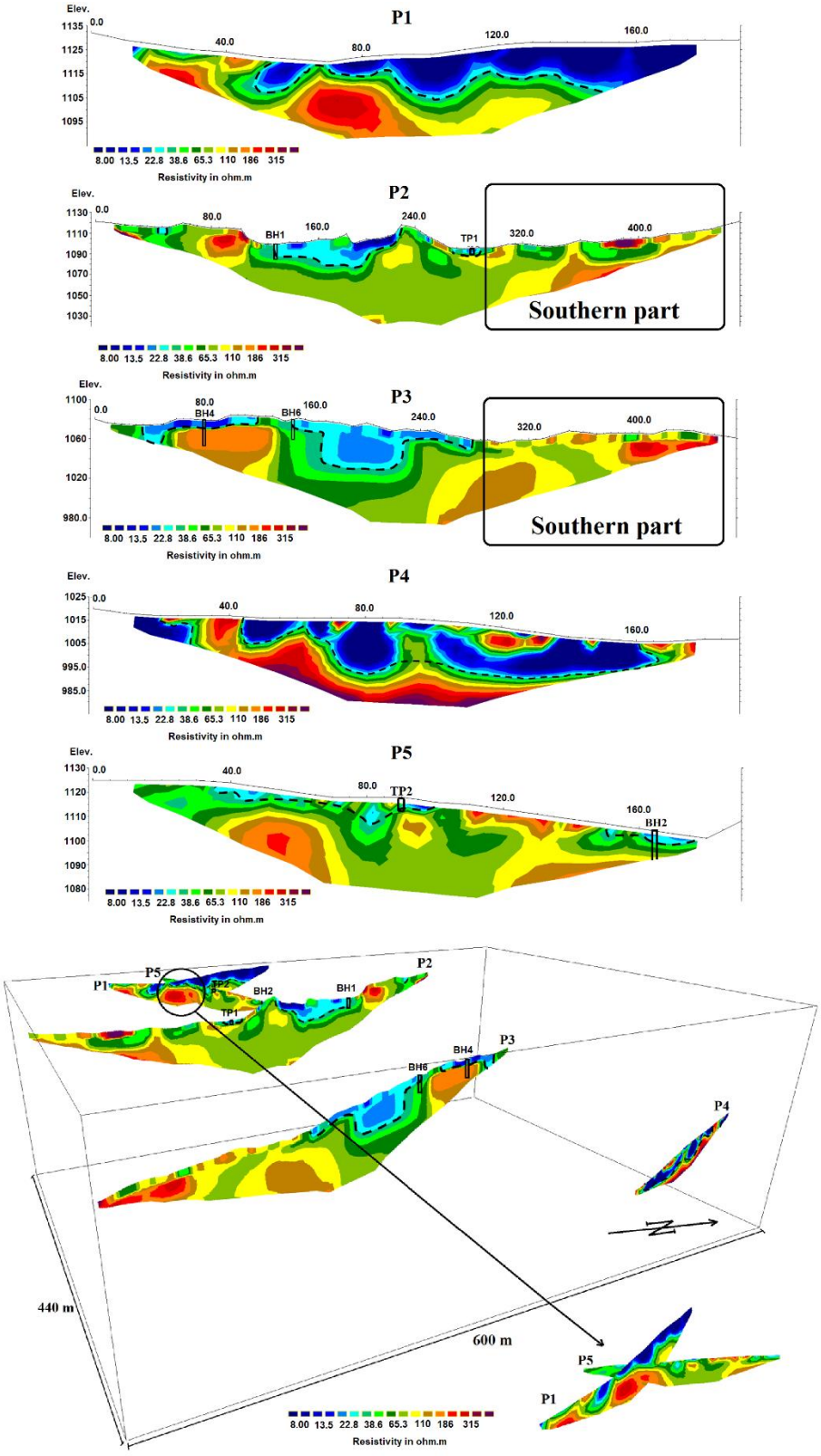

Fig. 6- 5 The ERT profiles and their quasi 3D view (the black dotted line is the sliding surface)

6-5 Ambient noise method

The seismic noise recording was set up in April 2015 in the Nargeschal landslide area to study differences in slope dynamic response to seismic shaking under different lithological and topographic conditions. The seismometers used in this survey are four of all-in-one broadband tri-axial CME 4211 seismometers (diameter 180 mm, height 140 mm, weight 4.3 kg). This instrument, which has a 2000 v/(m/s) sensitivity and requires, at most, a 27 mA power consumption with a 12 V DC nominal power supply (10.5–30 V permissible), is equipped with an acquisition system and a GPS tracking device. The sensors have a homogenous response in the 0.03–50 Hz frequency interval (see http://r-sensors.ru for more details).

The recordings were acquired at four different sites: (1) a reference site located out of the region affected by the mobilized mass on a nearly flat outcrop made of siltstone and sandstone (ST1), (2) the rim of the sliding mass (ST2), (3) close to the crown of the landslide (ST3), and (4) on the landslide body, where two stations were set up in the middle of the mobilized mass (ST4, ST5), and one (ST6) near its foot (Fig. 6-1). The recording was repeated seven times in one day and lasted for 30 minutes each time to verify data accuracy. The analysis was extended down to 0.3–0.5 Hz since the effect of very far sources with source-controlled directivity (e.g. oceanic storms) are typically at frequencies lower than 0.2 Hz. Previous studies recommended that, to verify that the observed peaks are not due to particular environmental conditions at the time of data acquisition, measurements should be repeated at different times and, possibly, in different seasons (Del Gaudio et al. 2014).

For proper evaluation of the HVSR result uncertainty in determining the frequency, azimuth and amplitude, the SESAME guidelines (Site EffectS assessment using AMbient Excitations (Bard and SESAME Participants 2004)) were followed to prevent effects related to bad soil-sensor coupling, proximity to buildings or weather conditions on the results. Therefore, in the study area, seismic responses were investigated to find any directional variation of spectral properties by applying the well-known single station method (Nakamura 1989) to calculate the spectral ratios between the horizontal and vertical components along different azimuths. Based on the SESAME instructions, Fourier Transforms were calculated for at least 20 time-windows of 25 s and spectra were smoothed using a triangular average on frequency intervals of ±5% of the central frequency. Afterwards, the spectra of horizontal components, oriented at 10° azimuth intervals, were divided by that of the vertical component, averaging the resulting ratios over all the recording intervals, in each direction and for each station to obtain azimuthal variations at each frequency.

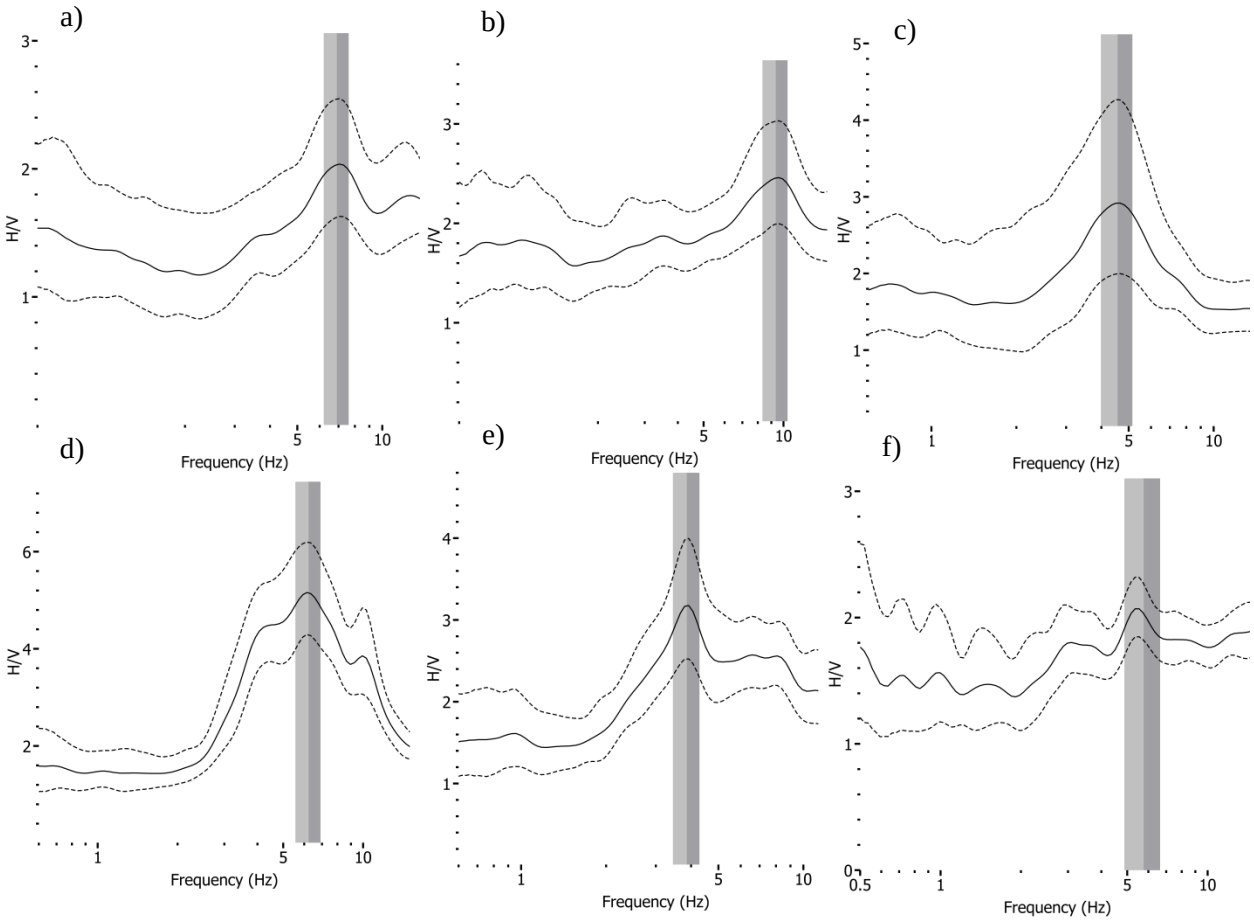

Fig. 6- 6 H/V curves obtained from a geometric average of the horizontal components as a function of frequency (black solid lines) calculated for stations: (a) ST1, (b) ST2, (c) ST3, (d) ST4, (e) ST5 and (f) ST6. Dashed lines represent the standard deviation from the average and the grey areas are representative of frequency peak precision.

One challenge of HVSR technique is the presence of near-surface geological bodies whose geometry notably deviates from 1D layering which causes the H/V ratios represents lower and broader maxima compare to those seen on a 1D layering with similar thickness. The ambiguity in noise wave-field nature and noise source location provides complexity to their processing and interpretation. Therefore, it is required to benefit other complementary data in modelling shear wave velocity profile and make the solutions more compatible with the real data. Indeed, the frequency of H/V peaks is representative of the S waves resonance frequency, even when Rayleigh waves are dominant in the noise (Asten 2004). The inversion of H/V curves obtained from noise analysis renders the shear wave velocity profiles of slope materials which are the primary input in numerical modelling of site dynamic response.

When the H/V spectral ratios (Fig. 6-6) were estimated (by Geopsy software), the Dinver and OpenHVSR software tools (Wathelet et al. 2004; Bignardi et al. 2016) performs the inversion to obtain the

shear wave velocity profile of the soil in the region. The data obtained via Boreholes (Fig. 6-3), geological profile (Fig. 6-4), and ERT profiles (Fig. 6-5) were used to make a proper initial subsurface model. The inversion result of H/V spectral ratio at station ST3 is presented as an example in Fig. 6-7.

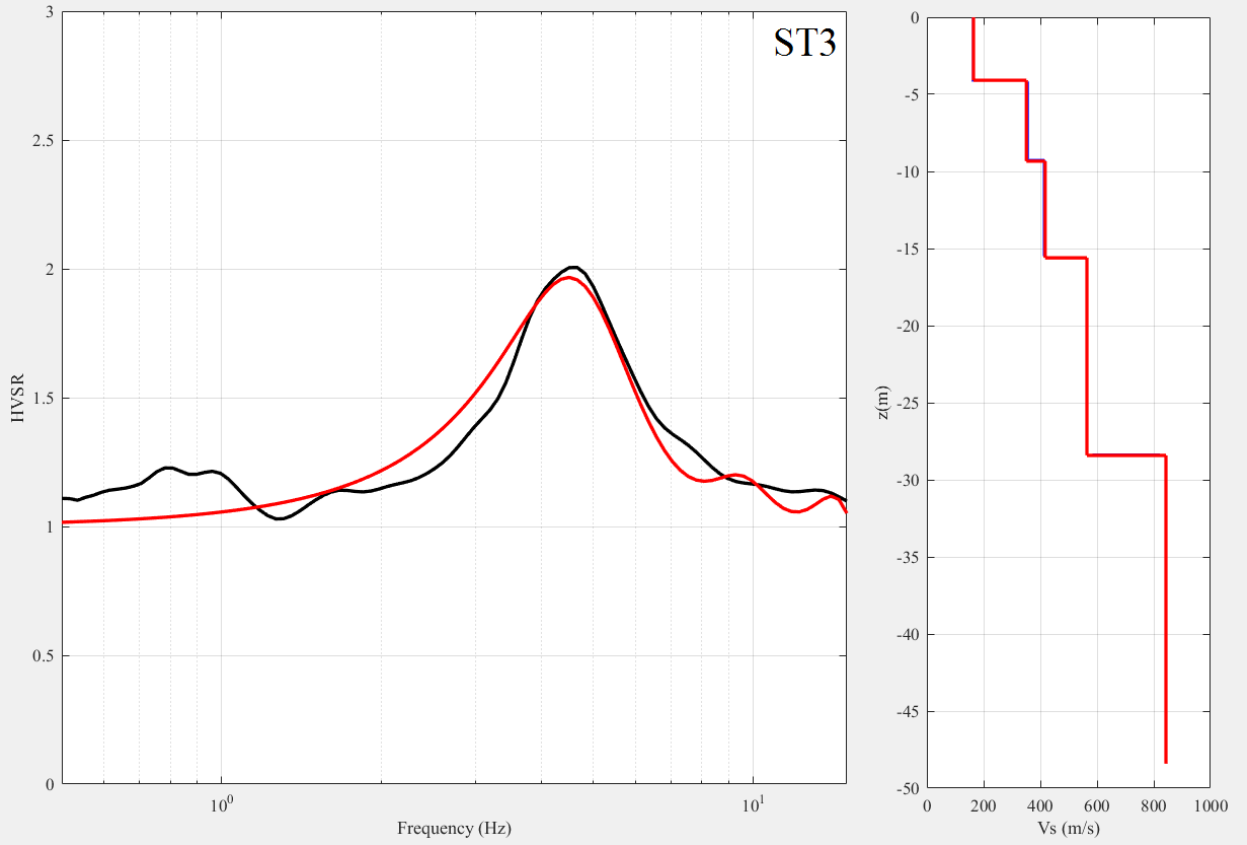

Fig. 6- 7 The inversion results of the experimental H/V curve, assumed as representative of ellipticity curve of Rayleigh waves, at Station ST3. The red curve is the estimated curve best fitting the empirical H/V curve (black curve). The relevant shear wave velocity profile is reported beside the curve.

It is worth mentioning that the shear wave velocity profiles derived from the inversion of the ellipticity curves were verified by the available geotechnical and ERT results, which were in the vicinity of these stations. Fig. 6-8 depicts a good agreement between the shear wave velocity profile obtained at station ST4 and SPT-N changes in borehole BH4. Since SPT-N reflects the stiffness of ground materials and the slip surface has minimum strength in failure conditions; therefore, the depth of 6 m in BH4 can be identified as a slip surface. Besides, the shear wave velocity shows variations in geological layers at depths of 6.31 m and 17.5 m which are compatible with the geological cross-section with lithology variations at depths of 9.5 and 20 m under the station ST4 (Fig. 6-8 b). Considerably, the ERT profile P3 also confirms the change of geological layer at a depth of 7 m.

At station ST5, the shear wave velocity represents variations at depths of 6, 12.3, and 28 m, the geological cross-section shows the changes at depths of 8 and 13.5 m under this station, the ERT represents

the variation in geological layering at depths of 8, and 11 m, and the SPT-N defines the depth of 6 m for the slip surface. Although the shear wave velocity and the ERT refer to different parameters, the comparison of their variation can be useful in verifying the results; therefore, the shear velocity profile at station ST5, the ERT profile at P3 and SPT-N in borehole BH6 were compared. The good compatibility of the results derived from the ambient noise measurements, ERT and boreholes data confirms the reliability of the results (Fig. 6-8).

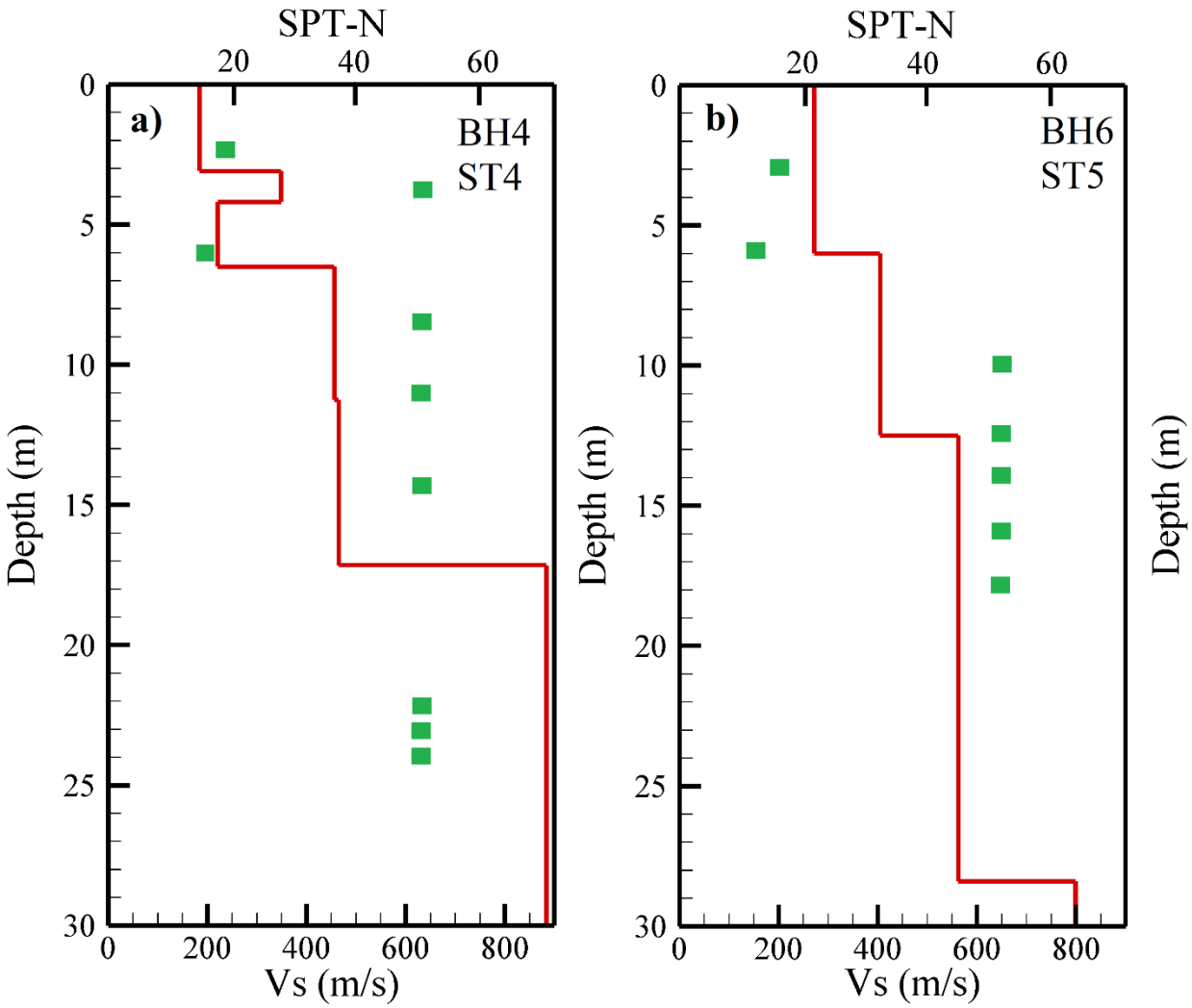

Fig. 6- 8 Comparison between shear wave velocity (red line) and SPT-N (green square) at stations a) ST4 b) ST5.

One of the difficulties in HVSR interpretation is defining the peaks of persistent features relevant to site response. To overcome this problem, Bard and SESAME Participants in (Bard and SESAME Participants 2004) suggested that peak amplitude should have a minimum value of 2 and the standard

deviation around the mean HVSR values achieved from all the analysed time windows should have prescribed limits. Nevertheless, these limitations are overly restrictive in landslide cases, where complex site conditions can generate a complicated spectral pattern of multiple peaks. Furthermore, the contribution of different type of waves to the noise (Rayleigh, Love, and body waves) increases the problems because the peak amplitude can considerably vary according to the portion of these waves present in the noise wave-field (Bonnefoy-Claudet et al. 2006). Thus, to overcome some of these limitations and to obtain more information from the noise analysis, we employed the HVIP (Horizental to Vertical Instantaneous Polarisation analysis) method, which can more efficiently identify, within the noise recording, Rayleigh wave packets, whose characteristics can be a useful tool in defining subsoil properties controlling the site dynamic response (fig. 6-9).

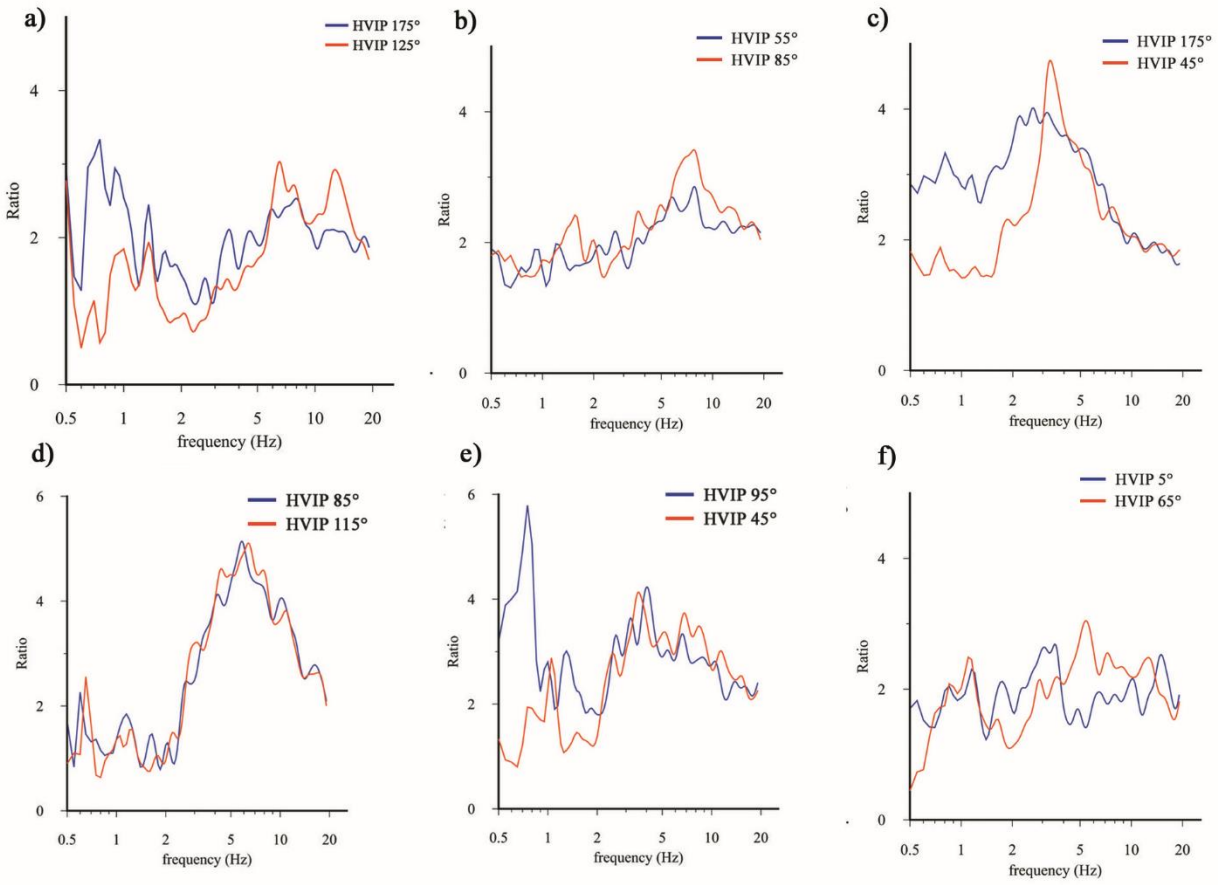

Fig. 6- 9 Rayleigh wave ellipticity achieved by using the HVIP method along the directions of main peak values (specified by the legend).

6-6 Site response directivity

The analysis of seismic site response is studying the factors like topographic and litho-stratigraphic, which are responsible for ground motion amplification, ground motion directivity, and slope dynamic response. Site response directivity is defined as a directional resonance phenomenon and is proven effective to depict resonance frequencies related to topographic amplification, anisotropy in slope materials, and mechanical properties (e.g. Chávez-García et al. 1996, Spudich et al. 1996). In studying the site response directivity in landslide areas, Del Gaudio et al. (2008) were the pioneer to present a comprehensive directional analysis of ambient noise data to study the differences in H/V ratios estimated along orthogonal directions. Despite the numerous case studies in landslide areas, the origin of directional resonance has remained uncertain due to the difficulty in recognition of the involved factors. This implies the presence of various mechanisms that cause the site directivity, which increases the necessity of different data sets.

The anisotropy of shear wave velocity caused by mobilization of softer materials in landslides can depict directional amplification. At the interface between substratum and surface layer, the transmission coefficient is increased for the waves polarized transversally to the direction of dominant fissuring due to the directional variation of wave velocity. However, the factors control the behavior of slope materials under dynamic conditions is not only dependent on mechanical effects of mass movements but also on structural properties and the geometry of geological bodies. The variation of directivity of ground motion amplification can highlight a deformation in substratum geology due to morphological and structural factors acting at various frequencies. It can be concluded that the directional amplification does not need to be coincident with the direction of slope along which the landslide occurs. It is significant to note that the similarity of direction in slope and maximum amplification can increase the effect of directivity on the mass movement.

The site response directivity can be analyzed using the three quantities of frequency, amplitude, and azimuth. Studying these quantities requires ad hoc information; hence, the ERT, geotechnical, and field surveys were integrated as an input to illuminate the substratum materials and geological structures. The results of the directional variation of those H/V ratios obtained in Fig. 6-6 are illustrated in Fig. 6-10 and those ellipticity curves estimated in Fig. 6-9 are depicted in Fig. 6-11.

ST1 shows no significant prevailing directivity in site response at the reference station, although a certain directivity seems present around 160° with two peaks at 7 and 12–13 Hz. Additionally, its amplification occurs only at high frequencies (around 7 Hz), and therefore, this station can be chosen as a

reference to detect directivity at lower frequencies. The directional maxima at the reference site are controlled by source effects rather than site effects since it shows variable directivity in measurement repetitions.

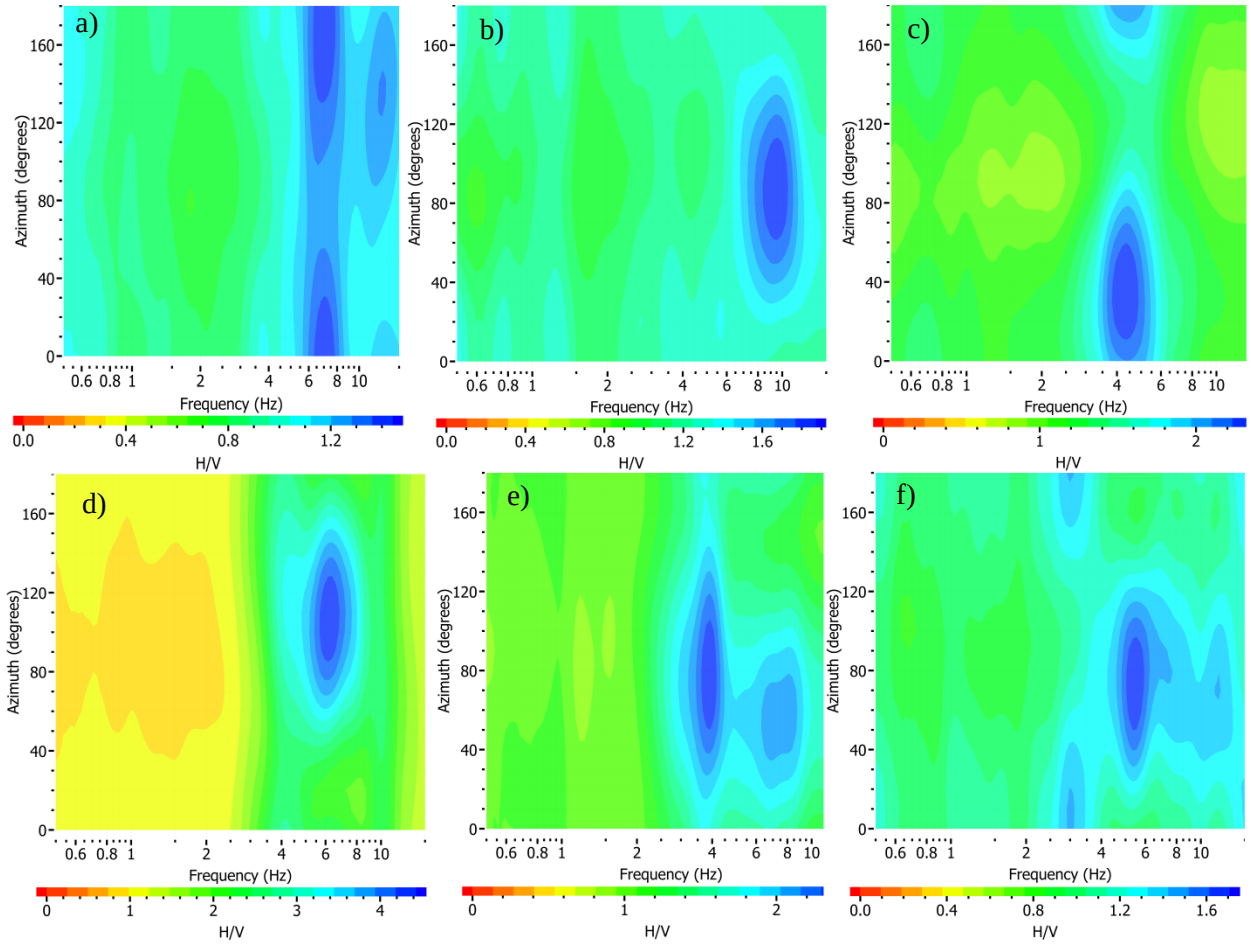

Fig. 6- 10 Azimuthal variations of HVSR values obtained for stations (a) ST1, (b) ST 2, (c) ST 3, (d) ST 4, (e) ST5 and (f) ST6.

Considering Fig. 6-10, differences can be seen in the maximum amplification frequencies among different sites, even in the case of ST5 and ST6 (4 and 5.5 Hz, respectively), which are relatively close to each other and almost located on the same lithology. The differences in peak frequency can be related to the changes in mechanical properties generated by the landslide on slope material or the reduction of landslide thickness, moving toward its toe, as an effect of substratum undulations, related to the pre-existing topography. These resonance frequencies are possibly due to the 28 m depth of sliding surface on the mobilized mass. Inverting the H/V curve at these sites, interpreted as representative of Rayleigh wave ellipticity, in terms of a sub-soil velocity model, resulted in an estimate between 450 and 800 $m.s^{-1}$ for the substratum shear wave velocity and 200-450 $m.s^{-1}$ for the landslide materials (Fig. 6-8). Considering the

known relationship ($F_0 = V_s /4H$) linking the surface layer shear velocity, V_s, and thickness, H, to the resonance frequency, F_0, these velocities imply that resonance frequencies from 4 to 5.5 Hz should correspond to landslide thicknesses varying from 9 to 12.5 m for the minimum velocity estimation and from 20 to 28 m for the maximum. These impedance contrasts between the surface and substratum materials can blur the cause of directivity; thus, a combination of various factors, such as structural factors and lithology, is normally assumed as the primary reason of directional amplification. The azimuthal variation of HVSR values demonstrated that all sites located on landslide mass (except ST3) are characterized by pronounced site response directivity approximately along 60–100° azimuths. With regard to "crest" stations, a resonance at frequencies of 3-4 Hz, with a maximum in NE can be recognized at ST3, which is more pronounced in HVIP analysis (H/V peak = 4.7) than Nakamura (H/V = 2.9). According to the HVIP results, the directional maximum in this station exceeds transverse minimum by a factor of 2.6 at 3.3 Hz, which appears corelated to local features of the site (transverse to local tension cracks). A higher frequency resonance (7-8 Hz) east-west directed can be recognized at ST2, although not so strong (H/V = 3.4). These resonance effects are less clear from the Nakamura's analysis and, according to the SESAME criterion of a minimum threshold 2, resonance would be excluded for most of them.

The stations ST4 and ST5 share the common presence of at least one peak (not necessarily the major) in a frequency band between 3 and 6 Hz in HVIP analysis (Fig. 6-9 d and e). This peak is more pronounced at ST4 (H/V 5.1 at 5.85 Hz) and ST5 (H/V 4.2 at 4.05 Hz), in both case with a weakly directional character (azimuthal variations of H/V do not exceed 70%) (Fig. 6-11 d and e). The secondary peaks around 8-10 Hz partially merged with the major 6 Hz peak for ST4 and H/V = 3.7 at 6.8 Hz for ST5. Comparing stations ST4, and ST5 located on the body of sliding mass reveals that the directivity is likely controlled by landslide material fissuring (transverse to sliding direction) which makes it more deformable and amplifies ground vibration, while the frequency is controlled by the thickness and Vs of landslide material. The difference in H/V peak amplitude is related to the difference in impedance contrast, which implies a variation of substratum properties. It is difficult to rely on fundamental resonance frequencies obtained from H/V spectral ratios since its vertical component can be amplified under special conditions, which results in the reduction of the H/V ratios. The substratum material at station ST4 represents low electrical resistivity which is an indication of water content. The increase in water content causes the rise of P-wave velocity and conclusively increases the H/V ratio. This phenomenon can be the reason for large amplification at station ST4 compare to the near stations.

At ST6, located slightly less than 200m away from ST5, site amplification is less evident. It is worth noting the similarity of ST4 and ST5 with ST6, located down the hill, in preferential directivity and their differences in frequency. Thus, it seems the landslide thickness variations and the lateral variations of landslide materials velocity are responsible for the frequency discrepancy, and the directional similarity is

due to the effect of the landslide and major fissure system orientation which is transversal to the maximum slope direction in the region, although the geology can be effective as well in both frequency and directivity. The Nakamura's analysis recognized the primary peak at 5.5 Hz at the station ST6 in direction 80°; while the HVIP defined the directional resonance in direction 65°. The other discrepancy between these two methods is in detection of the secondary peak defined at 3 Hz shows the maximum in direction 170° in Nakamura's method while in HVIP method the secondary peaks are at 7.25 and 12.55 in direction 65°.

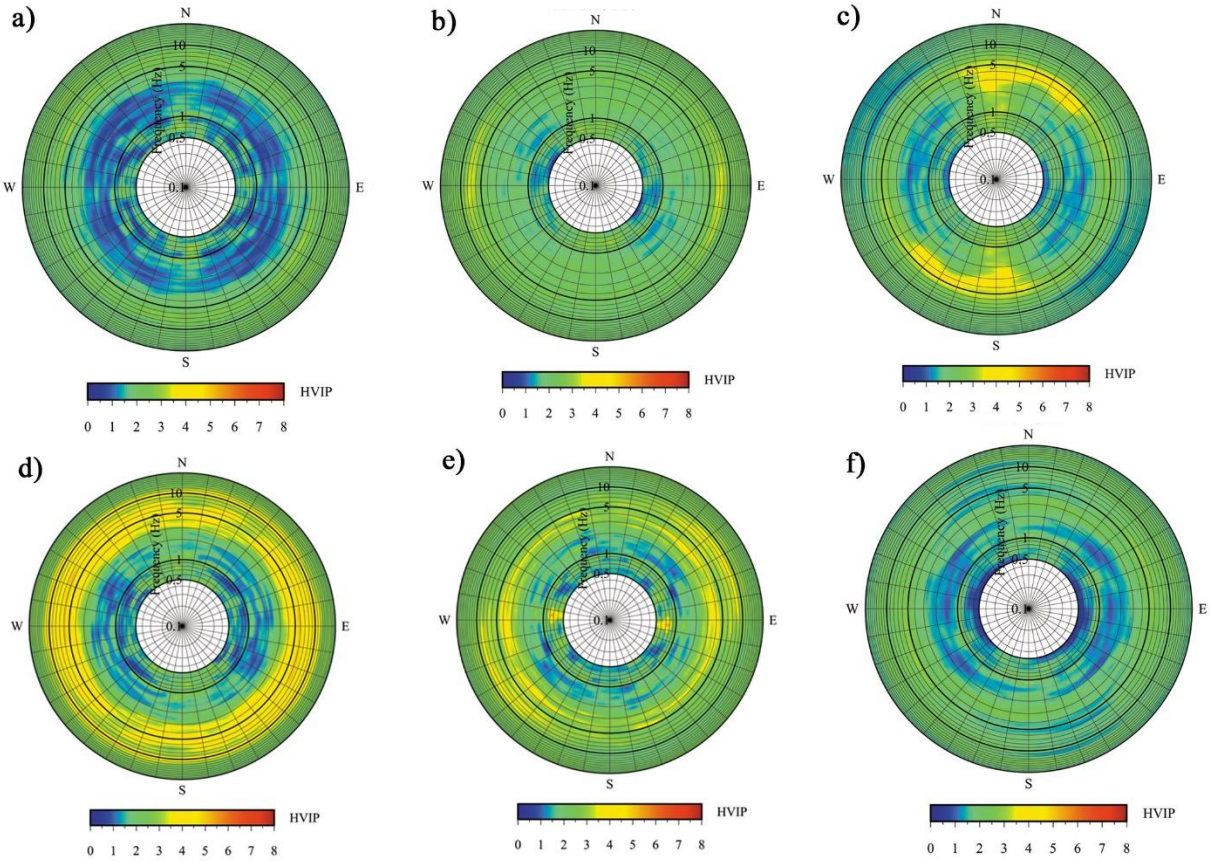

Fig. 6- 11 Polar diagrams of HVIP values obtained from noise recordings

The site response directivity can be verified via a comprehensive field survey and study Nargeschal landslide map to identify all slide paths, cliff sides, ruptures, old landslides and tension cracks. However, it is significant to identify the reliability of the obtained directivities. Therefore, the criteria proposed by Del Gaudio et al. (2014) were followed in this study to validate the directional resonance detected at each station. The results of the evaluation are presented in Table 3-4. These criteria are as follows:

1- The presence of relative maxima with an amplitude larger than 2 in the average H/V spectral ratios;
2- The azimuthal variation of spectral ratios of such maxima, with their amplitude at the resonance frequency presenting a lessen down to a direction orthogonal to maximum, which cannot exceed larger than 2/3 of the maximum;
3- Consistent orientation (within 20°-30°) of resonance directional peaks in the H/V spectral ratios;
4- The consistency in the presence of maxima which means the time windows show consistent directional peaks which satisfy the criteria 1 and 2 in different recording sessions.

The first criterion is an identification factor in evaluating the presence of amplification conditions. The second criterion shows the presence of a notable anisotropy of site response. The third criterion detects the direction along which the maxima are prone to be focused. The last criterion is to validate that the directional resonance is due to the consecutive and coherent polarized waves during the acquisition. According to the criteria proposed by Del Gaudio et al. (2014), the Nakamura's results are not reliable, while the results obtained by HVIP fulfilled all the criteria.

The effect of topography in the observed directivity of the study region is unfeasible based on the facts that the topography amplification requires sharp, convex shape of topography relief. In general, topographic amplification is expected as the effect of wave-field focusing at the top of relief, typically with a directional maximum transverse to relief elongation. However, such an effect can hardly produce amplifications by factors larger than 2 and tends to decrease moving from the top of the relief. Stronger effects can be caused by lithology or structural factors, and sometimes these effects are mixed to each other. Indeed, structural factors can also control the relief morphology, so that both topography and structural factor concur to amplify more ground motion in the same direction. The reason for the frequent presence of maximum amplification along sliding direction is that generally, mass movement causes the opening of fissure/fracture systems transverse to the sliding direction, which, in turn, make the material more deformable in such directions.

This claim is supported by the coexistence of distinct directivity detected by two stations located on the same slope but with different substratum materials (ST6 on the landslide and ST1 on the outcrop) and the same directivity for stations (ST5 and ST6) located on different topography but the same substratum material. Station ST1 shows almost no preferential directivity while station ST6 presents the directivity along the direction of the slope. The substratum material under station ST1 is made of siltstone and sandstone, while the materials beneath ST6 consist of clay and weathered shale and marl (Table 3-5). The geological characteristics of the topography relief can arbitrate the relationship between the site directivity and topography. As an example, the directivity recognized at ST2 was controlled by the slope while at ST3,

the fracture systems were responsible for the detected directivity. These examples strengthen the speculation that a directional distribution of energy mostly causes directivity.

The observed directivity at different frequency bands could be due to several factors such as the 3-D geometry of the landslide body affecting at different scales (Del Gaudio 2017). The presence of multiple peaks in the results can be the effect of different vibration modes or complex site conditions. The site responses of all stations indicated that the observed directivity at different frequency bands is due to the effect of the landslide, except for ST3, which is probably caused by the direction of fractures. The compatibility of directivity observed at the stations located on the landslide region with the maximum slope, which is also the direction of the landslide, has been mentioned in other researches (Del Gaudio et al. 2014; Pilz et al. 2014). However, some considerations are necessary for interpreting single station data since the results may be biased by the presence of sources exciting strongly polarized signals in a wide frequency range; For instance, dominant winds causing oscillations of trees or high buildings in the same direction with different oscillation periods. The azimuthal variations, the resonance frequency and amplitude of each station associated with the corresponding factor caused the directivity are summarized in Table 3-5.

Table 6- 3 Ambient noise stations with their corresponding amplification and directional resonance

Station	**Azimuth (o)**	**Resonance frequency**	**Amplitude**	**Slip material**	**Primary reason of directional**
ST1	Not defined	7	2	Siltstone and Sandstone	Source effect
ST2	90	9.5	2.4	Brown Clay, weathered Shale and Marl with Sandstone	landslide
ST3	40	4.5	2.8	Siltstone and Sandstone	Tension cracks with azimuth of 130
ST4	100	6.5	5	Shale and Siltstone	landslide
ST5	80	4	3.3	Shale and Siltstone	landslide
ST6	80	5.5	2.2	Shale and Siltstone	landslide

6-7 Conclusions

Assessment on seismically induced susceptibility to slope failure has been a crucial topic for geotechnical engineers, particularly in the case of urban area proximity to a landslide-prone zone. Slopes

with a deep-seated landslide can be an amplification factor of seismic ground motion, with a maximum along the sliding direction. In such situations, slopes with high impedance contrast of layers along the 3D geometry of a landslide body can induce trapping seismic waves and prolonging shaking, which conclusively makes slopes more prone to seismically induced reactivation of the landslide. This phenomenon is more likely in the case of polarizing shaking energy along the hill slope facing direction. The presence of more factors producing directional spectral peaks is a common property of site response directivity phenomena. A comprehensive evaluation of the effective factors on landslide was discussed in Rezaei et al. (2019) and Kazemnia Kakhki et al. (2020). In this chapter, we try to highlight factors control site response directivity via using a combination of reconnaissance techniques. The method introduced by Nakamura (1989) has only application on simple sites. This limitation was enhanced by the method proposed by Del Gaudio (2017). Therefore, a comparative use of these methods was applied in this part to evaluate their performance under complex conditions of the site.

Besides the ambient noise analysis, the ERT, geotechnical and field approaches were also applied to reveal the complex tectonic and geological structure of the area. Boreholes helped in determining the soil properties and conclusively defining the depth and geological features of slip surfaces. Field surveys were also conducted to define outcrops, flow pathways, types of soil in the region and the properties of the landslide. The results achieved in this work are as follows:

- The high value of the resonance frequency in the region indicates the seismic impedance contrast in shallow interfaces;
- The lower velocity of substratum materials of the slope compared to the ones outside the influenced region was due to the landslide effect;
- The absence of peaks at some frequencies at different stations was due to the amplification of the vertical component at these frequencies
- Source effects were the reason for no significant prevailing directivity in site response at the reference station;
- Variations in mechanical properties and different vibration modes caused the differences in the maximum amplification frequencies and the presence of multiple peaks;
- Shallow discontinuities caused the wave polarisation rotation at the station on the crown;
- Lithology and fracture/fissure systems have a significant role in controlling site response at our site and landslide can explain only some of the directional peaks.

According to the results, structural factors and landslide material mechanical properties deriving from the landslide deformation explained the twist of the spectral features with moderately varying peaks

at different frequencies due to the various factors acting along similar directions. The presence of different factors responsible for site response directivity resulted in directional resonance at different frequencies. To associate the relevant frequencies with the corresponding factors required applying approaches that rendered a better understanding of the substratum materials and geological features. Therefore, integrating the methods used in this work verify that the heterogeneities recognized using ambient noise analysis are induced by the landslide movements. The results of tests carried out at different stations confirm that the HVIP method has a functional capacity for delineating the frequency and orientation of directional resonance. It is also derived that the outputs of the Nakamura's method are unreliable in some cases, while the HVIP method renders more stable results owing to the purity of the ellipticity curves from interference of other wave types. It should be noted that the results obtained in this work has great compatibility with the results of ERT and geotechnical surveys in the study area. The HVIP method is also capable of revealing the site resonance properties which are indefinable with the Nakamura's method.

This study can enhance our knowledge of similar landslide-prone regions. Moreover, the variation of site directivity from the landslide-controlled orientation could be used to delimit the active part of the main landslide body and prevent more casualties and financial losses caused by this disastrous natural phenomenon. The study of directional resonance is more important for the slopes that their potential sliding direction is according to the maximum resonance orientation.

Chapter 7

Conclusions and Recommendations

7-1 Overview

This study has enhanced the perceiving of waves contribution in seismic signals through polarisation analysis. A cutting-edge solution was presented in this work for improving the resolution of the polarisation attributes spectra. This contribution provided a viable alternative to the ST in polarisation analysis and obtained comprehensive results proving the superior performance of the sparse ST. The ability of both time and frequency regularization and high resolution of the proposed spectral decomposition approach was used to delineate the arrival of different phases more distinctly and help us to estimate the polarisation attributes more effectively.

The proposed procedure was a clear advance on current polarisation methods by improving the resolution of the attributes and reducing the computational complexity. Impressive results obtained from this work take advantage of the high-resolution polarisation attributes to predict the packets of Rayleigh wave to design a robust adaptive filter for their removal.

The principal feature of this adaptive sparse approach is to restrain random noise pervasive in both time and frequency domains. However, the random noise problem has not been solved completely in the sparse ST. This motivated us to propose a better time-frequency decomposition to have higher resolution and is more robust against noise.

Thus, in this work, the problem has been solved within the framework of a sparsity-based optimisation and weighting function. Indeed, by using the Geman-McClure and Laplace functions, the weighting function has been incorporated into the existing SST approach, to introduce the WSST method. The fundamental role of the weighting function is to enhance the frequency components with the larger amplitudes proposed by the SST technique and to attenuate the components with low amplitudes but without eliminating the desired signal.

Finally, to introduce the application of polarisation methods, the site response characteristics of a landslide case, consisting of multiple resonance frequencies with directional variations of amplification, is analysed by taking advantage of the polarisation analysis. This procedure is by applying the analysis of

instantaneous polarisation on ambient noise data. To define Rayleigh waves ellipticity and polarisation direction as function of frequency, wave packets of Rayleigh waves first determined by polarisation properties. Analytic transformation was applied to the recording components to obtain the maximum amplitude of ground motion on the horizontal plane and the amplitude of the vertical component and eventually to calculate the ellipticity, their ratio is considered.

One of the main reasons for applying the instantaneous polarisation method on the data sets is that just a small portion of wave has Rayleigh polarisation, therefore average noise characteristics over time windows of the order of seconds are misleading our results. Directional variations of site response can be derived from analyzing the variation of the mean ellipticity values with azimuth and frequency. Especially, the directional resonance conditions can be observed if a preferential orientation of Rayleigh wave direction combined with eminent peaks of ellipticity curves at certain frequencies is available. The proposed polarisation analysis is a new method to analyse ambient noise data in site response by adding elements to study ambient noise origin which results in more constraints to its modeling.

The recognition of the occurrence of directional resonance phenomena can imply the need for redefining design actions to take into consideration these effects, for instance increasing the design spectra, in comparison to what is prescribed for the soil on flat surfaces. Site response directivity also has application in modelling earthquake ground motion for active seismic regions, earthquake scenarios, hazard assessment, and seismic regulation. The polarisation methods have also application in waveform tomography, characterization of surface waves, the splitting of shear waves, and seismic exploration.

7-2 Main conclusions

The significant findings of the work presented in this dissertation can be summarized as follows:

1- A high-resolution and robust time-frequency decomposition was introduced, which is superior to the previous methods in rendering higher resolution images even under the low SNR.
2- A polarisation filter was devised in the time-frequency domain via estimating the polarization attributes directly from the time-frequency spectra. The polarisation filter optimally extracted the Rayleigh waves from the data. This filtering helped detect the arrival of different types of waves more distinctly.
3- A landslide phenomenon was evaluated using the ambient noise recordings, which were filtered using the polarisation method to extract the Rayleigh waves. The ellipticity of the extracted Rayleigh wave packets was used to define the directional resonance frequency of the study site. Analysing the data using polarisation method resulted in more accurate and more detailed directional resonance frequency, which effects in our interpretation of the occurred landslide.

7-3 Recommendations for future research

The work presented in this dissertation opens new opportunities for further research. There are three aspects of this thesis that can be improved by further studies. The first one is the time-frequency decomposition proposed. Although its computational complexity is the same as ST, one can reduce the cost of computation of this transform. This is a remarkable challenge not only in this work but also in most of the geophysical methods due to the large volume of the data. The other challenge in the time-frequency decomposition is the windowing. To overcome the problem of a Gaussian-window-based-S-transform that degrade the time resolution in the time-frequency spectrum due to the long front taper, an asymmetric bi-Gaussian window is proposed by Pinnegar and Mansinha (2003) and Cheng et al. (2016). The window problem can also be solved by the Wigner-Ville distribution (WVD) which increases the resolution using no window in calculating the time-frequency representation (O'Neill et al. 1999; Wu and Liu 2010). Considering that the WVD has limitations due to its cross-term interference and its loss of phase information.

The second aspect that can be studied more is polarisation analysis. Several methods benefit the Hilbert transform to estimate the polarisation attributes. These methods are based on the analytic signal; therefore, a robust Hilbert transform will definitely improve their efficiency in defining their target. Taking advantage of the proposed Hilbert transform in chapter 2.4 can enhance these types of methods.

A comprehensive comparison needs to be done between the polarisation methods in retrieving a seismic wave under different circumstances. In this thesis, the time-frequency polarisation filtering is applied to extract the Rayleigh waves, but there are other time-frequency analyses available to fulfill the same task, which can be enhanced using the proposed methods in this dissertation.

One can also use an alternative for the transform used in the time-frequency polarisation filter introduced in this study and compare their performance. A wavelet transform is an option that has the potential of working with large data sets. A physical and numerical model can also be devised to test the efficiency of the proposed polarisation method.

The third part that has the potential to be investigated vastly is the application of the proposed methods in the real world. For example, in seismic exploration, one can apply the polarisation methods in filtering the seismic data when the ground rolls are an obstacle in rendering a clear image of the subsurface. Moreover, civil engineers can also use the method proposed in chapter 6 to obtain the site amplification factor, which is a critical parameter for their future design. In this thesis, we focused on the landslide example, but there are other natural and manmade disasters like sinkholes that can be studied using the analysis proposed in chapter 6.

References

Aki K, Richards PG (1980) Quantitative Seismology, Theory and Methods Volume I and Volume II. Book

Ali A, Younas M, Ullah M, et al (2019) Characterization of secondary reservoir potential via seismic inversion and attribute analysis: A case study. J Pet Sci Eng. https://doi.org/10.1016/j.petrol.2019.03.039

Anant KS, Dowla FU (1997) Wavelet transform methods for phase identification in three-component seismograms. Bull Seismol Soc Am

Andrade MCB, Porsani MJ, Ursin B (2018) Complex Autoregressive Time-Frequency Analysis: Estimation of Time-Varying Periodic Signal Components. IEEE Signal Process Mag. https://doi.org/10.1109/MSP.2017.2783942

Arai, H., Tokimatsu, K. (1998) Evaluation of local site effects based on microtremor H/V spectra. In: Second International Symposium on the Effects of Surface Geology on Seismic Motion. Yokohama, Japan. pp 673–680

Arai, H., Tokimatsu K (2000) Effects of Rayleigh and love waves on microtremor H/V spectra. In: the 12th World Conference on Earthquake Engineering. Auckland, New Zealand.

Ardhuin F, Stutzmann E, Schimmel M, Mangeney A (2011) Ocean wave sources of seismic noise. J Geophys Res Ocean. https://doi.org/10.1029/2011JC006952

Asten MW (2004) Comment on "Microtremor observations of deep sediment resonance in metropolitan Memphis, Tennessee" by Paul Bodin, Kevin Smith, Steve Horton and Howard Hwang. Eng Geol 72:343–349. https://doi.org/10.1016/j.enggeo.2003.09.001

Asten MW (1978) Geological control on the three-component spectra of Rayleigh-wave microseisms. Bull Seismol Soc Am

Asten MW, Henstridge JD (1984) Array estimators and the use of microseisms for reconnaissance of sedimentary basins. GEOPHYSICS. https://doi.org/10.1190/1.1441596

Aster RC, McNamara DE, Bromirski PD (2008) Multidecadal climate-induced variability in microseisms. Seismol Res Lett. https://doi.org/10.1785/gssrl.79.2.194

Bard P-Y, SESAME Participants (2004) The SESAME project: an overview and main results. In: 13th world conference on earthquake engineering

Bard P (1998) Microtremor measurement : a tool for site effect estimation? K Irikura K Kudo H Okada T Sasatami Eds

Bataille K, Chiu J (1991) Polarization analysis of high-frequency, three-component seismic data. Bull Seismol Soc Am

Beaty KS, Schmitt DR, Sacchi M (2002) Simulated annealing inversion of multimode Rayleigh wave dispersion curves for geological structure. Geophys J Int. https://doi.org/10.1046/j.1365-246X.2002.01809.x

Bignardi S, Mantovani A, Abu Zeid N (2016) OpenHVSR: Imaging the subsurface 2D/3D elastic properties through multiple HVSR modeling and inversion. Comput Geosci. https://doi.org/10.1016/j.cageo.2016.05.009

Boashash B (2015) Time-Frequency Signal Analysis and Processing: A Comprehensive Reference

Bodin P, Smith K, Horton S, Hwang H (2001) Microtremor observations of deep sediment resonance in metropolitan Memphis, Tennessee. Eng Geol. https://doi.org/10.1016/S0013-7952(01)00058-8

Bonnefoy-Claudet S (2004) Nature du bruit de fond sismique: Implications pour les études des effets de site. Ph.D. thesis,University Joseph Fourier, Grenoble, France. (In French with English abstract).

Bonnefoy-Claudet S, Cornou C, Bard P-Y, Cotton F (2004) Nature of noise wavefield

Bonnefoy-Claudet S, Cotton F, Bard PY (2006) The nature of noise wavefield and its applications for site effects studies. A literature review. Earth-Science Rev 79:205–227. https://doi.org/10.1016/j.earscirev.2006.07.004

Boore D, Toksöz M (1969) Rayleigh wave particle motion and crustal structure. Bull Seismol Soc Am

Bourdeau C, Havenith HB (2008) Site effects modelling applied to the slope affected by the Suusamyr earthquake (Kyrgyzstan, 1992). Eng Geol 97:126–145. https://doi.org/10.1016/j.enggeo.2007.12.009

Bracewell RN (2000) The Fourier Transform and applications. McGraw Hill

Burjánek J, Gassner-Stamm G, Poggi V, et al (2010) Ambient vibration analysis of an unstable mountain slope. Geophys J Int 180:820–828. https://doi.org/10.1111/j.1365-246X.2009.04451.x

Chávez-García FJ, Sánchez LR, Hatzfeld D (1996) Topographic site effects and HVSR. A comparison between observations and theory. Bull. Seismol. Soc. Am. 86:1559–1573

Chen CY (2009) Sedimentary impacts from landslides in the Tachia River Basin, Taiwan. Geomorphology 105:355–365. https://doi.org/10.1016/j.geomorph.2008.10.009

Cheng Z, Chen W, Chen Y, et al (2016) Application of bi-Gaussian S-transform in high-resolution seismic time-frequency analysis. Interpretation. https://doi.org/10.1190/INT-2016-0041.1

Chouet B, De Luca G, Milana G, et al (1998) Shallow velocity structure of Stromboli Volcano, Italy, derived from small-aperture array measurements of Strombolian tremor. Bull Seismol Soc Am

Christoffersson A, Husebye ES, Ingate SF (1988) Wavefield decomposition using ML-probabilities in modelling single-site 3-component records. Geophys J. https://doi.org/10.1111/j.1365-246X.1988.tb01996.x

Claassen JP (2006) Robust Bearing Estimation for Three-component Stations. Pure Appl Geophys. https://doi.org/10.1007/pl00001163

Cornou C (2002) Traitement d'antenne et imagerie sismique dans l'agglomération grenobloise (Alpes françaises): implications pour les effets de site. Ph.D. Thesis, University Joseph Fourier, Grenoble, France. (In French with English abstract).

Del Gaudio V (2017) Instantaneous polarization analysis of ambient noise recordings in site response investigations. Geophys J Int. https://doi.org/10.1093/gji/ggx175

Del Gaudio V, Coccia S, Wasowski J, et al (2008) Detection of directivity in seismic site response from microtremor spectral analysis. Nat Hazards Earth Syst Sci. https://doi.org/10.5194/nhess-8-751-2008

Del Gaudio V, Luo Y, Wang Y, Wasowski J (2018) Using ambient noise to characterise seismic slope response: The case of Qiaozhuang peri-urban hillslopes (Sichuan, China). Eng Geol. https://doi.org/10.1016/j.enggeo.2018.10.008

Del Gaudio V, Muscillo S, Wasowski J (2014) What we can learn about slope response to earthquakes from ambient noise analysis: An overview. Eng Geol 182:182–200. https://doi.org/10.1016/j.enggeo.2014.05.010

Del Gaudio V, Wasowski J (2011) Advances and problems in understanding the seismic response of potentially unstable slopes. Eng Geol 122:73–83. https://doi.org/10.1016/j.enggeo.2010.09.007

Del Gaudio V, Zhao B, Luo Y, et al (2019) Seismic response of steep slopes inferred from ambient noise and accelerometer recordings: the case of Dadu River valley, China. Eng Geol. https://doi.org/10.1016/j.enggeo.2019.105197

Devi A, Israil M, Anbalagan R, Gupta PK (2017) Subsurface soil characterization using geoelectrical and geotechnical investigations at a bridge site in Uttarakhand Himalayan region. J Appl Geophys. https://doi.org/10.1016/j.jappgeo.2017.07.005

Dey A, Ward SH (1970) INDUCTIVE SOUNDING OF A LAYERED EARTH WITH A HORIZONTAL MAGNETIC DIPOLE. GEOPHYSICS. https://doi.org/10.1190/1.1440122

Diallo MS, Kulesh M, Holschneider M, Scherbaum R (2005) Instantaneous polarization attributes in the time-frequency domain and wavefield separation. Geophys Prospect. https://doi.org/10.1111/j.1365-2478.2005.00500.x

Donoho DL (2006) Compressed sensing. IEEE Trans Inf Theory. https://doi.org/10.1109/TIT.2006.871582

Douze E (1967) Short-period seismic noise. Bull Seismol Soc Am

Du Z, Foulger GR, Mao W (2000) Noise reduction for broad-band, three-component seismograms using data-adaptive polarization filters. Geophys J Int. https://doi.org/10.1046/j.1365-246X.2000.00156.x

Farnbach JS (1975) The complex envelope in seismic signal analysis. Bull Seismol Soc Am

Frantti GE (1963) The nature of high-frequency earth noise spectra. Geophysics.

https://doi.org/10.1190/1.1439228

Gabor D (1946) Theory of communication. Part 1: The analysis of information. J Inst Electr Eng - Part III Radio Commun Eng. https://doi.org/10.1049/ji-3-2.1946.0074

Gholami A (2013) Sparse time-frequency decomposition and some applications. IEEE Trans Geosci Remote Sens. https://doi.org/10.1109/TGRS.2012.2220144

Goebel V (1984) Polarization and ground roll suppression. In: 1984 SEG Annual Meeting, SEG 1984

Goldstein T, Osher S (2009) The Split Bregman Method for L1-Regularized Problems. SIAM J Imaging Sci. https://doi.org/10.1137/080725891

Gutenberg B (1958) Microseisms. Adv Geophys. https://doi.org/10.1016/S0065-2687(08)60075-8

Guzzetti F, Ardizzone F, Cardinali M, et al (2008) Distribution of landslides in the Upper Tiber River basin, central Italy. Geomorphology 96:105–122. https://doi.org/10.1016/j.geomorph.2007.07.015

Harkrider BDG (1964) Surface waves in multilayered elastic media I. Rayleigh and love waves from buried sources in a multilayered elastic half-space. Bull Seismol Soc Am

Haskell NA (1953) "The dispersion of surface waves on multilayered media." Bull Seismol Soc Am 43:17–34

Hasselmann K (1963) A statistical analysis of the generation of microseisms. Rev. Geophys.

Haubrich, R.A. and McCamy K (1969) Microseisms: Coastal and pelagic sources. Rev Geophys 7:539–571

Herak M (2008) ModelHVSR-A Matlab® tool to model horizontal-to-vertical spectral ratio of ambient noise. Comput Geosci. https://doi.org/10.1016/j.cageo.2007.07.009

Herrmann RB (2013) Computer programs in seismology: An evolving tool for instruction and research. Seismol Res Lett. https://doi.org/10.1785/0220110096

Horike M (1985) Inversion of phase velocity of long-period microtremors to the S-wave-velocity structure down to the basement in urbanized areas. J Phys Earth. https://doi.org/10.4294/jpe1952.33.59

Jones DL, Parks TW (1990) A High Resolution Data-Adaptive Time-Frequency Representation. IEEE Trans Acoust. https://doi.org/10.1109/29.61539

JURKEVICS A (1988) Polarization analysis of three-component array data. BSSA

Kanai K (1955) On Sezawa-waves (M2-waves).: Part II. Bull Earthq Res Institute, Univ Tokyo 33:275–281

Kanai K and TT (1961) On mierotremors VIII. Bull Earthq Res Inst Tokyo Univ 39:97–114

Kazemnia Kakhki M, Peters FC, Mansur WJ, et al (2020) Deciphering site response directivity in landslide-prone slopes from ambient noise spectral analysis. Eng Geol. https://doi.org/10.1016/j.enggeo.2020.105542

Kedar S, Longuet-Higgins M, Webb F, et al (2008) The origin of deep ocean microseisms in the North Atlantic Ocean. Proc R Soc A Math Phys Eng Sci. https://doi.org/10.1098/rspa.2007.0277

Kleinbrod U, Burjánek J, Fäh D (2019) Ambient vibration classification of unstable rock slopes: A systematic approach. Eng Geol. https://doi.org/10.1016/j.enggeo.2018.12.012

Konno K, Ohmachi T (1998) Ground-motion characteristics estimated from spectral ratio between horizontal and vertical components of microtremor. Bull Seismol Soc Am

Kuwayama S (1992) Use of short-period microtremors for Vs profiling. J Geotech Eng. https://doi.org/10.1061/(ASCE)0733-9410(1992)118:10(1544)

Labonne C, Sèbe O, Gaffet S (2016) Seismic wavefield polarization – Part I: Describing an elliptical polarized motion, a review of motivations and methods. E3S Web Conf. https://doi.org/10.1051/e3sconf/20161206001

Lachet C, Bard PY (1994) Numerical and Theoretical Investigations on the Possibilities and Limitations of Nakamura's Technique. J Phys Earth. https://doi.org/10.4294/jpe1952.42.377

Lamoureux MP, Gibson PC, Grossman JP, Margrave GF (2003) A fast , discrete Gabor transform via a partition of unity. J Fourier Anal Appl

Li J, Liu C, Zeng Z, Chen L (2015) GPR signal denoising and target extraction with the CEEMD method. IEEE Geosci Remote Sens Lett. https://doi.org/10.1109/LGRS.2015.2415736

Li TMC, Ferguson JF, Herrin E, Durham HB (1984) HIGH-FREQUENCY SEISMIC NOISE AT LAJITAS, TEXAS

Lilly JM, Park J (1995) Multiwavelet spectral and polarization analyses of seismic records. Geophys J Int. https://doi.org/10.1111/j.1365-246X.1995.tb06852.x

Lima MVS, Ferreira TN, Martins WA, Diniz PSR (2014) Sparsity-aware data-selective adaptive filters. IEEE Trans Signal Process. https://doi.org/10.1109/TSP.2014.2334560

Liu J, Marfurt KJ (2007) Instantaneous spectral attributes to detect channels. Geophysics. https://doi.org/10.1190/1.2428268

Loris I, Nolet G, Daubechies I, Dahlen FA (2007) Tomographic inversion using ℓ1-norm regularization of wavelet coefficients. Geophys J Int. https://doi.org/10.1111/j.1365-246X.2007.03409.x

Lu W kai, Zhang CK (2013) Robust estimation of instantaneous phase using a time-frequency adaptive filter. Geophysics. https://doi.org/10.1190/GEO2011-0435.1

Luo Y, Al-Dossary S, Marhoon M, Alfaraj M (2003) Generalized Hilbert transform and its applications in geophysics. Lead Edge (Tulsa, OK). https://doi.org/10.1190/1.1564522

Malischewsky, P.G. and Scherbaum F (2004) Love's formula and H/V-ratio (ellipticity) of Rayleigh waves. Wave motion 40:57–67

Malvern LE (1969) Introduction to the Mechanics of a Continuous Medium. (No Monogr

Montalbetti JF, Kanasewich ER (1970) Enhancement of Teleseismic Body Phases with a Polarization Filter. Geophys J R Astron Soc. https://doi.org/10.1111/j.1365-246X.1970.tb01771.x

MOONEY HM, BOLT BA (1966) Dispersive characteristics of the first three Rayleigh modes for a single surface layer. Bull Seismol Soc Am. https://doi.org/

Mori T, Tobita Y, Okimura T (2013) Damages of Hillside Embankments in Sendai City During the 2011 Great East Japan Earthquake. In: Earthquake-Induced Landslides

Morozov IB (1996) Instantaneous polarization attributes and directional filtering. Geophysics. https://doi.org/10.1190/1.1444012

Nakamura Y (1989) A method for dynamic characteristics estimation of subsurface using microtremor on the ground surface. Q. Rep. Railw. Tech. Reasearch Inst. 30:25–33

Nakamura Y (2000) Clear identification of fundamental idea of Nakamura's technique and its applications. In: Proceedings of the 12th world conference on …

Natarajan BK (1995) Sparse approximate solutions to linear systems. SIAM J Comput. https://doi.org/10.1137/S0097539792240406

NOGOSHI M, IGARASHI T (1971) On the Amplitude Characteristics of Microtremor (Part 2). Zisin (Journal Seismol Soc Japan 2nd ser). https://doi.org/10.4294/zisin1948.24.1_26

Nuttli O (1961) The effect of the earth's surface on the S wave particle motion. Bull Seismol Soc Am

O'Neill JC, Flandrin P, Williams WJ (1999) On the existence of discrete Wigner distributions. IEEE Signal Process Lett. https://doi.org/10.1109/97.803429

Oh S, Sun CG (2008) Combined analysis of electrical resistivity and geotechnical SPT blow counts for the safety assessment of fill dam. Environ Geol. https://doi.org/10.1007/s00254-007-0790-y

Ohmachi, T., Umezono T (1998) Rate of Rayleigh waves in microtremors. In: the Second International Symposium on the Effects of Surface Geology on Seismic Motion. Yokohama, Japan, pp. pp 587–592

Ohmachi, T. et al. (1998) Rate of Rayleigh waves in microtremors. Second Int Symp Eff Surf Geol Seism Motion 2:587–592

Okada H (2003) The Microtremor Survey Method (translated by Koya Suto)

Oliver, J. and Ewing M (1957) Higher modes of continental Rayleigh waves. Bull Seismol Soc Am 47:187–204

Oppenheim, A.V. and Schafer RW (1975) Digital Signal Processing

Panza GF, Romanelli F, Vaccari F (2001) Seismic wave propagation in laterally heterogeneous anelastic media: Theory and applications to seismic zonation. Adv Geophys. https://doi.org/10.1006/ageo.2001.0001

Parrent GB, Roman P (1960) On the matrix formulation of the theory of partial polarization in terms of

observables. Nuovo Cim. https://doi.org/10.1007/BF02902573

Pilz M, Parolai S, Bindi D, et al (2014) Combining Seismic Noise Techniques for Landslide Characterization. Pure Appl Geophys. https://doi.org/10.1007/s00024-013-0733-3

Pinnegar CR (2006) Polarization analysis and polarization filtering of three-component signals with the time-frequency. Geophys J Int. https://doi.org/10.1111/j.1365-246X.2006.02937.x

Pinnegar CR, Mansinha L (2003) The S-transform with windows of arbitrary and varying shape. Geophysics. https://doi.org/10.1190/1.1543223

Rabiner LR, Gold B (1975) Theory and Application of Digital Signal Processing. IEEE Trans Acoust. https://doi.org/10.1109/TASSP.1975.1162708

Radad M, Gholami A, Siahkoohi HR (2015a) S-transform with maximum energy concentration and its application to detect gas bearing zones and lowfrequency shadows. J Earth Sp Phys

Radad M, Gholami A, Siahkoohi HR (2015b) S-transform with maximum energy concentration: Application to non-stationary seismic deconvolution. J Appl Geophys. https://doi.org/10.1016/j.jappgeo.2015.04.010

Rene RM, Fitter JL, Forsyth PM, et al (1986) MULTICOMPONENT SEISMIC STUDIES USING COMPLEX TRACE ANALYSIS. Geophysics. https://doi.org/10.1190/1.1442177

Rezaei S, Shooshpasha I, Rezaei H (2019) Reconstruction of landslide model from ERT, geotechnical, and field data, Nargeschal landslide, Iran. Bull Eng Geol Environ. https://doi.org/10.1007/s10064-018-1352-0

Rhie J, Romanowicz B (2006) A study of the relation between ocean storms and the Earth's hum. Geochemistry, Geophys Geosystems. https://doi.org/10.1029/2006GC001274

Roberts RG, Christoffersson A, Cassidy F (1989) Real-Time Event Detection, Phase Identification and Source Location Estimation Using Single Station Three-Component Seismic Data. Geophys J Int. https://doi.org/10.1111/j.1365-246X.1989.tb00517.x

Roult G, Crawford W (2000) Analysis of "background" free oscillations and how to improve resolution by subtracting the atmospheric pressure signal. Phys Earth Planet Inter. https://doi.org/10.1016/S0031-9201(00)00172-2

Samson JC (1977) Matrix and Stokes vector representations of detectors for polarized waveforms: theory, with some applications to teleseismic waves. Geophys J R Astron Soc. https://doi.org/10.1111/j.1365-246X.1977.tb04208.x

Samson JC (1983) Pure states, polarized waves, and principal components in the spectra of multiple, geophysical time-series. Geophys J R Astron Soc. https://doi.org/10.1111/j.1365-246X.1983.tb02825.x

Samson JC, Olson J V. (1980) Some comments on the descriptions of the polarization states of waves.

Geophys J R Astron Soc. https://doi.org/10.1111/j.1365-246X.1980.tb04308.x

Sattari H (2017) High-resolution seismic complex trace analysis by adaptive fast sparse S-transform. Geophysics. https://doi.org/10.1190/GEO2015-0425.1

Sattari H (2016) High-resolution seismic complex trace analysis by adaptive fast sparse S-transform. GEOPHYSICS. https://doi.org/10.1190/geo2015-0425.1

Sattari H, Gholami A, Siahkoohi HR (2013) Seismic data analysis by adaptive sparse time-frequency decomposition. GEOPHYSICS. https://doi.org/10.1190/geo2012-0550.1

Schimmel M, Gallart J (2005) The inverse S-transform in filters with time-frequency localization. IEEE Trans Signal Process. https://doi.org/10.1109/TSP.2007.896050

Schimmel M, Gallart J (2003) The use of instantaneous polarization attributes for seismic signal detection and image enhancement. Geophys J Int. https://doi.org/10.1046/j.1365-246X.2003.02077.x

Schimmel M, Gallart J (2004) Degree of polarization filter for frequency-dependent signal enhancement through noise suppression. Bull Seismol Soc Am. https://doi.org/10.1785/0120030178

Schimmel M, Stutzmann E, Ardhuin F, Gallart J (2011) Polarized Earth's ambient microseismic noise. Geochemistry, Geophys Geosystems. https://doi.org/10.1029/2011GC003661

Schuster R, Highland L (2003) Impact of landslides and innovative landslide-mitigation measures on the natural environment. Geol Hazards Team, US Geol …

Seo K (1998) A joint microtremors measurements in the Fukui basin to discuss the effects of surface geology on seismic motion during the 1948 Fukui, Japan Earthquake. Proc XIth Eur Conf Earthq Eng Paris, Sept 6 11:

Sepúlveda SA, Murphy W, Jibson RW, Petley DN (2005) Seismically induced rock slope failures resulting from topographic amplification of strong ground motions: The case of Pacoima Canyon, California. Eng Geol 80:336–348. https://doi.org/10.1016/j.enggeo.2005.07.004

Shalev-Shwartz S, Tewari A (2009) Stochastic methods for l 1 regularized loss minimization

Sheriff RE (2002) Encyclopedic Dictionary of Applied Geophysics

Shimshoni M, Smith SW (1964) SEISMIC SIGNAL ENHANCEMENT WITH THREE-COMPONENT DETECTORS. GEOPHYSICS. https://doi.org/10.1190/1.1439402

Singh KK, Mehrotra A, Pal K (2014) Landslide detection from satellite images using spectral indices and Digital Elevation Model. Disaster Adv 7:

Smart E, Sproules H (1981) Regional phase processors.

Smith BD, Ward SH (1974) ON THE COMPUTATION OF POLARIZATION ELLIPSE PARAMETERS. GEOPHYSICS. https://doi.org/10.1190/1.1440474

Steen W. (2000) Principles of Optics M. Born and E. Wolf, 7th (expanded) edition, Cambridge University Press, Cambridge

Stephenson WR (2003) Factors bounding prograde Rayleigh-wave particle motion in a soft- soil layer. Proc 2003 Pacific Conf Earthq Eng

Stockwell RG, Mansinha L, Lowe RP (1996) Localization of the complex spectrum: The S transform. IEEE Trans Signal Process. https://doi.org/10.1109/78.492555

Stratton JA (1941) Electromagnetic theory: McGraw-HIll Book Co.

Stutzmann E, Schimmel M, Patau G, Maggi A (2009) Global climate imprint on seismic noise. Geochemistry, Geophys Geosystems. https://doi.org/10.1029/2009GC002619

Suda N, Nawa K, Fukao Y (1998) Earth's background free oscillations. Science (80-). https://doi.org/10.1126/science.279.5359.2089

Sutton GH, Pomeroy PW (1963) Analog analyses of seismograms recorded on magnetic tape. J Geophys Res. https://doi.org/10.1029/jz068i009p02791

Taner MT, Koehler F, Sheriff RE (1979) COMPLEX SEISMIC TRACE ANALYSIS. Geophysics. https://doi.org/10.1190/1.1440994

Tanimoto T (2007) Excitation of microseisms. Geophys Res Lett. https://doi.org/10.1029/2006GL029046

Tanimoto T, Ishimaru S, Alvizuri C (2006) Seasonality in particle motion of microseisms. Geophys J Int. https://doi.org/10.1111/j.1365-246X.2006.02931.x

Telford WM, Geldart LP, Sheriff RE (1990) Telford - Applied Geophysics

Tibshirani R (2018) Regression Shrinkage and Selection Via the Lasso. J R Stat Soc Ser B. https://doi.org/10.1111/j.2517-6161.1996.tb02080.x

Tokimatsu K (1997) Geotechnical site characterization using surface waves. In: the First International Conference on Earthquake Geotechnical Engineering. pp 1333–1368

TOKIMATSU K, MIYADERA Y (1992) CHARACTERISTICS OF RAYLEIGH WAVES IN MICROTREMORS AND THEIR RELATION TO UNDERGROUND STRUCTURES. J Struct Constr Eng (Transactions AIJ). https://doi.org/10.3130/aijsx.439.0_81

Topsakal E, Topal T (2015) Slope stability assessment of a re-activated landslide on the Artvin-Savsat junction of a provincial road in Meydancik, Turkey. Arab J Geosci. https://doi.org/10.1007/s12517-013-1210-0

Tsai NC (1970) A NOTE ON THE STEADY-STATE RESPONSE OF AN ELASTIC HALF-SPACE. Bull Seismol Soc Am

van Westen CJ, van Asch TWJ, Soeters R (2006) Landslide hazard and risk zonation - Why is it still so difficult? Bull Eng Geol Environ 65:167–184. https://doi.org/10.1007/s10064-005-0023-0

Vella A, Galea P, D'Amico S (2013) Site frequency response characterisation of the Maltese islands based on ambient noise H/V ratios. Eng Geol. https://doi.org/10.1016/j.enggeo.2013.06.006

Vidale JE (1986) Complex polarization analysis of particle motion. Bull Seismol Soc Am

Ville J (1948) Theorie et applications de la notion de signal analytique. Cables Transm

Wang X, Chen W, Zhu Z (2019) Robust Seismic Volumetric Dip Estimation Combining Structure Tensor and Multiwindow Technology. IEEE Trans Geosci Remote Sens. https://doi.org/10.1109/TGRS.2018.2854777

Wathelet M (2005) Array recordings of ambient vibrations: surface-wave inversion, PhD thesis, Li`ege University, Belgium.

Wathelet M, Jongmans D, Ohrnberger M (2004) Surface-wave inversion using a direct search algorithm and its application to ambient vibration measurements. Near Surf Geophys. https://doi.org/10.3997/1873-0604.2004018

WHALEN AD (1971) Detection of Signals in Colored Gaussian Noise. In: Detection of Signals in Noise

Wolf E (1959) Coherence properties of partially polarized electromagnetic radiation. Nuovo Cim. https://doi.org/10.1007/BF02725127

Wu X, Liu T (2010) Seismic spectral decomposition and analysis based on Wigner-Ville distribution for sandstone reservoir characterization in West Sichuan depression. J Geophys Eng. https://doi.org/10.1088/1742-2132/7/2/002

Xue W, Dai X, Zhu J, et al (2019) A Noise Suppression Method of Ground Penetrating Radar Based on EEMD and Permutation Entropy. IEEE Geosci Remote Sens Lett. https://doi.org/10.1109/lgrs.2019.2902123

Yamamoto H (2000) Estimation of shallow S-wave velocity structures from phase velocities of Love- and Rayleigh-waves in microtremors. In: the 12th World conference on earthquake engineering. New Zealand: Auckland.

Yamanaka H, Takemura M, Ishida H, Niwa M (1994) Characteristics of long-period microtremors and their applicability in exploration of deep sedimentary layers. Bull - Seismol Soc Am. https://doi.org/10.1016/0148-9062(95)99176-x

Yazdanpanah H, Diniz PSR (2017) Recursive Least-Squares algorithms for sparse system modeling. In: ICASSP, IEEE International Conference on Acoustics, Speech and Signal Processing - Proceedings

Yuan S, Su Y, Wang T, et al (2019) Geosteering phase attributes: A new detector for the discontinuities of seismic images. IEEE Geosci Remote Sens Lett. https://doi.org/10.1109/LGRS.2018.2866419

Zhang J, Li Y, Wu N (2015) Noise attenuation for seismic data by hyperbolic-trace time-frequency peak filtering. IEEE Geosci Remote Sens Lett. https://doi.org/10.1109/LGRS.2014.2352671

Zhang SX, Chan LS (2003) Possible effects of misidentified mode number on Rayleigh wave inversion. J Appl Geophys. https://doi.org/10.1016/S0926-9851(03)00014-4